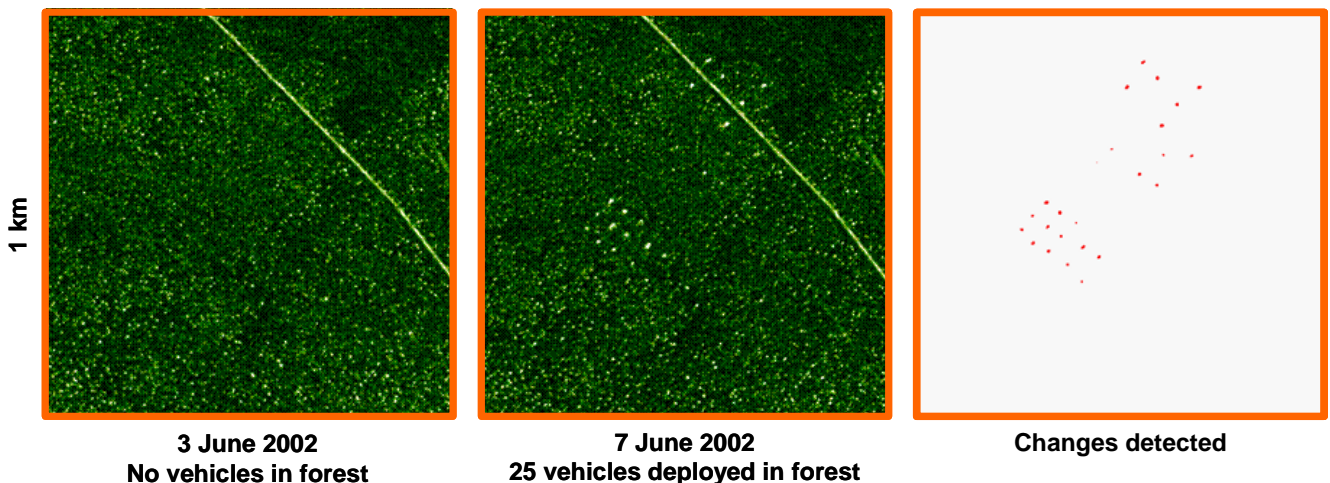


Lars M. H. Ulander, Björn Flood, Peter Follo, Per-Olov Fröling,
Anders Gustavsson, Tommy Jonsson, Björn Larsson, Mikael Lundberg,
William Pierson, and Gunnar Stenström

Flight Campaign Vidse 2002

CARABAS-II Change Detection Analysis



SWEDISH DEFENCE RESEARCH AGENCY

Sensor Technology

P.O. Box 1165

SE-581 11 Linköping

FOI-R--1001--SE

November 2003

ISSN 1650-1942

Scientific report

Lars M. H. Ulander, Björn Flood, Peter Follo, Per-Olov Fröling,
Anders Gustavsson, Tommy Jonsson, Björn Larsson, Mikael Lundberg,
William Pierson, and Gunnar Stenström

Flight Campaign Vidsel 2002

CARABAS-II Change Detection Analysis

Issuing organization FOI – Swedish Defence Research Agency Sensor Technology P.O. Box 1165 SE-581 11 Linköping	Report number, ISRN FOI-R--1001--SE	Report type Scientific report
	Research area code 4. C4ISR	
	Month year November 2003	Project no. E3029, E3789
	Customers code 5. Commissioned Research	
	Sub area code 42 Surveillance Sensors	
Author/s (editor/s) Lars M. H. Ulander Björn Larsson Björn Flood Mikael Lundberg Peter Follo William Pierson Per-Olov Frörlind Gunnar Stenström Anders Gustavsson Tommy Jonsson	Project manager Lars Ulander	
	Approved by Svante Ödman	
	Sponsoring agency Swedish Armed Forces, DARPA	
	Scientifically and technically responsible Lars Ulander	
Report title Flight Campaign Vidsel 2002. CARABAS-II Change Detection Analysis		
Abstract (not more than 200 words) <p>The airborne radar CARABAS-II conducted a data collection campaign at the RFN Vidsel test range between 30 May and 12 June 2002. Sixteen successful flight missions were flown resulting in 150 imaging passes.</p> <p>In this report, 64 synthetic-aperture radar (SAR) images from eleven flight missions are analyzed in order to evaluate CARABAS-II change detection performance.</p> <p>The operating conditions studied were changes in radar bandwidth, incidence angle, flight heading, radio-frequency interference, target orientation, and target size. The change detection processing scheme was intentionally kept uncomplicated and consistent, i.e. to ensure a robust performance across all of the operating conditions being investigated.</p> <p>The main general results showed that change detection performance improved when the processed bandwidth increased. Furthermore, performance improved when target size increased, but dropped when the incidence angle increased.</p>		
Keywords CARABAS, SAR, VHF, foliage penetration, ground surveillance, change detection		
Further bibliographic information	Language English	
ISSN 1650-1942	Pages 72 p.	
	Price acc. to pricelist	

Utgivare Totalförsvarets Forskningsinstitut - FOI Sensorteknik Box 1165 581 11 Linköping	Rapportnummer, ISRN FOI-R--1001--SE	Klassificering Vetenskaplig rapport
	Forskningsområde 4. Spaning och ledning	
	Månad, år November 2003	Projektnummer E3029, E3789
	Verksamhetsgren 5. Uppdragsfinansierad verksamhet	
	Delområde 42 Spaningssensorer	
Författare/redaktör Lars M. H. Ulander Björn Larsson Björn Flood Mikael Lundberg Peter Follo William Pierson Per-Olov Frörlind Gunnar Stenström Anders Gustavsson Tommy Jonsson	Projektledare Lars Ulander	
	Godkänd av Svante Ödman	
	Uppdragsgivare/kundbeteckning FM, DARPA	
	Tekniskt och/eller vetenskapligt ansvarig Lars Ulander	
Rapportens titel (i översättning) Flygkampanj Vidsele 2002. CARABAS-II Förändringsdetektionsutvärdering		
Sammanfattning (högst 200 ord) <p>Den flygburna radarn CARABAS-II utförde en datainsamlingskampanj vid RFN Vidsele under perioden 30 maj till 12 juni 2002. Sexton lyckade flygpass genomfördes vilket resulterade i 150 flyglöpar med radardata.</p> <p>I föreliggande rapport redovisas en analys av förändringsdetektion baserat på 64 SAR-bilder från elva flygpass.</p> <p>Systemparametrar som studerades var radarbandbredd, infallsvinkel, kurs, radiostörningsnivå, målorientering och målstorlek. Algoritmen som användes för förändringsdetektion definierades för att erhålla robusta prestanda för alla undersökta systemparametrar.</p> <p>Resultaten visar att prestanda för förändringsdetektion med CARABAS-II förbättras med ökande radarbandbredd. Vidare förbättras prestanda när målstorleken ökar, men försämras när infallsvinkeln ökar.</p>		
Nyckelord CARABAS, SAR, VHF, vegetationsgenomlysning, markspaning, förändringsdetektion		
Övriga bibliografiska uppgifter	Språk Engelska	
ISSN 1650-1942	Antal sidor: 72 s.	
Distribution enligt missiv	Pris: Enligt prislista	

Table of Contents

1	Introduction	1
2	CARABAS-II	2
2.1	Antenna System and Backlobe Suppression	2
2.2	Motion Compensation	4
2.3	Other Design Issues.....	4
3	Vidsel Data Collection	5
3.1	Data Collection Objectives.....	5
3.2	Ground Report.....	6
3.2.1	Data Collection Area.....	6
3.2.2	Target Descriptions	9
3.2.3	Target Deployments	11
3.3	Flight Report	13
3.3.1	Radar Parameters.....	13
3.3.2	Flight Paths.....	14
3.4	Forest Report	16
3.5	Overview of the Vidsel Data.....	17
3.5.1	Example Vidsel Imagery	17
3.5.2	Image Generation and Calibration	18
3.5.3	Image Quality Control.....	19
3.5.4	RFI Environment.....	20
4	Experimental Process	22
4.1	Image Selection	22
4.2	Change Detection Algorithm	24
4.2.1	Spatial Bandpass Filtering.....	24
4.2.2	Geocoding	24
4.2.3	Matching.....	25
4.2.4	Change Analysis.....	25
4.2.5	CFAR filtering.....	26
4.2.6	Detection Analysis	26
5	Results	27
5.1	Introduction	27
5.2	Measures of Performance.....	28
5.2.1	Declaration of a Target Detection and False Alarm.....	28
5.2.2	P_d and FAR Calculations.....	28
5.2.3	Confidence Interval Calculations	29
5.3	ROC Curves	29
5.3.1	Studies 1-4: RFI Environment and 5° Change in Heading	29
5.3.2	Analysis of ROC Curve Shape for Low Bandwidth and Small Targets	33
5.3.3	Study 5: Target Size and Bandwidth.....	37
5.3.4	Study 6: Incidence Angle	37
6	Conclusions	41
	References	42
	Appendix A SAR Image Quality Numbers	43
	Appendix B SAR Image Chips of Forest 1, 2	45

1 INTRODUCTION

This report presents results from the change detection (CD) study performed on data collected by the CARABAS-II synthetic aperture radar (SAR) at RFN Vidsel in northern Sweden between 30 May and 12 June, 2002.

The primary objective of the data collection and subsequent analysis was to provide CD performance curves of a VHF-band SAR system. A secondary objective was to increase the understanding of CARABAS-II CD data and algorithms for future research and development.

The data collection and experimentation were planned and conducted such that an understanding of performance would be obtained over various operating conditions (OCs). Operating conditions can be thought of as the dependant variable of a function. While countless OCs exist, each may be categorized into the following four classes: 1) radar sensor, 2) radar processor, 3) target characteristics, and 4) environment conditions.

The goal of the CD study was to measure performance as a function of:

- Radar incidence angle and bandwidth
- Target size and orientation
- Radio-frequency interference (RFI) level
- Change in flight heading between two images used to form a change image

The principle results of the analysis are that CD is a robust detection principle for a VHF-band SAR, in particular when the system uses a large fractional bandwidth such as the CARABAS-II SAR. Generally speaking, VHF-band CD has a capability to detect and position truck-sized targets with high confidence – both in the open and under foliage cover. The detection performance is, however, found to deteriorate under certain conditions. A significant reduction is found for near-grazing angles, i.e. above approximately 70° of incidence angle or, equivalently, below 20° of depression angle. Additionally, a significant performance loss is found for smaller-sized targets when the radar bandwidth is reduced.

The report is organized as follows. Chapters 2 and 3 provide a background and overview. The intent of these chapters is to give a perspective of the study as well as aid in the interpretation of the results. Chapter 2 includes a description of the CARABAS-II system, whereas Chapter 3 provides an overview of the Vidsel data collection.

Chapter 4 describes the experimental procedure used to process the data. It includes a description of the methodology used to select the CD image pairs as well as the subsequent CD processing.

Chapter 5 presents and discusses the results from the study. First, the measures of performance used are defined (probability of detection, P_d , and false-alarm rate, FAR). Next, the assumptions used to derive the confidence intervals for these measures are provided. Then the results are given both in the form of ROC curves as well as P_d and FAR as a function of detection threshold. Each graph shows the CD results as a function of different OCs. These results are then analyzed and discussed. Finally, conclusions are summarized in Chapter 6.

2 CARABAS-II

CARABAS-II is a second-generation, airborne, ultra-wide bandwidth, wide-beam SAR designed and operated by the Swedish Defense Research Agency (FOI). CARABAS stands for Coherent All Radio Band Sensing. CARABAS-II transmits HH-polarized waves between 20-90 MHz, which lie in the upper part of the HF band and lower part of the VHF band, corresponding to wavelengths between 3.3 m and 15 m [1]. The spatial resolution obtained, using the full signal bandwidth and an azimuth integration angle of roughly 70° , is 2.5 m by 2.5 m defined in the slant range plane. A Sabreliner aircraft hosts the sensor. Currently, the raw radar data are recorded onboard while all signal processing such as image formation, radiometric calibration, geo-coding, and change detection are performed off-line on the ground.

For several years CARABAS technology was the only flying resource with the ability to gather high-quality SAR data below 100 MHz. More recently, DARPA has contracted Lockheed Martin to develop the FOPEN SAR system operating in the UHF/VHF band [2], which includes the CARABAS band below 100 MHz.

Realization of a high-performance SAR system in this frequency range of the electromagnetic spectrum is challenging. Advances in antenna and digital receiver design as well as image formation algorithms have been crucial in the development of CARABAS-II and its predecessor. The exponential growth in signal processing power which is the foundation of SAR image formation is also fundamental to the development of CARABAS technology.

The remainder of this chapter will address some of the more important design issues.

2.1 Antenna System and Backlobe Suppression

The antennas are the most conspicuous aspect of the CARABAS-II system. In order to obtain low ohmic losses, the length of the antenna needs to be approximately half the wavelength. This has been accomplished with two rigid Kevlar push-boom antennas composed of two horizontal biconical radiating elements, which extend from under the nose of the aircraft as shown in Figure 1. The design and location of the antennas provide good aerodynamical stability, and minimize electromagnetic interactions with the airframe.

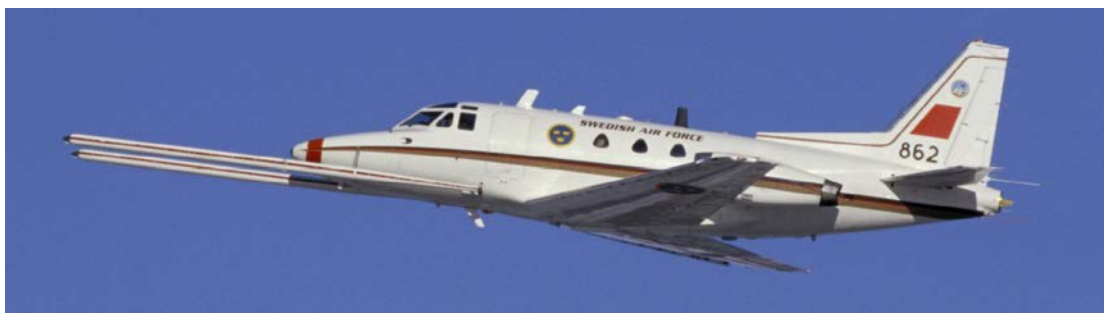


Figure 1. The CARABAS-II VHF-band SAR in operation with the antennas deployed in the front of the Sabreliner aircraft (© Photo: Swedish Defense Images / Peter Liander).

The antennas are designed to provide essentially horizontal polarization and omni-directional illumination in the elevation plane across the 20-90 MHz band. Each boom is 8 m long in

total with the 5-m long active segment extending in front of the aircraft nose. The boom separation is 1.85 m. Both antennas are fed during transmission and a delay line is used to tilt the antenna beam to the left- or right-hand side of the flight track. On receive, the signals from each antenna are simultaneously recorded in two parallel receiver channels.

The radiating elements produce a wide azimuth beam pointing in the across-track direction. The low directivity of the antenna system implies that objects on the ground will be illuminated over a very wide aspect angle, typically 90° or more. Ideally, an illumination width of 180° is present and a circular average over a semicircle segment represents each raw data sample acquired along the flight path, as illustrated in Figure 2. In reality the sensitivity of the antenna pattern fluctuates with respect to frequency, incidence angle and aspect angle.

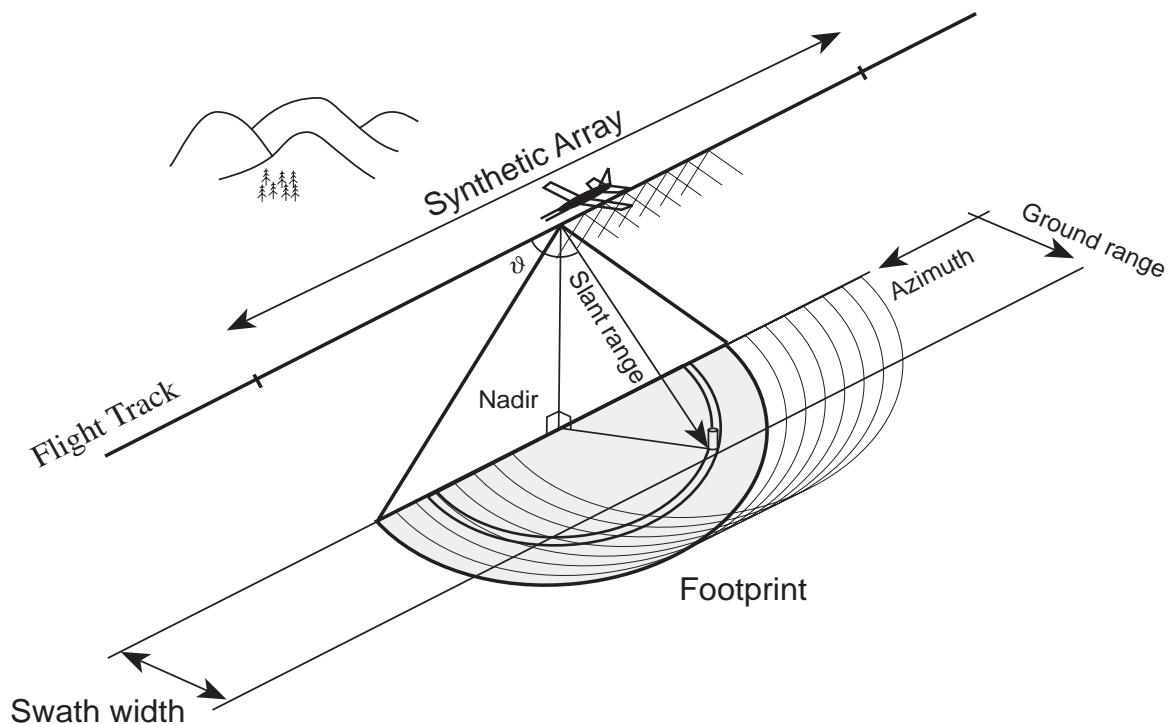


Figure 2. The basic imaging geometry for CARABAS-II. To obtain a sufficient resolution in azimuth the signal must be integrated over a large aspect angle. The effective swath in the final image is reduced compared to the raw data coverage required to carry out the corresponding inverse processing.

While the antennas are designed to allow for steering of the mainlobe to either the left or right hand side of the flight track, suppression of scatterers from the unintended side of the flight track is limited. This can give rise to strong backlobe image artifacts. Returns from sufficiently large scatterers in the backlobe will appear in the processed image, positioned according to their orthogonal distance from the flight track. Using only one antenna on receive suppresses these artifacts by approximately 10 dB [3]. Rejection of the backlobe leakage can be further improved by combining the signals from both antennas. However, this processing was not performed on the data in this study. All SAR imagery in this analysis was formed using only the returns received from the antenna closest to the target area.

2.2 Motion Compensation

Operation of an airborne wide-beam SAR may give synthetic apertures on the length of tens of kilometers. The signal processing algorithms must therefore handle long data segments in azimuth to fully utilize the Doppler information. This places stringent requirements on the accuracy and temporal drift of the navigation system to carry out the motion compensation properly. The platform position is monitored with a carrier-phase differential GPS (CDGPS) device. A ground based CDGPS receiver may be deployed within or in the vicinity of each test site or one of the national SWEPOS network [4] ground stations can be used. In this campaign, a nearby SWEPOS station was used.

2.3 Other Design Issues

A vital design issue for a VHF-band SAR system is the management of radio frequency interference (RFI). This is a two-fold problem in that the radar is required to adapt the transmitted spectrum to avoid frequency bands presently occupied by other services, e.g. air traffic control, but also have enough dynamic range on receive to ensure that strong external signal sources, e.g. TV broadcasting, can be filtered out.

The requirement to minimize harmful interference effects is implemented in CARABAS-II via a flexible digital waveform generator. This allows narrow and wide-band frequency notches to be included in the definition of the pulse encoding.

Digital receiver technology can provide the dynamic range typically needed to avoid saturation or inter-modulation from strong external sources. However, this comes at the expense of bandwidth. The solution adopted by the CARABAS-II system is to combine a high-performing digital receiver with a stepped-frequency waveform [1]. The 70 MHz signal bandwidth used by CARABAS-II is thus divided into a number of sub-bands in order to reduce the instantaneous bandwidth. The penalty is that the receiver must perform fast frequency tuning and that the ultra-wideband signal requires spectrum reconstruction. The receiver used for each antenna channel has a bandwidth of 2 MHz, and provides 14-bit output data at a sampling rate of 5 MHz. The spurious-free dynamic range of the receiver is 88 dB.

The main disadvantage for image quality of using the stepped-frequency technique is the problem of controlling paired-echo sidelobes after spectrum reconstruction. Paired-echo sidelobes occur when any significant periodic amplitude or phase ripple remains in the reconstructed spectrum. This ripple generates coherent sidelobes in the range direction. A stable system and careful calibration are required in order to reduce the effect to a satisfactory level. A calibration methodology with the purpose of reducing this effect during processing has been derived. It is based on an optimal linear filter, which maximizes signal-to-noise ratio under the constraint of a flat output energy spectrum [5].

The challenges associated with ultra-wideband and wide-beam SAR data have resulted in several signal processing research topics. For example, efficient signal processing methods in the time domain for image formation have been developed and implemented [6]. The need for this new technique comes from the large amount of contributing data samples from each ground point when illuminating with a wide antenna beam in combination with a curved flight track. New methodologies for radiometric calibration have also been devised [7].

3 VIDSEL DATA COLLECTION

The purpose of this chapter is to provide an overview of the most important aspects of the Vidsel data collection campaign. First the objectives of the data collection are reviewed. Next, the principal points from the ground, flight and forest report associated with the Vidsel data collection are discussed. The full ground, flight, and forest reports can be found in references [8], [9] and [10], respectively.

3.1 Data Collection Objectives

The goal of the Vidsel 2002 data collection was to provide the necessary data to measure the performance of VHF-band SAR change detection (CD) for targets obscured by foliage. The primary measures of performance used in analyzing a target detection system are the probability of detection (P_d) and false-alarm rate (FAR). These two measures can be combined in one graph known as the receiver operating characteristic (ROC) curve which shows P_d as a function of FAR.

One ROC curve can be generated using all the data collected at RFN Vidsel. However, this would not give insight into system performance nor would it allow for predicting system performance for data collected in regions other than RFN Vidsel. For a more thorough understanding of the data and the CD performance of the CARABAS-II system, several ROC curves were generated, each giving the P_d vs. FAR for a specific operating condition (OC).

An operating condition is a parameter associated with system performance. While the number of different possible OCs are countless, they can be categorized based upon which component of the experiment they are associated with. Thus OCs are often thought of as belonging to one of four areas: sensor, environment, target, or processor. Sensor OCs describe all parameter settings associated with the sensor platform as well as the sensor's geometry. Environmental OCs are parameters associated with the space-time being imaged such as the type of trees in the data collection area and the atmospheric conditions. Target OCs capture all aspects connected with the targets being imaged such as target size, class, orientation, and position. Finally, processor OCs describe the algorithms analyzing the data.

The use of operating conditions is an attempt to isolate the affects of performance to only one free variable. However, we readily admit even under the best circumstances, it is extraordinarily difficult to show performance as a function of only one parameter.

For this data collection several operating conditions were chosen. Specifically, performance as a function of the six parameters shown in Table 1 was studied in various combinations.

Table 1. The operating conditions over which the Vidsel 2002 data were collected.

Operating Condition	Operating Condition Class	Types of Measurements
Target Orientation	Target	Non-broadside aspect and all aspects
Target Size	Target	Small, medium, large targets
Heading Delta	Sensor	The heading change between two images to form a change image: 0°, 2°, 3°, 5°, 6°, 11°, and 13°
RFI	Environment	Low or High
Bandwidth	Processor	Analysis done over three bands: High: 25-85 MHz Medium: 25-68 MHz Low: 25-52 MHz
Incidence Angle	Sensor	58°, 63°, 68°, 72°, 75°

Careful planning was performed prior to any data being collected in order to assure that the data obtained supported analysis over these OCs. The planning included the selection of appropriate test sites, target types, target deployments, system parameters, and flight paths. The remainder of this section discusses the details of the planning as well as some examples for how the decisions made assured collecting data that supported the desired OCs.

3.2 Ground Report

The purpose of the ground report is to document the ground activity during the radar data collection. This section gives a description of the data collection area, the targets and each of the different deployments of the targets. A more complete description of the ground activities can be found in [8].

3.2.1 Data Collection Area

The data collection campaign was conducted at RFN (RobotFörsöksplats Norr) Vidsel, a military test range located south west of the town Jokkmokk, as seen in Figure 3. The data used in the present analysis is a subset of the data collected.

Used primarily for practice firing and testing of airborne and surface launched missile systems, the RFN facility is part of the largest proving ground found on land in Western Europe. The geographic location of the test range is in northern Sweden, close to the Arctic Circle and just east of the mountain range on the border of Norway.

The restricted ground area inside RFN Vidsel was surveyed in preparation for the radar campaign, in search of appropriate locations for the target deployment. The primary criterion in this process was to locate the densest forested areas inside RFN Vidsel. The prevailing altitude and climate found in this part of Sweden result in sparsely populated forests comprised primarily of small- to medium-sized trees.

Only a limited number of potential target deployment sites were found. The target deployment sites were additionally restricted to areas adjacent to roads. This was done to help facilitate relocating the targets into various deployment scenarios that were planned during the course of the campaign. This directed the final choice to a region on the west and north of a fresh water lake, Naustajaure.

Two mature forest parcels, found on predominantly level ground, were utilized to establish various configurations of targets concealed in foliage. The approximate extent of the two sites, labeled Forest 1 and Forest 2, respectively, has been added as grayish segments on the map shown in Figure 4.



Figure 3. The shaded rectangular area is the data collection area located southwest of Jokkmokk, Sweden (Map: http://www.norden.org/web/1-1-fakta/sv_kort.htm).

Forest 1 was used for target deployments Gustav (A5), Johan (A6), Fredrik (A3) and Adolf-Fredrik (A4). Forest 2 is located about 2 km north of Forest 1 and was the site for target deployments Sigismund (A1) and Karl (A2). The foliage in both of these regions consisted mostly of Scots pine with diameters up to roughly 25-30 cm and a stem volume of roughly 100 m³/ha. Aerial photos with the GPS positions of target locations in all the forest stands used for target deployments are shown in Figure 5.

At the southern end of the road crossing through Forest 1 there are grass fields with some buildings from an abandoned farming hamlet known as Nausta. The open fields and close proximity to the two forest sites made Nausta well suited for the location of a trihedral. This trihedral allows for in-scene radiometric calibration of all generated SAR images covering the main area of interest depicted in Figure 4.

Another advantage with the selected test site is the hill, Naustapuouta, found in the northeast corner of Figure 4. The slopes are forest covered except near the peak. The forest quality characteristics are similar to the surrounding lowlands. Although not done within the present study, the radar data corresponding to the hill can be used to explore the effect of terrain relief clutter on CD performance. Figure 6 shows a photo taken from the hill towards the lake and the Nausta peninsula. The clearing in the middle denotes the location of Nausta. This image also reflects the typical landscape of the test range, i.e. moderate topographic undulations reaching heights in the range of 400 to 800 m, many small lakes, sparse forest with medium-dense sub-regions, and open areas dominated by marshlands. Finally, besides being a test range, most of the terrain at RFN Vidsel is also a protected nature reserve and is therefore moderately affected by silvicultural actions, e.g. clear-cuttings and thinnings.






Figure 6. View from the top of Naustapuouta hill. The large grass field seen on the peninsula is the Nausta hamlet and was used for deployment of targets in the open, as well as a trihedral for calibration purposes.

3.2.2 Target Descriptions

Twenty-five vehicles were made available from the military garrison in Boden to participate and form target deployments during the experiment period. The request to the Army asked for vehicles of three different sizes, as well as vehicles designed for movement in normal terrain conditions. Three different target models were provided. Each model corresponds to one of the desired classes of small, medium and large. Table 2 provides a summary of each target type.

Table 2. Overview of the target types used during the Vidsel data collection.

Name	L (m)	W (m)	H (m)	Role	#	Image
TGB11	4.4	1.9	2.2	Personnel transport	10	
TGB30	6.8	2.5	2.9	Equipment transport	8	
TGB40	7.8	2.5	2.9	Equipment transport	7	

The terrain vehicle model TGB11 was used for the small target class. The TGB11 has jeep-like dimensions but with a more cubic shape, i.e. 4.4 m long, 1.9 m wide and 2.2 m high. The primary use of the TGB11 is transportation of military personnel. Ten units of this type participated in the deployments.

The TGB30 comprised the medium class. The TGB30 is a terrain vehicle with a truck-like design. The TGB30 has the following dimensions, length of 6.8 m, a width of 2.5 m and a height of 2.9 m. Eight TGB30s were used in the target deployments. Different versions of the TGB30 exist depending upon the configuration of its truck bed. Four different configurations of the TGB30 were used in the collection; one with a booth, one with 2 fuel tanks, three with covers, and three in a standard configuration.

The large target class was comprised of terrain vehicle model TGB40. The TGB40 has the same basic design as TGB30 but is extended in length to 7.8 m and equipped with a third axle in the rear. The seven different TGB40s used during the data collection came in three different configurations; four had booths, two were in the standard configuration, and one was a flatbed.

Note that the difference in dimensions between the medium and large class is not substantial. As expected, the results from the data evaluation show that in general, the effect on performance due to target size is more pronounced between the small and medium target classes than between medium and large target classes. Photos of the three terrain vehicle models concealed in foliage are found in Figure 7. The pictures also give an idea of the forest density for the two sites.

Apart from the vehicle targets, three trihedrals with sides 5-m in length were deployed in the open. Two were kept at a fixed orientation, whereas the third was rotated manually. The rotation was performed in advance of each sensor pass to ensure the center of the trihedral pointed in a direction perpendicular to the flight path. The trihedral that was adjusted between sensor flights can be seen in place in Figure 7. The forest-covered hill Naustapuouta, mentioned earlier in this report, is also visible beyond the lake.



Figure 7. The terrain vehicle models TGB40 (upper left), TGB30 (upper right) and TGB11 (lower left). The deployed trihedral in Nausta (lower right) was adjusted for each flight pass to allow radiometric calibration.

The locations of the trihedrals were well separated within the imaged area and their positions were measured with GPS. Comparison of the estimated trihedral locations after geo-coding with the measured GPS locations enables the accuracy of the geo-coding to be determined.

3.2.3 Target Deployments

Six target deployments were used in collecting the data analyzed in this report; four were set up in Forest 1 and two in Forest 2. In combination with variations of the imaging geometry, such as incidence angle and flight heading, the target configurations in the different deployments were varied as well. These variations in imaging geometry and target deployment were designed to allow for a systematic evaluation of CARABAS-II change detection performance as a function of numerous operating conditions.

In two of the deployments (Gustav and Johan) all vehicles were randomly oriented, whereas in other deployments all targets had the same orientation. In the case where all vehicles had the same orientation, the target orientation for that deployment was chosen so that a particular operating condition could be measured and was dependent upon the flight paths of the sensor.

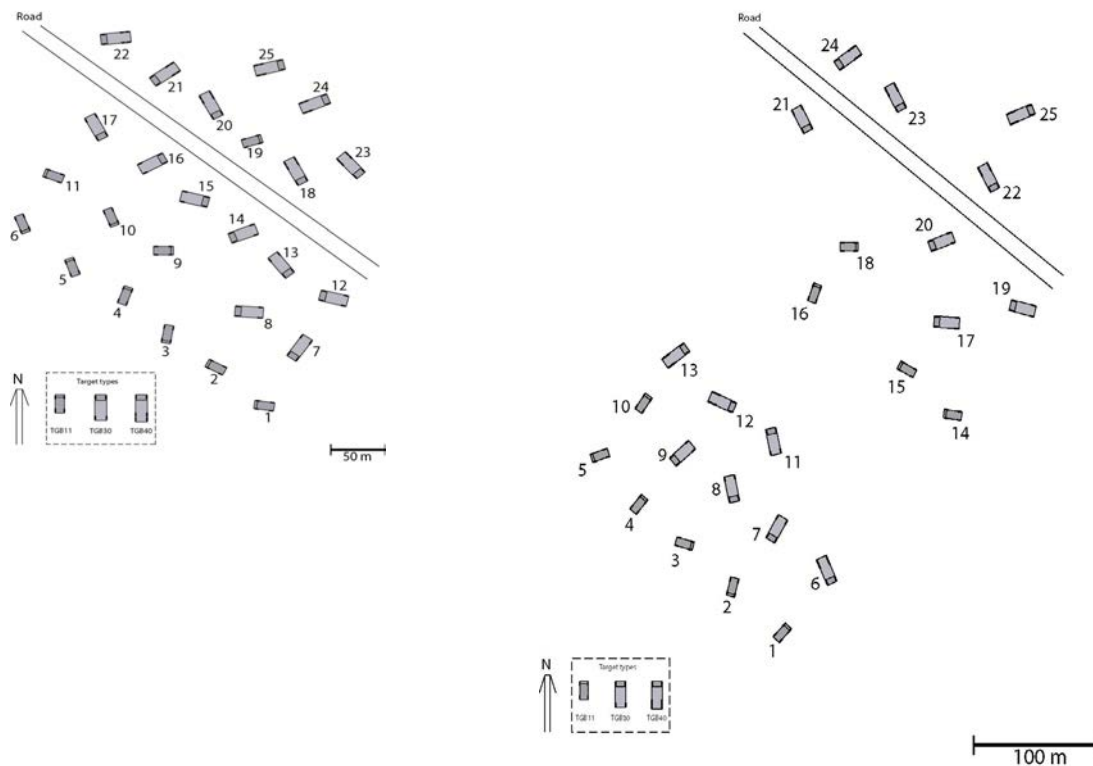


Figure 8. Sketch of deployments Gustav (left) and Johan (right) realized inside Forest 1. The 25 terrain vehicles in these two deployments have been given a random orientation. Note that twelve of the targets have nearly the same position in the two deployments (Gustav 1, 2, 4, 8, 9, 12, 14, 17, 18, 20, 21, 24 corresponding to Johan 14-25).

Every target position was marked with a wooden stake while the target was present. Accurate geographical coordinates of the corresponding positions were retrieved afterwards by use of carrier-phase differential GPS measurements. However, the interaction with the vegetated layers introduced a high root-mean-squared error in a few GPS positions despite the long period of integration. After inspection of these positions, it was concluded that only one target position needed correction before detection analysis could be performed. The corrected GPS position corresponds to Gustav 9 and Johan 18 in Figure 8.

Besides target positions, other parameters such as heading, pitch and roll were measured for every vehicle in each deployment. Other means of documentation include photographs from a number of views for every target in position and in a few cases an overview of all deployed units was gathered with an airborne camera. Table 3 provides an overview of the relevant target deployments used during the data collection.

Table 3. Overview of the relevant target deployments used during the Vidsel 2002 data collection. In this table, missions refer to flight mission numbers for which the target deployment was imaged.

Deployment	Missions	Site	Objective
Sigismund	2	Forest 2	Detection vs. RFI and target orientation
Karl	3	Forest 2	Detection vs. RFI and target orientation
Fredrik	4	Forest 1	Detection vs. RFI and target orientation
Adolf-Fredrik	5	Forest 1	Detection vs. RFI and target orientation
Gustav	7,8,9,14	Forest 1	Detection vs. incidence angle
Johan	11,12,13	Forest 1	Detection vs. incidence angle

3.3 Flight Report

The previous section described details of the ground activities during the Vidsel data collection. This section provides a general reference on the details of what occurred in the air. Specifically, flight paths, geometries and sensor parameters are discussed. More details are available in reference [9].

3.3.1 Radar Parameters

Sixteen successful missions were conducted, resulting in 150 radar passes. A subset of these measurements, i.e. from eleven missions, was used to perform the analysis in this report. The main system parameters associated with the radar mode operated during the field campaign are summarized in Table 4.

Table 5 provides a temporal representation for when the data was collected as well as comments on a few of the missions.

Table 4. The CARABAS-II sensor settings used during the Vidsel data collection.

System Parameter	Value
Nominal flight altitude	3 - 6 km
Nominal ground speed	127 m/s
Frequency band	20 - 86 MHz
Transmitted power (peak)	500 W
Pulse modulation	Non-linear FM
Frequency sub-bands	35 (36 with RF-sniff)
Frequency step	1.875 MHz
Centre frequencies	21.25 - 85 MHz
Pulse repetition frequency	5000 Hz
Pulse length	15 μ s
Duty cycle	7.5 %
Maximum range	26.4 km
Transmit notch	74.8 – 75.2 MHz
RFI sniff	On

Table 5. A timeline showing when the data used in this report was collected.

Day	Time	Mis.	Deployment	Comments
31/5 Friday	11-13	9	A5: Gustav	
	14-16	7	A5: Gustav	
2/6 Sunday	03-05	14	A5: Gustav	Night flight
	06-08	8	A5: Gustav	
6/6 Thursday	08-10	13	A6: Johan	Pass 7,8 missing due to airspace conflicts
7/6 Friday	08-10	11	A6: Johan	Pass 9 at FL200 instead of FL170
	10-12	12	A6: Johan	
10/6 Monday	11-13	2	A1: Sigismund	
	15-17	3	A2: Karl	
11/6 Tuesday	11-13	4	A3: Fredrik	
	15-17	5	A4: Adolf-Fredrik	

The flight program to image the deployment area was derived using one radar aim point located on the road within Forest 1.

Table 6 shows the three different flight geometries used for collecting the data which supports this report. The need for different geometries came from the desire to study performance as a function of incidence angle. Different incidence angles were obtained by varying the altitude of the aircraft while keeping the slant range distance to the aim point fixed at 12 km. By keeping the slant range distance constant, the nominal signal-to-noise ratio (SNR) will be constant. This gives a fair comparison of CD as a function of incidence angle.

Table 6. The incidence angle geometries of the Vidsel 2002 data used in this report.

#	θ_{AP}	Altitude above ground (km)
1	58°	6.4
3	68°	4.5
4	72°	3.7

The length of each imaging flight path was typically 37 km. This length was chosen to ensure sufficient variation of aspect angle to form images within a ground segment of approximately 10 km by 10 km, centered on the aim point.

Some imaging passes were redundant measurements in that they contained the same flight geometry and target deployments. This was done deliberately in order to investigate temporal scene stability.

3.3.2 Flight Paths

The final variable associated with the flight geometry is the heading of the aircraft. Each mission had multiple passes.

Two criteria were used for choosing the headings of the different flight passes. First, in order to determine the impact of RFI on CD performance, some headings were chosen such that data was collected in both low and high RFI environments. Second, headings were chosen

such that change images could be formed from two images having slightly different headings. This criterion was used for the selection of flight headings in order to measure CD performance as a function of the delta in heading between two passes. Figure 9 gives two examples of flight paths.

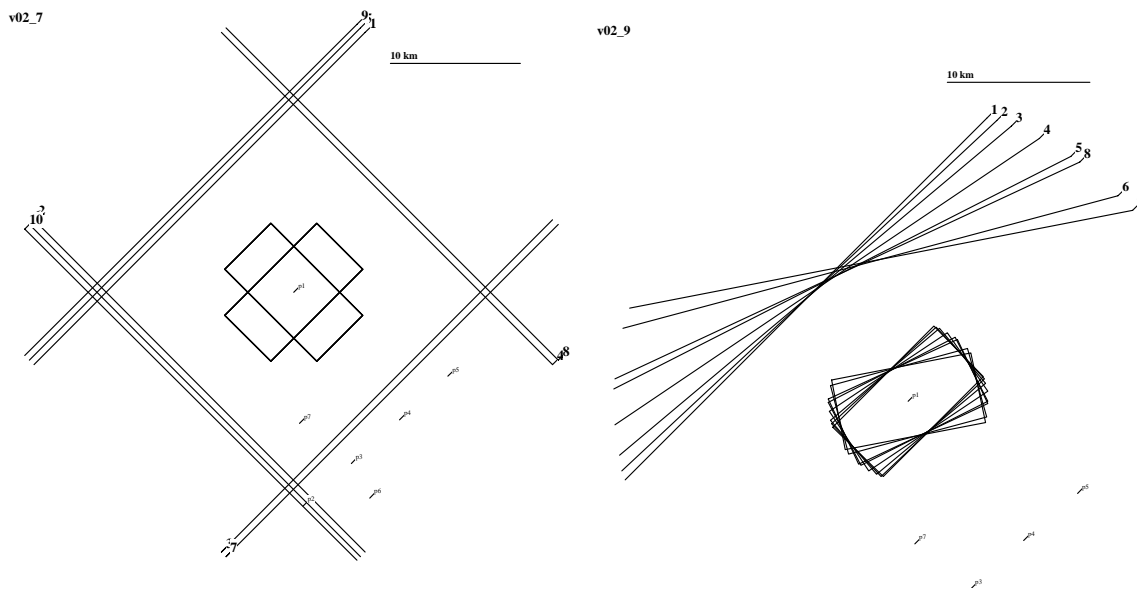


Figure 9. The lines in each figure represent flight paths. The boxes represent the imaged area. Adjacent but shifted flight paths correspond to changes in incidence angle while preserving the same stand-off range. The cardinal passes shown in the image on the left ensure that the primary RFI source, which was located to the southeast of the imaging area, would be in the main, back, and side lobes of the antenna. This flight path structure allows for estimating CD performance as a function of RFI environment. In the figure to the right, the heading is instead changed in small steps whereas both the stand-off range and incidence angle are constant. This set of passes allows for studying the impact of changes in flight heading on change detection.

RFI was measured both through the use of RFI sniffing pulses interleaved during a data run as well as in the raw radar data. In Sweden, three low-VHF TV channels (channels 2-4) are normally found between 47 and 68 MHz which provide significant external RFI sources. The nearest TV broadcasting antenna (channel 4) was located approximately 150 km southeast of the aim point. The location of this antenna as well as other low-VHF TV transmitters can be seen in Figure 10. To explore the effect of RFI on CD performance, four cardinal headings were chosen such that the effect of RFI on the images should vary significantly. More detail on the RFI is given in Section 3.5.4.

Because all data used in this analysis was collected by illuminating the ground to the left of the flight path, a flight heading of 225° pointed the radar antennas' main beam in the direction of the nearest low-VHF TV transmitter. Thus this heading was used to collect data with a large RFI. A few passes at a heading of 45° were also collected to see the effect of a strong RFI in the backlobe. Since there is only one close low-VHF TV transmitter, a lower RFI environment occurs when flying directly towards or away from it, i.e. placing it outside of the main beam. Thus headings of 135° and 315° were both collected to represent a low RFI environment.

To collect data to explore the effect of changes in heading on CD performance, several passes were flown with small deviations from 225° . Specifically, headings of 227° , 230° , 236° , 243° , and 255° were collected. These will provide data with high RFI as well. Since this represents the hardest environment, the numbers provided in this analysis should give a pessimistic bound on the performance of the system as a function of heading delta.

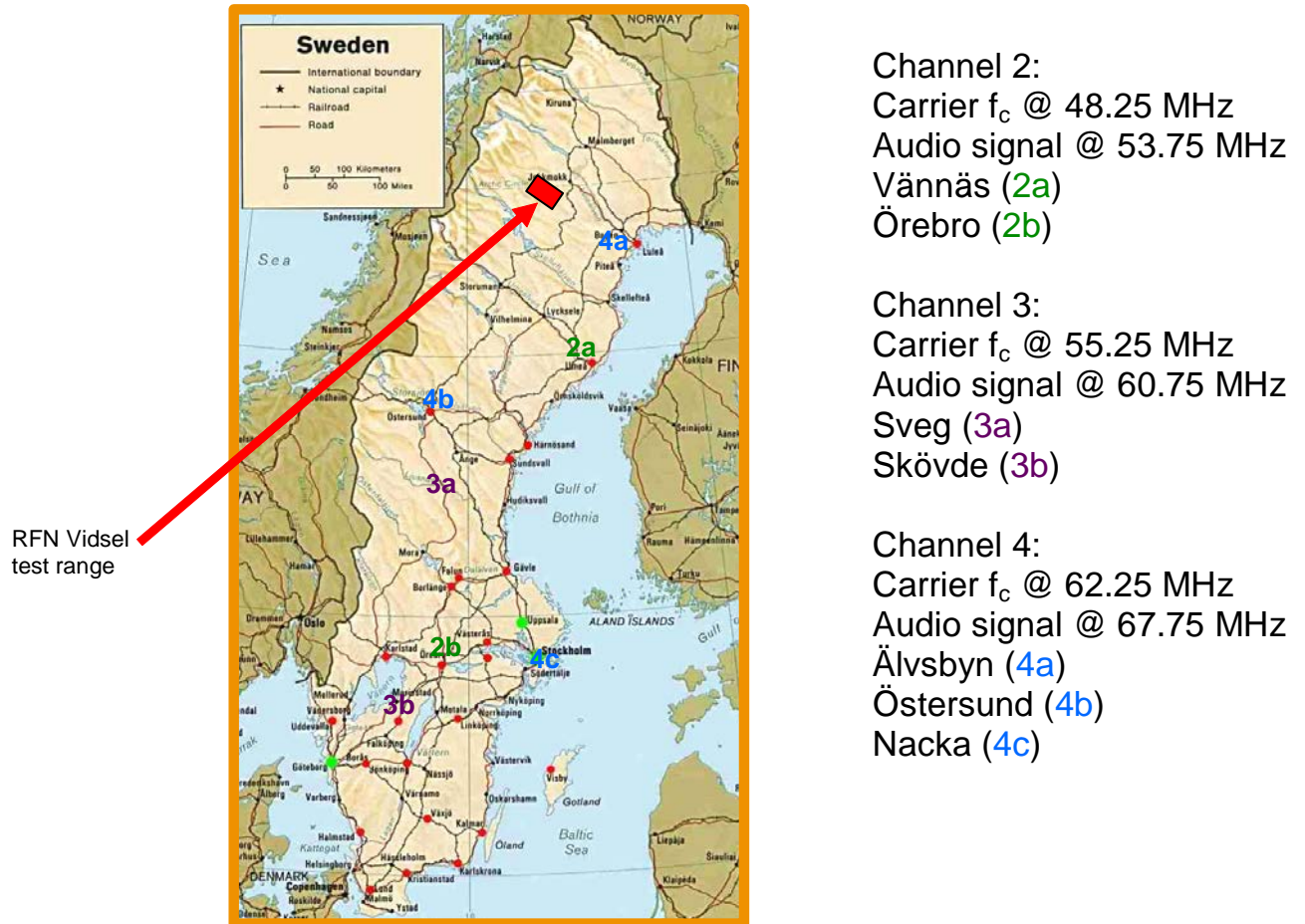


Figure 10. Location and center frequencies of low-VHF TV transmitters in Sweden (Map: <http://www.uu.se/Univ/Sweden.eng.html>).

3.4 Forest Report

A careful and detailed forest inventory of the two deployment parcels was performed after the completion of all radar measurements [10]. The dominating tree species (99%) was found to be Scots pine. Other existing species are birch and Norway spruce. The forest in this region has a rather low yield, with an average annual timber production of approximately $2 \text{ m}^3 \text{ ha}^{-1}$. The dominant soil type is till, i.e. coarse and mainly podsollic soil of glacial origin, and has a mineral content dominated by quartz. The field layer consists of mainly lingonberry and lichens. The ground elevation in the forest parcels exhibits a variation in the interval of 470-500 m above sea level.

As seen in Figure 5, Forest 1 was divided into three smaller stands while Forest 2 was divided into two stands. Each of the five stands was chosen to define homogenous forest regions. The

forest inventory provided stand-wise averages of important forest parameters, e.g. stem volume, stem number density, tree height, and stem diameter, which are presented in Table 7.

Table 7. Vidsel average forest stand parameters. Stands 1-3 refer to Forest 1, and stands 4-5 to Forest 2.

Stand	1	2	3	4	5
Average elevation (m)	490	480	480	500	500
Volume (m ³ /ha) - living trees	94	111	134	67	96
Volume (m ³ /ha) - dead trees	4.4	0.8	0.9	1.7	1.7
Growth (m ³ /ha/yr)	1.2	1.4	1.5	1.5	1.8
Stem Number (stems/ha)	177	247	314	314	365
Height (m)	16.2	16.6	16.0	13.2	14.0
Diameter (cm)	32	29	28	24	26

Detailed measurements of individual tree positions and characteristics were made within a 10 m radius of each target location. This makes it possible to create detailed models of the forest nearby each deployed target.

3.5 Overview of the Vidsel Data

This section describes the data used in the CD analysis performed in this report. This is accomplished through a discussion on image formation and calibration, the image quality of the Vidsel data, the existing RFI environment during this collection, and by providing an example SAR image.

3.5.1 Example Vidsel Imagery

Figure 11 gives an example of a geo-coded CARABAS-II SAR image collected at Vidsel. The aircraft flew on a south-western course illuminating the area from the upper left side.

The main layout of the landscape is readily identified when compared to the map in Figure 4. The noise-limited low signatures are produced by the lake, swampy ground, and open fields. The forest covered areas exhibit an intermediate intensity level, whereas the strongest contributions correspond to man-made structures. Examples of the latter are the complex of buildings and other objects at Nausta.

The most noticeable visible features are likely the bright, linear segments. They correspond typically to fences or various types of overhead lines and appear as long as the integrated data include Doppler frequencies perpendicular to the main orientation of such an extended object.

Figure 11 also includes a target deployment in Forest 2. It consists of the 25 terrain vehicles concealed in foliage and can easily be identified. These 25 targets are seen in the mid-upper part of the image as a 5x5 grid of bright points.

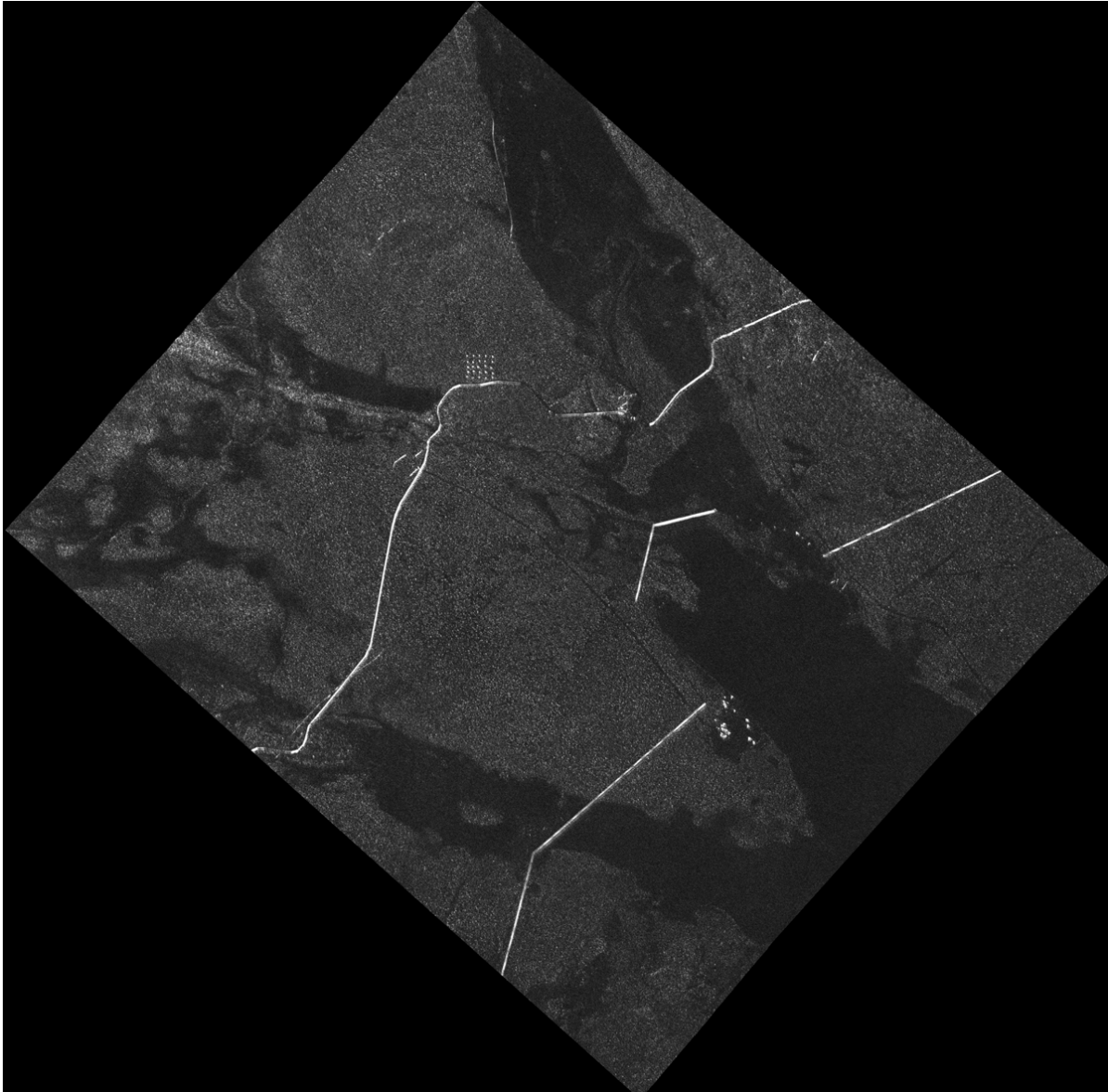


Figure 11. A geo-coded CARABAS-II VHF SAR image over the experimental area, covering all deployment sites used during the campaign. The image generated is from Mission 2 Pass 1, which used target deployment Sigismund. This deployment is the 5x5 grid of bright points visible in the mid-upper region of the image.

3.5.2 Image Generation and Calibration

The radar data have been processed using the standard CARABAS-II SAR processor, which includes pulse compression, spectral summation, RFI filtering and fast factorised back-projection (FBP) modules. The input to this process is the raw radar data stored on tape or hard disk, and the output is a slant range complex SAR image. More details of the image formation and calibration may also be found in [6] and [7].

The image generation starts by extracting a raw data segment centred at the flight track position which is closest to the selected aim point. The segment length is chosen to comply with the desired aperture angle over the imaged area. The number of aperture positions was chosen to 32768 with a spacing of 0.9375 m in all the images formed for the present report.

For each equidistant aperture position and frequency band, a pulse echo is formed by linear interpolation of the two closest raw pulse echoes along the flight track. The resulting pulse echo is then matched filtered using a pulse replica obtained from a calibration recording. Thereafter, full bandwidth data are formed by spectral summation and normalised to equalise the spectral response using the calibration recording. The output from this process is the “unfiltered t-file” where each line corresponds to a full-bandwidth pulse echo for each aperture position. The t-file data are stored as a function of range frequency and azimuth position. Each line is also accompanied by a GPS position in a separate file.

The RFI noise is filtered using a Wiener filter approach. The average energy spectrum in the range frequency dimension along the flight track is computed and its reciprocal is applied to each line of data. The output is the “RFI-filtered t-file” with the same format as the unfiltered t-file.

The next step corresponds to azimuth compression using the FBP algorithm. A line of data in the t-file is zero-padded, transformed to time domain, and then recursively summed with neighbouring lines to produce the final output slant range image. The data are back-projected onto a flat and horizontal Earth model passing through the selected image aim point and then geometrically projected into slant range coordinates.

The last step of the image formation is radiometric calibration based on in-scene trihedrals. The calibration starts by extracting an image chip around a trihedral which is Fourier transformed to 2-dimensional frequency domain. This response is compared to an ideal trihedral response computed using the finite-difference time domain (FDTD) method and a correction filter is determined. The full image is calibrated by filtering, scaling and finally applying a correction for the range-spreading loss. No correction is applied for the antenna elevation pattern since measurements have shown this effect to be small within the normal swath. The radar-cross section (RCS), in units of m^2 , of the resulting pixel is then determined by the magnitude square of the corresponding complex image pixel value. More details may be found in [7].

3.5.3 Image Quality Control

For the purposes of this report, we consider the following four image quality (IQ) measures: Noise power, trihedral 3 dB width in azimuth (cross-range), trihedral 3 dB width in slant range, and trihedral 3 dB contour area. The noise power gives a measure of overall image noise, whereas the remaining three measures provide understanding on the resulting resolution of the imagery.

The noise power level is defined as the noise-equivalent average radar-cross section and is measured over an extended area in units of dBm^2/m^2 . The 3 dB widths are computed by interpolating the trihedral response and measuring the half-power full width along the two cardinal (slant range and azimuth) directions through the peak response. Finally, the 3 dB contour area is computed by interpolating the trihedral response and measuring the area within the half-power border around the peak response.

The average noise power level was measured to $-19.1 \text{ dBm}^2/\text{m}^2$, and Figure 12 shows a histogram of the noise power across the imagery. Measurements of the average 3 dB resolution in slant range and azimuth gave 2.7 m and 3.0 m, respectively, and the average 3 dB contour area gave 6.2 m^2 .

Appendix A contains a full list of all images used in the analysis for the present report together with IQ numbers and the nominal flight heading for reference.

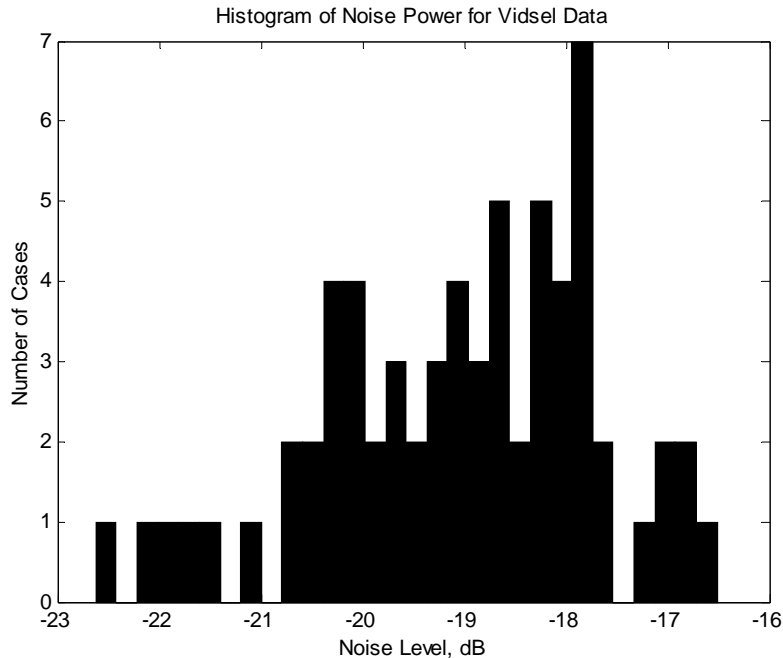


Figure 12. Histogram of the noise power of the Vidsel imagery.

3.5.4 RFI Environment

As mentioned in Section 3.3.2, various flight headings were chosen such that both low and high RFI environments would be encountered. This section describes the resulting RFI environment as a consequence of flight heading.

The RFI environment was measured by examining the average range spectral power of a given pulse-compressed data file. Because RFI is the largest contributor to spectral shaping, it has the largest effect on the shape of the RFI filter. Thus the inverse of the RFI filter can be viewed as an indicator of the RFI environment.

Figure 13 shows the averaged RFI environment for missions 2 through 5 as a function of the different headings used. First note the spike in all three headings at roughly 22 MHz. This can be identified as short-wave radio broadcasting. Next, notice the narrow-band video carrier within the three low VHF-band TV channels at 48.25 MHz, 55.25 MHz, and 62.25 MHz. Notice also the narrow-band signals associated with the audio carriers at 53.75 MHz, 60.75 MHz, and 67.75 MHz, respectively. Finally, the color information is modulated on a suppressed carrier located at 4.43 MHz above the video carrier and thus appears centered at 52.68 MHz, 59.68 MHz and 66.68 MHz.

There is substantially more energy in TV channel 4 when the flight heading is 225° or 230° compared to a heading of 135°. This occurs because the radar antenna main lobe is facing the

closest low VHF-band TV broadcasting antenna. In the case of a flight heading of 135° , there is more than a 25 dB reduction in the signal level from TV channel 4.

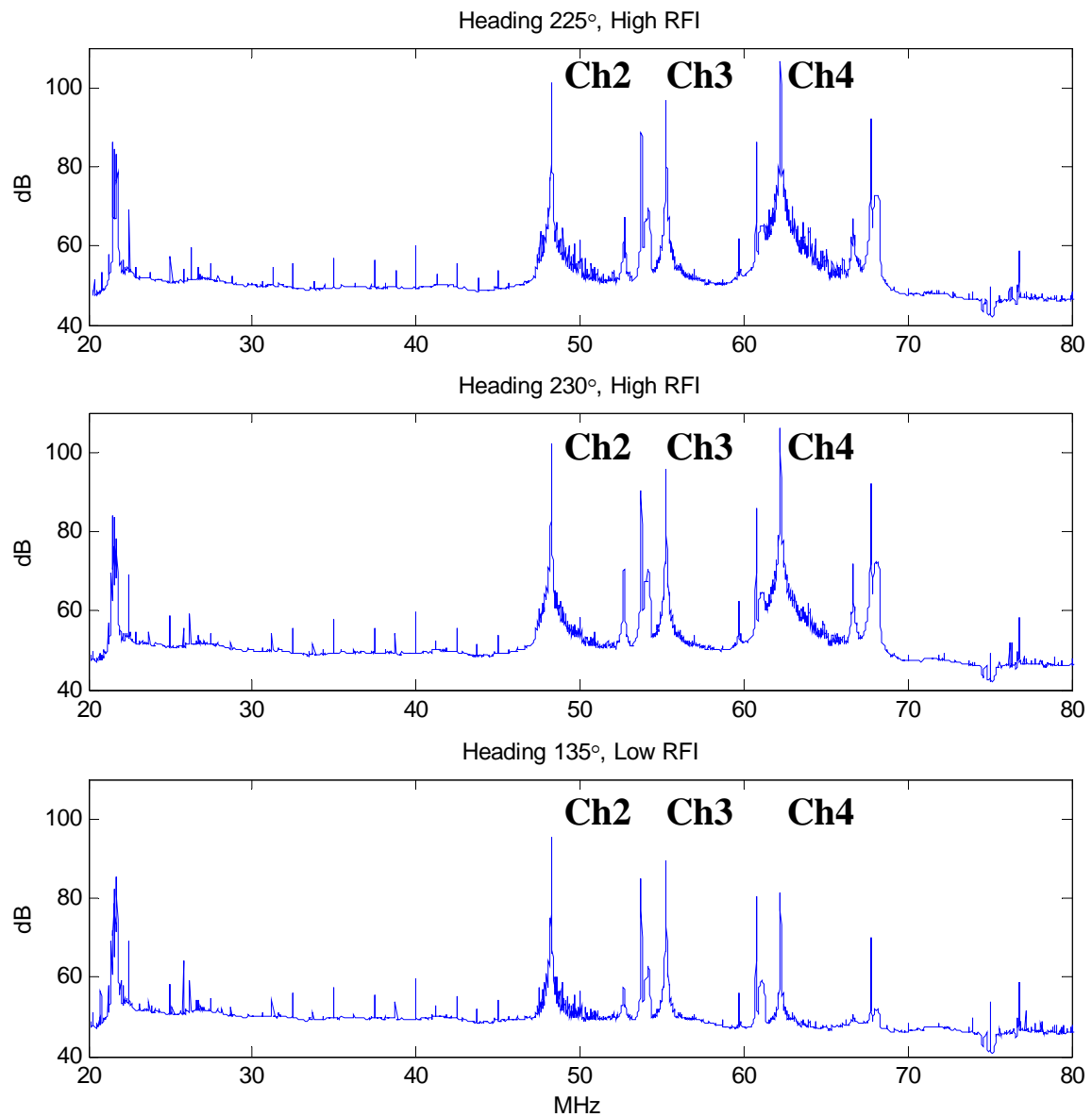


Figure 13. Average RFI environment as a function of aircraft heading. The three 7-MHz TV-channels 2-4 are clearly seen including the two carriers (video and audio) and associated modulation signals.

4 EXPERIMENTAL PROCESS

4.1 Image Selection

Over the course of the eleven missions flown at Vidsel in support of this analysis, the CARABAS-II system collected 84 usable image passes. The agreement between Sweden and the US which helped to fund this work stated that data from 56 passes would be delivered by FOI to the US. Thus the data needed to be prioritized in order to choose the 56 images for delivery.

The goal is to choose the 56 images which provide the best understanding of CD performance. The criterion used to achieve this was to select those images which provided the best statistical sampling of the data across the different OCs being investigated. This can be accomplished by understanding how the data is distributed as a function of various OCs and comparing it to the desired ROC curves.

The first approach used to select images for the CD study was as follows. First, a matrix was generated where each row represents a valid image pair and each column represents a desired ROC curve. Each element of the matrix is either a zero or one depending upon whether or not an image pair can be used to generate a desired ROC curve. Using this information, it is possible to rank the images based upon the number of times they can be used in generating the desired ROC curves. Unfortunately, although this approach is straightforward it is flawed because there is no guarantee that the resulting subset of images chosen will provide sufficient number of image pairs for each desired ROC curve.

Thus a more involved approach for image selection must be followed. The approach used in selecting the best images for delivery is given below. First, as alluded to above, all possible image pairs from the 84 image passes collected were generated. Next, many of these were eliminated by constraining the pairs to only those useful in this analysis. The logic used to parse down the total number of pairs included the following:

- Remove all image pairs using the same image, i.e. A,A.
- Keep only one of the image pairs A,B and B,A.
- Each image must come from a different deployment to ensure target movement.
- Both images must have the same nominal incidence angle.
- The difference in the headings between the two images must be less than 15°.

These restrictions provided a list of 486 valid image combinations.

Next, each of these image pairs was compared against the desired ROC curves, where each ROC curve is specified by its OCs. Note that only four of the six OCs mentioned in Table 1 affect image selection. Firstly, target size has no affect on image selection because all targets were present in each image. Secondly, bandwidth does not affect image selection since different bandwidths are generated by filtering the data. The remaining four OCs were used to decide whether or not each image pair was suitable to be used in producing each of the desired ROC curves.

The matrix generated by this process was sparsely populated, implying that the above procedure did not provide an obvious way for selecting 56 images. Then it was noted that

many of the image pairs had the exact same geometries in terms of their incidence angles, headings, and target deployments used. This means that each of the image pairs should produce the same difference image, except for variations due to temporal changes in noise and RFI. Thus many of these image pairs could be discarded with only minor effects on the statistical confidence.

The selection of which of the redundant image pairs to remove was done by balancing two criteria: 1) keeping the number of image pairs across each of the missions flown as uniform as possible and 2) keeping the number of image pairs across each of the desired ROCs as uniform as possible. The first criterion ensures the best temporal diversity of the data which helps ensure the best statistical sampling across the entire data collection. The second criterion guarantees the best sampling of the data to ensure statistical significance for each of the desired ROC curves.

A flowchart of the entire image selection process is given in Figure 14.

Even after the manual balancing, it was determined that an additional 8 images were needed to ensure a sufficient number of samples across each desired ROC curve. The analysis described in this report is therefore based on a total of 64 images.

The file names of all 64 images are listed in Appendix A. Furthermore, Appendix B shows two sub-images for each of the analyzed 64 images together with information on flight heading and nominal incidence angle. The sub-images show the two areas (Forest 1 and 2) used as target deployment sites.

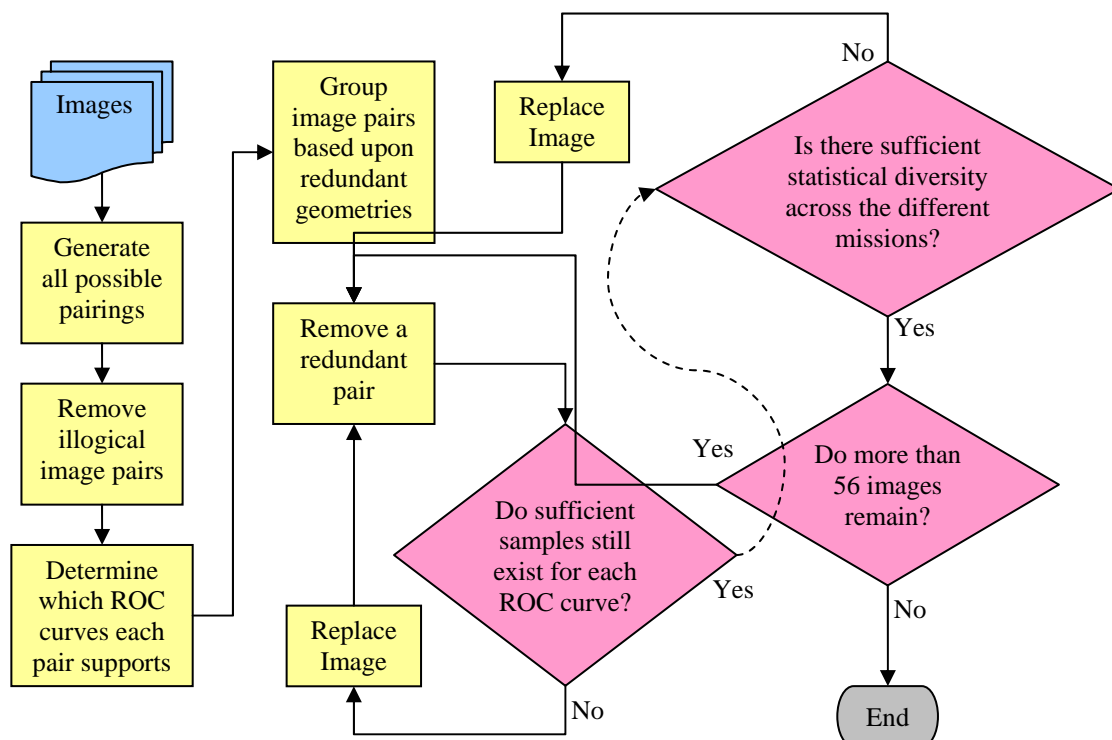


Figure 14. A flowchart of the image selection process used for this analysis.

4.2 Change Detection Algorithm

The CARABAS-II CD processor includes six principal processing steps:

- spatial band-pass filtering (“pie filtering”),
- geocoding,
- image matching,
- change analysis,
- CFAR filtering,
- detection analysis.

The processing chain, as seen in Figure 15, runs automatically, starting with two slant range images as input to the spatial band-pass filter module (“pie filter” module) and is completed after the detection analysis step. The output from the CD process is coordinates of potential targets. When analyzing the performance of the process each coordinate is compared with the ground truth of known targets to give statistics of detection probability and false-alarm rate. This section briefly describes each step of the CD process.

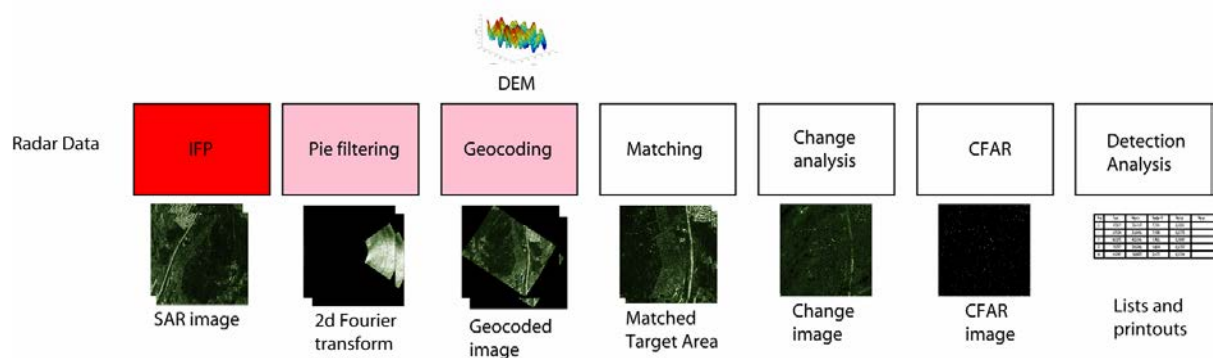


Figure 15. CARABAS-II Change Detection processor. The input is two slant range SAR images. First step is pie filtering to form images with the desired bandwidth. The second step is geocoding to project images to a map coordinate system. A matching algorithm then occurs to ensure that the images coincide. Thereafter, change analysis is performed to give the optimum linear combination of the two images. Finally, a CFAR image is formed, potential targets detected and a coordinate list produced.

4.2.1 Spatial Bandpass Filtering

The first step in the CD process is to filter the slant range images with a band-pass filter to produce images with desired bandwidth. The filter is defined in the frequency domain as the intersection between a circle sector and an annulus. Optionally, an amplitude taper may be applied to reduce impulse response side-lobe levels.

4.2.2 Geocoding

The geocoding transforms the SAR slant range images to map coordinates. The SAR imaging and processing geometry as well as a digital elevation model (DEM) of the ground are required input. The CARABAS flight track positions are recorded using carrier-phase differential GPS with accuracy of the order of a few decimeters.

4.2.3 Matching

The images to be used for change detection will not have a perfect match even after geocoding. This is mainly caused by inaccuracies in the flight track and DEM data. Therefore, a module is included which matches the images based on finding the cross-correlation peak. The images are split into smaller blocks and the necessary shift is determined for each block.

4.2.4 Change Analysis

The aim of the change analysis step is to transform the geocoded SAR images in such a way that changes (candidate targets) are enhanced whereas the stationary background is suppressed. In the change detection process, this is accomplished by combining a SAR image pair into an optimum change image. In the ideal case when the background is identical in both images it would suffice to form the change image by subtracting one image from the other. In reality, however, spatial and temporal decorrelation as well as other factors contribute to different image realizations. Hence, subtracting the images may yield poor results.

In the present work, an optimum combination of images is found in the sense of Bayes linear classification as illustrated in Figure 16. The class boundary is defined by maximizing the separation between the target and background classes [11], according to the following algorithm:

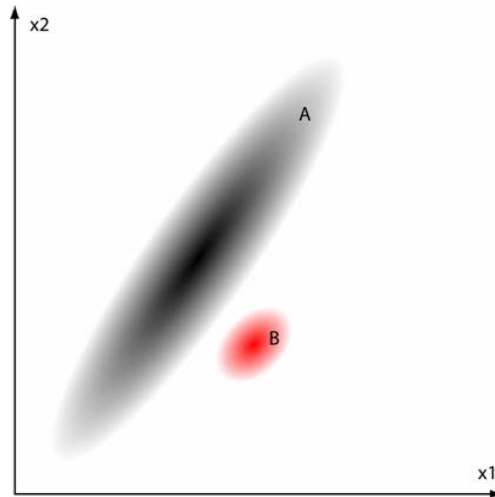


Figure 16. The two-dimensional feature vector of the image pair are assumed to belong to either of two classes, the background class (A) and the target class (B).

Convolution of each image with a smoothing kernel to reduce noise.

Form feature vector according to

$$X = \begin{bmatrix} x_1 \\ x_2 \end{bmatrix}$$

The mean and covariance of X for $i \in [A, B]$ is given by

$$M_i = E\{X|i\}$$

$$C_i = \text{Cov}\{X|i\}$$

Determine the linear combination $\mathbf{v}^T \mathbf{X}$, which maximizes the separation between the background class (A) and the target class (B), i.e.

$$\max \left\{ \frac{(\eta_A - \eta_B)^2}{P_A \sigma_A^2 - P_B \sigma_B^2} \right\} \Rightarrow \mathbf{v} = (P_A C_A + P_B C_B)^{-1} (M_B - M_A)$$

where

$$P_i = \text{a priori probability for class } i$$

$$\eta_i = E\{\mathbf{v}^T X_i\} = \mathbf{v}^T M_i$$

$$\sigma_i = \text{Var}\{\mathbf{v}^T X_i\} = \mathbf{v}^T C_i \mathbf{v}$$

Assuming $P_B \ll P_A$ gives the following simplification

$$\mathbf{v} \approx C_A^{-1} (M_B - M_A)$$

Finally, we also make the following assumption

$$M_B - M_A = \begin{bmatrix} 0 \\ 1 \end{bmatrix} \quad \text{or} \quad \begin{bmatrix} 1 \\ 0 \end{bmatrix}$$

corresponding to enhancing +ve or -ve changes, i.e. enhancing targets which have been added or removed, respectively.

4.2.5 CFAR filtering

The next step is to calculate the local background statistics in the change image and produce a scaled image where targets can be detected using a threshold. A CFAR (Constant False Alarm Rate) filter is used, which is defined as a convolution kernel with an outer box with non-zero values and an inner guard box with zero values. The center pixel of the kernel is the pixel under test. The background statistics of each pixel in the change image is calculated using the pixels within the region of non-zero frame.

4.2.6 Detection Analysis

The last step is to form objects and compute various attributes. First, a binary image is formed from the CFAR image by using a threshold. Binary morphological operations are used to connect pixels and remove noise pixels. The positions of the objects that remain are found by shrinking to the size of one pixel.

5 RESULTS

5.1 Introduction

This section presents the primary results found during the course of the CD study. Only ensemble results across multiple SAR image pairs are presented. Results from individual image pairs provide no statistical confidence and thus are not presented.

Six studies were conducted to determine the performance of the CD algorithm as a function of different OCs. The specific studies are summarized in Table 8. Studies one through four provide little insight into VHF SAR CD performance when viewed individually. They are meant to be examined in relation with each other. There are two OCs of interest for studies one through four: RFI and change in heading between imaging passes (Δ Heading). Both RFI and Δ Heading were categorized into one of two types. RFI was considered to be either “low” or “high” and Δ Heading was either 0° or 5° . Thus the four possible combinations of these two binary OCs are investigated across these four studies. In addition, each of these studies shows performance as a function of three different bandwidths.

Also note that each of these four studies examines the detection of only small targets at non-broadside orientations. The performance of these four studies is therefore expected to be pessimistic as compared to general VHF SAR CD performance.

Study five examines the effect of bandwidth on performance. Only two bandwidths are considered, small (25-52 MHz) and large (25-85 MHz). Targets are not grouped by size or orientation. However, only flights with headings which give a low RFI environment are used.

Study six isolates and examines the effect of incidence angle on CD performance. Specifically, incidence angles of 58° , 68° , and 72° are studied. The data are processed using only large bandwidth. However, there is no restriction on target size, orientation, or RFI environment. Thus this study provides understanding on the general performance across the Vidsel data.

Table 8. Summary of the different CD studies performed.

Study	Purpose
1	Small and Non-Broadside Targets, Low RFI, $0^\circ\Delta$ Heading
2	Small and Non-Broadside Targets, High RFI, $0^\circ\Delta$ Heading
3	Small and Non-Broadside Targets, Low RFI, $5^\circ\Delta$ Heading
4	Small and Non-Broadside Targets, High RFI, $5^\circ\Delta$ Heading
5	Target size, Low vs. High BW, Low RFI
6	Three Incidence Angles (58° , 68° , and 72°)

5.2 Measures of Performance

In this study there are only two measures of performance, P_d and FAR. Used in combination, these measures provide a ROC curve. This section describes how these measures and their confidence intervals were calculated.

5.2.1 Declaration of a Target Detection and False Alarm

As described in Section 4.2, the end result of the CD processing chain is a list of candidate target coordinates. Each candidate target must be declared to be either a true target or a false alarm. The procedure used for making this declaration is described as follows.

From the ground truth files, the GPS position of each target center is known. Each candidate target from the CD process that falls within 10 meters from a target GPS position is declared to be a true target. All candidate targets which do not comply with this condition are declared to be false alarms.

This procedure is expected to perform well within the present analysis. However, this may not be the case with a different experimental design. For example, the selected declaration procedure neglects the following effects:

- Errors or inaccuracies in the ground truth.
- Using only one radius regardless of target size.
- Not shaping or orienting the known target region.
- Using a point representation for the assumed detection.

An additional consequence of the procedure should be noted. The choice of a radius of 10 meters suggests that if the targets are placed closer than 20 meters apart then the possibility exists that one candidate target can be declared to be more than one true target. This is not an issue for this study since the minimum target spacing was roughly 50 meters.

5.2.2 P_d and FAR Calculations

P_d and FAR are defined in a straight-forward and consistent manner for all studies performed. P_d is the ratio of the number of true target detections divided by the total number of targets available. Both the numerator and denominator in this ratio are conditioned based upon the OCs of interest for the study being investigated. For example, in studies one through four, only small targets are of interest. Thus only small targets are counted as being true target detections in the numerator. Also, only small targets are counted when determining the total number of targets available. Note also that this value can, and often is further conditioned based upon the other OCs of interest, i.e. only small targets with non-broadside orientation.

FAR is defined as the ratio of the total number of false detections normalized by the total number of square kilometers used. No conditioning of either the numerator or denominator is considered. Furthermore, no segmenting of the images is performed. All pixels in the image are processed and a false alarm can come from any location in the image regardless if that pixel represents forest, populated area, marsh, or lake. The decision not to segment was made to help increase the total number of square kilometers available and thus improve statistical confidence.

The total number of true targets detected is determined by summing the true targets detected from each image pair used for a given study. Likewise, the total number of targets available is

also determined by summing the total number of applicable targets across each image pair used. The number of false alarms is the total number of false detections found across all images used. The total number of square kilometers is determined by summing the total number of pixels available across all change images used and converting to square kilometers.

This manner of calculation is equivalent (minus any potential edge effects) to calculating P_d and FAR from a mosaic of all change images used for a given study. Since each image in this mosaic has the same aim point, each change image is a representation of the same section of the Vidsel test range. Thus the results obtained for this study are not expected to be representative of the results found across a larger region whose total number of square kilometers is equal to the square kilometers of the mosaic.

5.2.3 Confidence Interval Calculations

The 95% confidence intervals on both P_d and FAR were also calculated for all results generated during the course of this study. The most commonly used confidence interval estimators have limited accuracy for the conditions found in this study. Specifically, it is known that for discrete distributions, small sample sizes, and for probability values close to either zero or one, commonly used confidence interval estimators have limited accuracy. Thus a more accurate measure of confidence intervals were used based upon the work found in [12] and [13].

These techniques use more appropriate parametric models for both proportion and rate estimates than the normal Gaussian assumption. P_d is an example of a proportion estimate while FAR is an example of a rate estimate. In the case of a proportion estimate a Binomial distribution is the model used for estimating confidence intervals whereas a Poisson distribution is the model used in estimating rate confidence intervals.

While the parametric models used to generate the confidence intervals in this study are accurate, it should be noted that the intervals they generate represent only quantity-limitations. No inference can be made by these intervals on how this CD processing chain would perform on a different data set. In order to make such inferences, certain assumptions regarding the data set would have to be true. These assumptions, including the data set being a sample population, random, and independent, are strictly speaking not true. As a consequence, the expected confidence intervals which could be used to infer performance are larger than those seen in this study.

5.3 ROC Curves

5.3.1 Studies 1-4: RFI Environment and 5° Change in Heading

As mentioned in Section 5.1, studies one through four provide little insight into the performance of the CD system when viewed independently. However, when viewed jointly, studies one through four provide information on how the system performs with regards to changes in the RFI environment and to a 5° change in heading between the two passes used to form a change image. In addition, the impact of bandwidth on system performance is also seen in these studies, i.e. for low (25-52 MHz), medium (25-68 MHz), and high (25-85 MHz) bandwidth. For more explanation on the meaning of low vs. high RFI environment, see Section 3.5.4.

To avoid monotony, the results for these four studies will only be presented in unison. Figure 17 shows the ROC curves for each of these four studies. Confidence intervals (95%) for both P_d and FAR are given.

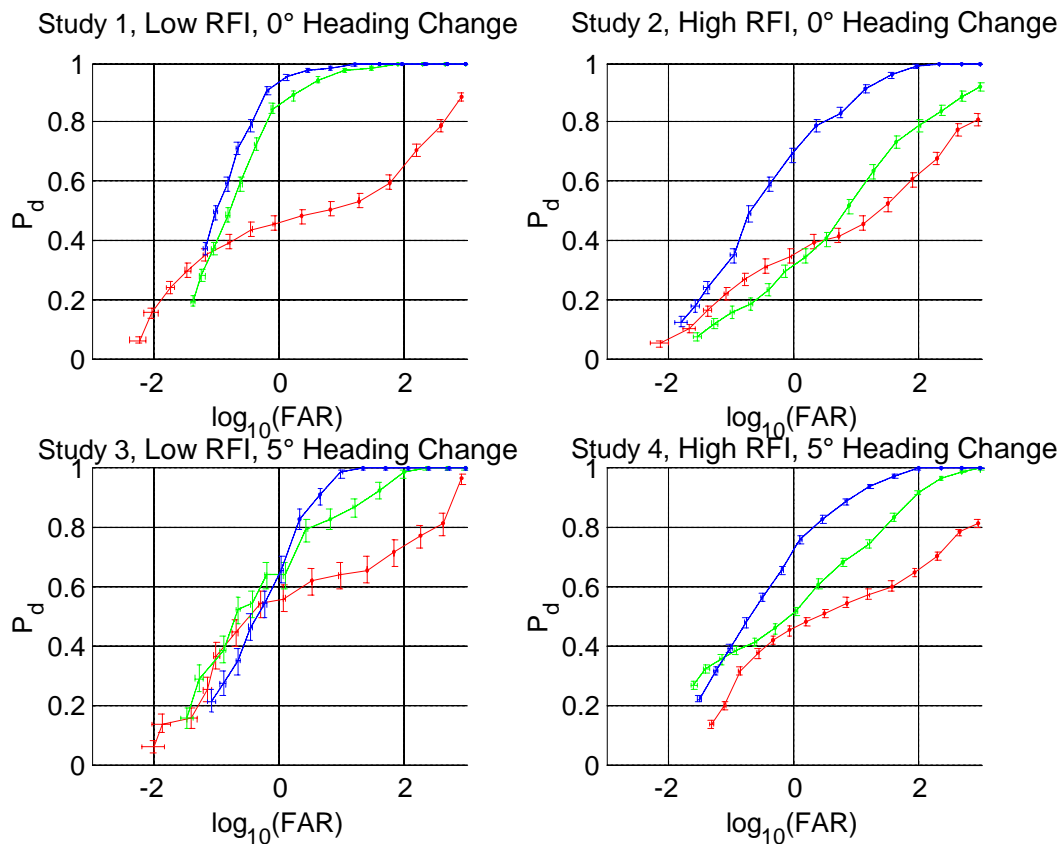


Figure 17. ROC curves for studies 1-4. Each of the four graphs shows the results for three different bandwidths. The legend for each plot is: low (r-), medium (g.), and high (b-) bandwidth. Studies 1-4 used 14, 9, 5, and 26 image pairs, respectively.

Some comments regarding these four studies are as follows:

- In all four studies, as bandwidth decreased, performance worsened.
- In all four studies, both target size and orientation were chosen to provide a scenario which is more difficult than on average.
- In study number one, there is sharp decrease in performance from medium to low bandwidth.
- In study two, there is a noticeable decrease in performance going from the high to the medium bandwidth case. This result is expected when the percentage of spectrum contaminated by RFI is considered - see Figure 20.
- There were only 5 image pairs suitable for study three (as opposed to 14, 9, and 26 for studies 1, 2 and 4, respectively). Thus the ROC curve for study three is not smooth and the confidence intervals are significantly larger.

The confidence intervals provided in these charts are expected to be optimistically tight when inferring performance on data collected at regions other than RNF Vidsel. Also, since the same segment of ground was used for each image pair, it can be argued that the confidence

intervals presented are even optimistic when compared to data collected at multiple regions at RFN Vidsel. Thus an alternative, pessimistic approach to generating confidence intervals was also used. This was done by averaging across the confidence intervals generated by each individual change image. Figure 18 shows the same results as in Figure 17 but using the pessimistic confidence interval technique. It is expected that the true confidence intervals across the RFN Vidsel area of Sweden lie somewhere between the two extremes depicted by these two figures. Also, while both sets of confidence intervals were generated for all results presented in this report, only the optimistic intervals will be presented to help avoid monotony and because the method used to generate these intervals are more recognized.

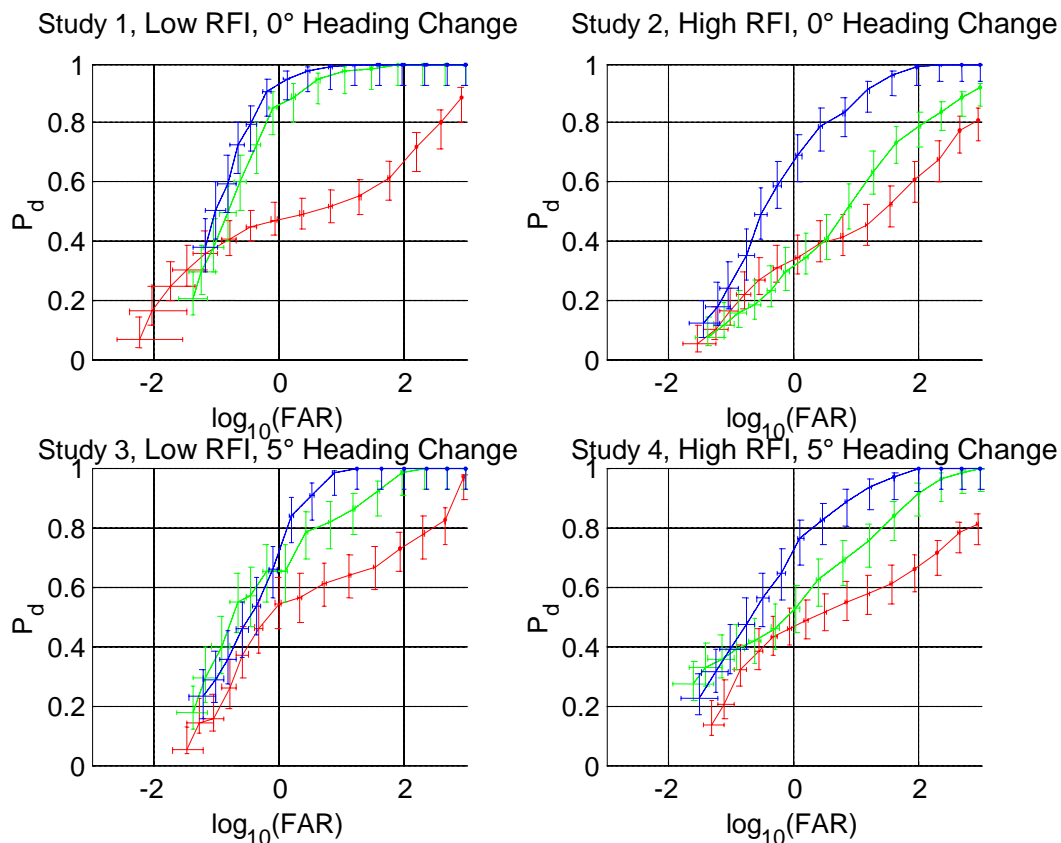


Figure 18. ROC curves for studies 1-4 using pessimistic confidence intervals. Each of the four graphs shows the results for three different bandwidths. The legend for each plot is: low (r-), medium (g.), and high (b-) bandwidth.

While Figure 17 and Figure 18 provide an adequate means for viewing the results of each study independently and comparing the effects of bandwidth, it is not well suited for viewing how changes in both RFI environment and changes in flight heading between passes affect performance. Thus the same information presented has been rearranged in Figure 19 so that performance as a function of these OCs can be better seen.

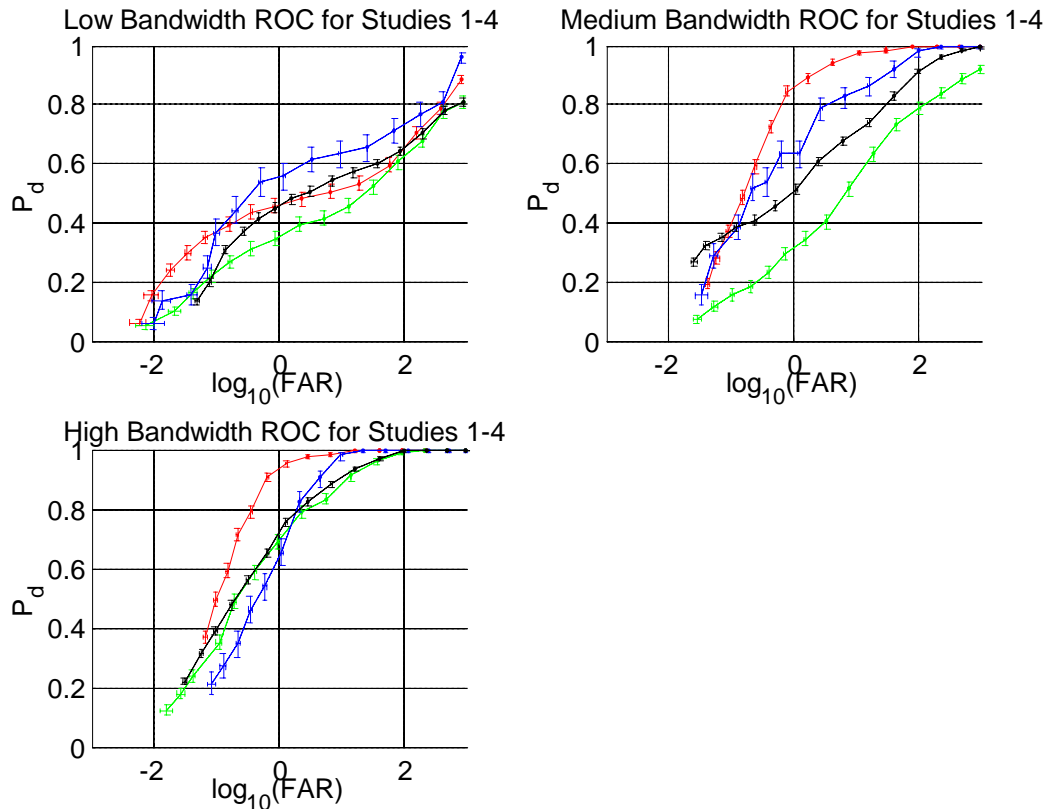


Figure 19. Comparison of studies 1-4, grouped by bandwidth. The legend for each of the three graphs is the same: Study 1 (r-), Study 2 (g-), Study 3 (b-), and Study 4 (black--).

From the results seen in Figure 19 the following observations can be made:

- In all four studies, the low bandwidth ROC curve has an unexpected shape. The reason for this unexpected shape will be explained later.
- For the low bandwidth case, the performance across all four studies is sufficiently poor such that no other conclusions can be drawn.
- The impact on performance by RFI environment appears to be more pronounced than the impact by a 5° change in heading, at least for medium bandwidth case. This is expected since the anticipated RFI takes up a larger percentage of the medium bandwidth case, as seen in Figure 20.
- For the medium and large bandwidth cases with low RFI (studies 1 and 3), there is a noticeable, yet not excessive decrease in performance going from a 0° to 5° change in heading.
- For the large bandwidth cases with high RFI (studies 2 and 4), there is a no noticeable change in performance going from a 0° to 5° change in heading.
- For the medium bandwidth cases with high RFI (studies 2 and 4), there is a noticeable, and unexpected increase in performance going from a 0° to 5° change in heading. There is presently no good explanation for this behavior besides being a pure statistical effect.

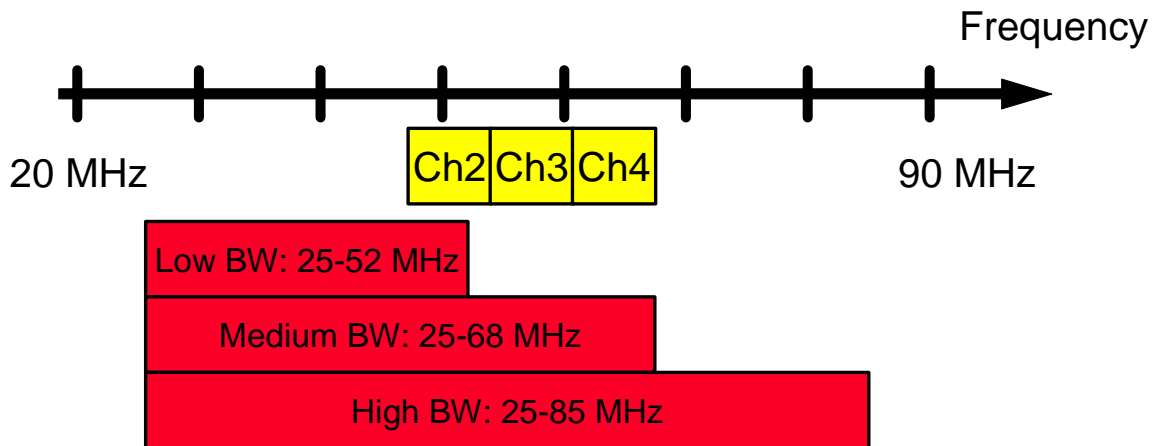


Figure 20. Illustration of the impact of RFI from low-VHF TV on the three bandwidths used.

5.3.2 Analysis of ROC Curve Shape for Low Bandwidth and Small Targets

As seen in Figure 19, there is a consistent, unexpected shape for all ROC curves when a bandwidth of only 25-52 MHz is used in conjunction with small targets at non-broadside orientations. This shape will also be seen in other studies when low bandwidth, small target cases are considered. Thus it is beneficial to investigate the cause for this unexpected result.

A better understanding of this shape is seen by examining the P_d vs. CFAR threshold graph for the low bandwidth case of study one. Figure 21 shows that the detection performance of each image pair suited for this study can be classified roughly into one of two classes; those with reasonable performance and those with poor performance. The resulting ensemble detection performance curve is impacted greatly by those image pairs with poor performance, especially at a low CFAR threshold. Thus the resulting ensemble curve shows both a quick decay in performance early as well as poorer than expected performance across all threshold levels. This shape is maintained when the P_d numbers are translated onto a ROC curve.

Again, this bimodality of the detection performance of individual image pairs is only seen with the combination of low bandwidth and small targets. The bimodality of the image pair P_d vs. CFAR threshold curves is not seen for medium or large targets or medium or large bandwidths.

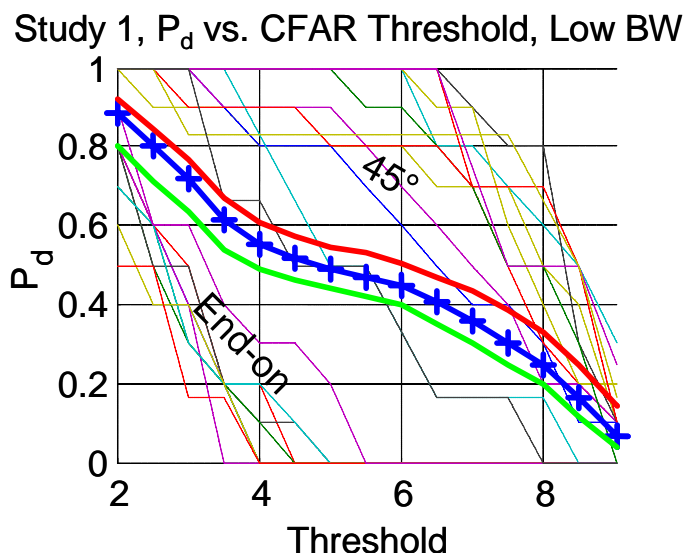


Figure 21. P_d curves for each image pair used in the low bandwidth case of study number 1. The bold, solid lines represent the average ROC curve from these 14 individual curves and the corresponding confidence intervals.

To understand the source of the bimodality of low bandwidth P_d , each of the change images used to generate the ensemble ROC curve for the low bandwidth case of study one were examined. It was determined that the image pairs which gave reasonable performance occurred when the imaging geometry was such that the targets were imaged at an orientation of 45° . Likewise, the image pairs which gave poor performance occurred when the imaging geometry was such that the targets were imaged at an orientation of 0° (end-on).

Figure 22 through Figure 25 provide further evidence for the cause of bimodality. In Figure 22 and Figure 24 we see the flight geometries used to collect two images used in study number one. The first geometry results in all targets having an end-on orientation while the second results in a 45° orientation. Figure 23 and Figure 25 show the SAR chips of the target array for each of these geometries at each of the three bandwidths investigated. Note how for the low bandwidth, end-on case in Figure 23, there is no noticeable energy in the surveillance image. Thus there is little chance there will be sufficient energy to detect a change, hence it is not surprising that in these cases the P_d performance is quite poor. However, there is sufficient energy to detect small targets using a low bandwidth when they have an orientation of 45° , as seen in Figure 25. Thus there is evidence to support the conclusion that the reason for the unexpected shape associated with P_d performance for small targets imaged at low bandwidth occurs due to the lack of energy of these targets imaged at end-on geometry.

It might seem surprising that the small targets oriented in 45° from the flight track gave a higher energy than the end-on targets. The opposite behavior may have been expected since the end-on geometry provides a more effective dihedral formed between the target side and the ground surface. This is indeed true for zero-Doppler frequency, but the 45° target will also form an effective dihedral for other Doppler frequencies because of the large aperture angle used in CARABAS-II. The effect will be further studied by RCS modeling.



Figure 22. Imaging geometry for one pass used in study number 1. The arrow indicates the flight heading. The geometry resulted in all 10 small targets (enclosed by circles) to have an end-on orientation.

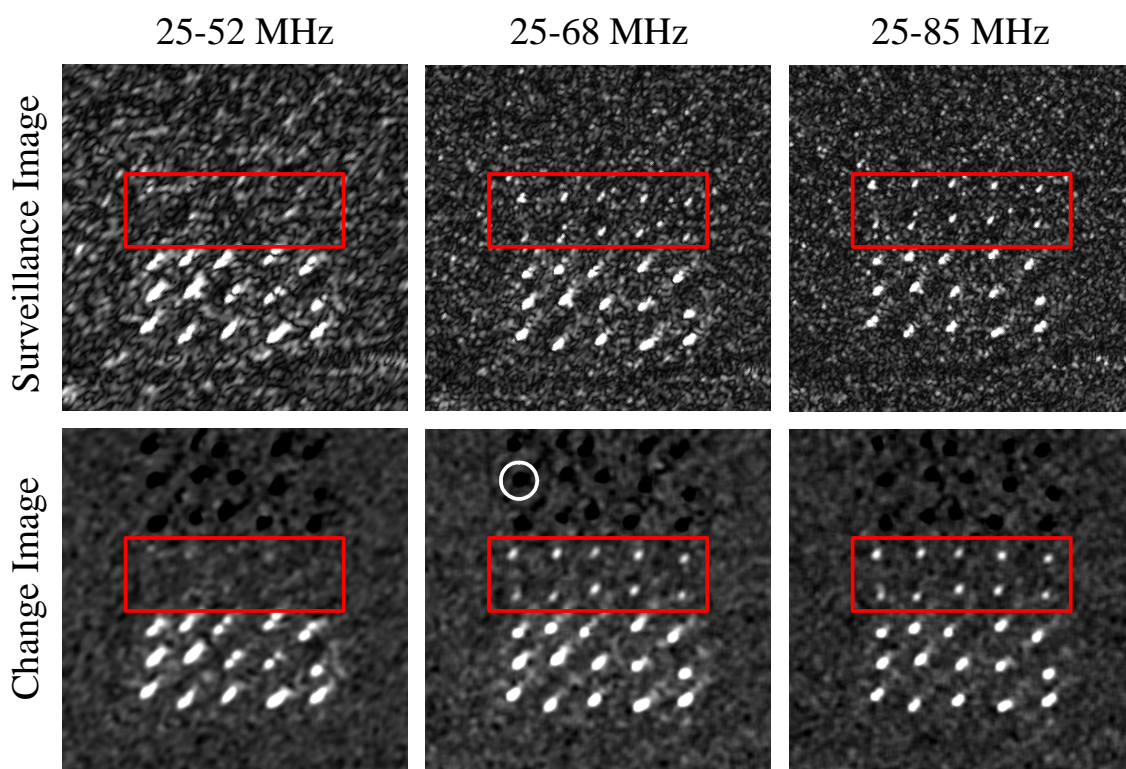


Figure 23. The surveillance and change images at all three bandwidths from imaging geometry found in Figure 22. The boxes denote the location of the small targets. The white circle denotes the location of a negative change which is of no importance for this discussion.

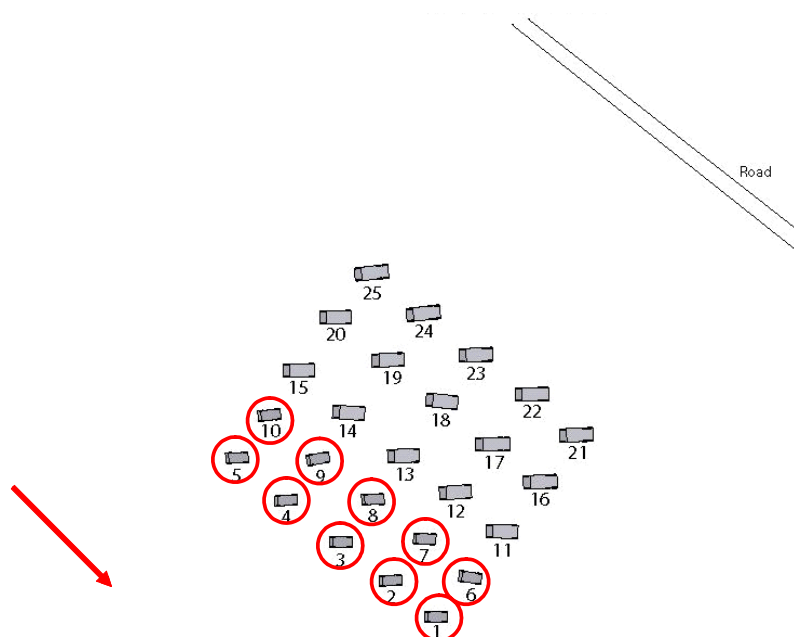


Figure 24. Imaging geometry for one pass used in study number 1. The arrow indicates the flight heading. The geometry resulted in all 10 small targets (enclosed by the circles) to have a 45° orientation.

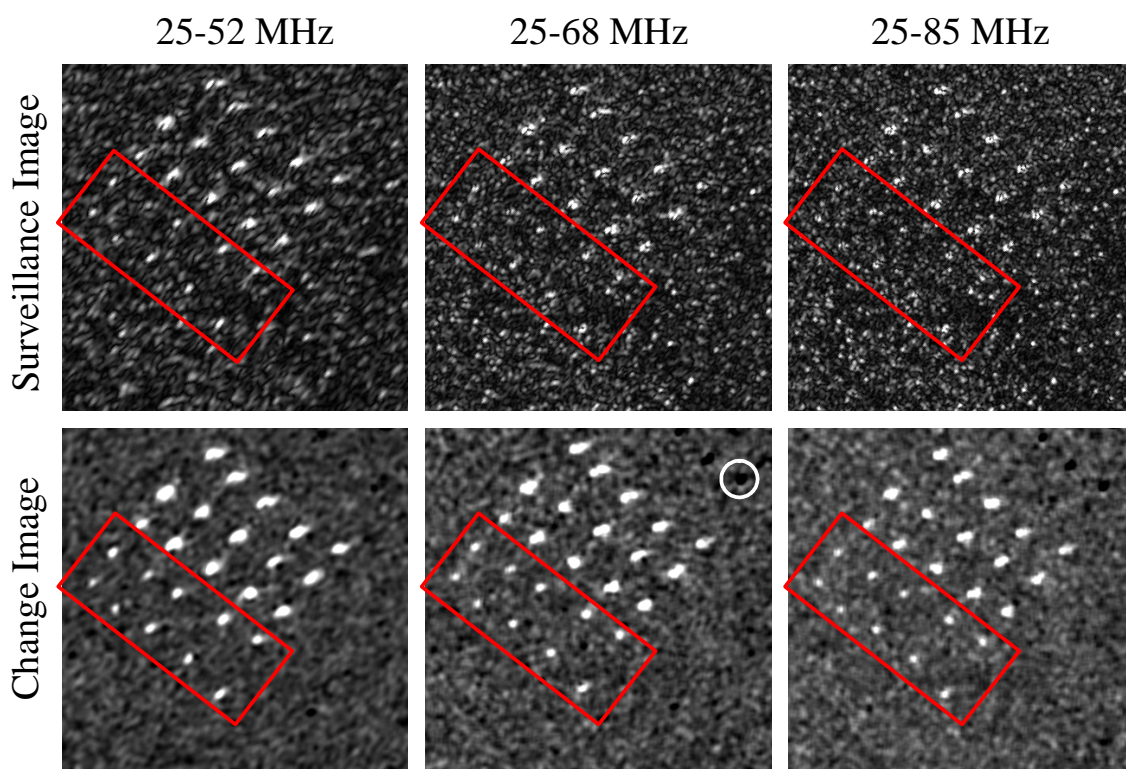


Figure 25. The surveillance and change images at all three bandwidths from imaging geometry found in Figure 24. The boxes denote the location of the small targets. The white circle denotes the location of a negative change which is of no importance for this discussion.

5.3.3 Study 5: Target Size and Bandwidth

The purpose of study number five is to investigate performance as a function of both bandwidth and target size. Unlike studies one through four, study five does not consider performance as a function of target aspect. Furthermore, only flight paths resulting in a low RFI are considered. Thus it is expected that this study will result in optimistic results when compared to overall system performance.

Figure 26 shows the ROC curves associated with this study. The following observations can be made from these results:

- Target size has a noticeable impact on performance at lower bandwidths but little impact on performance at higher bandwidths.
- There is a significant but not excessive decrease in performance going from the high to the low bandwidth case for the large target class.

Note again, the odd shape of the low bandwidth, small target ROC curve. As discussed in the previous section, the reason for this shape is the lack of energy in the return for small targets at low frequencies with an end-on orientation.

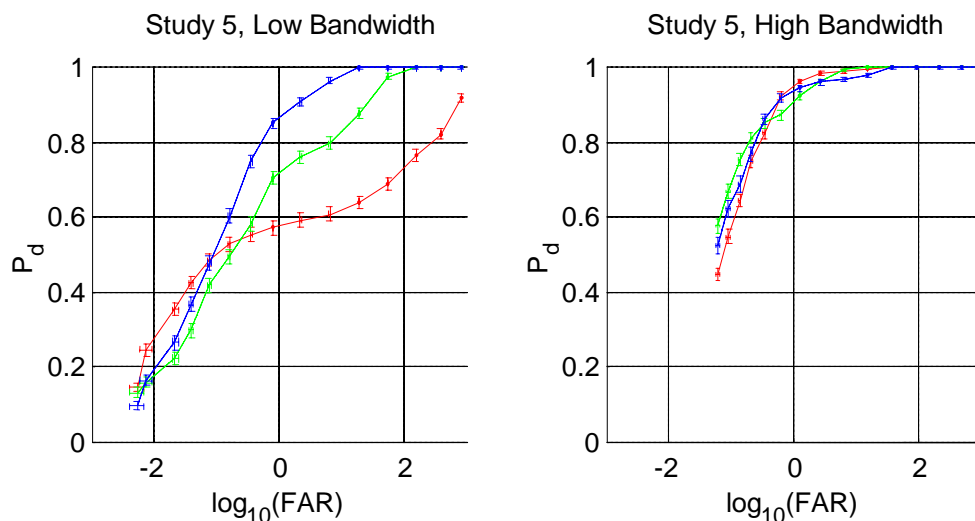


Figure 26. ROC curves for study number 5: Left is the low bandwidth case (25-52 MHz), right is the high bandwidth (25-85 MHz) case. On both graphs, the legend is: small (r-), medium (g.), and large (b-.) targets. In both the low and high BW cases, 23 image pairs were used to perform this study.

5.3.4 Study 6: Incidence Angle

The purpose of study six is to investigate CD performance as a function of incidence angle. For this, all target aspects were considered and all RFI environments were included. Originally, target size was not a parameter of interest. The results are presented in Figure 27.

There were no unexpected results found during the course of this study. It is observed that under all bandwidths, performance decreases as the incidence angle increases.

Figure 28 shows the same results as seen in Figure 27 but now the data is grouped by bandwidth instead of incidence angle.

Furthermore, it is noted that there is a significantly larger change in performance across the different bandwidths at 58° than there is at either 68° or 72° .

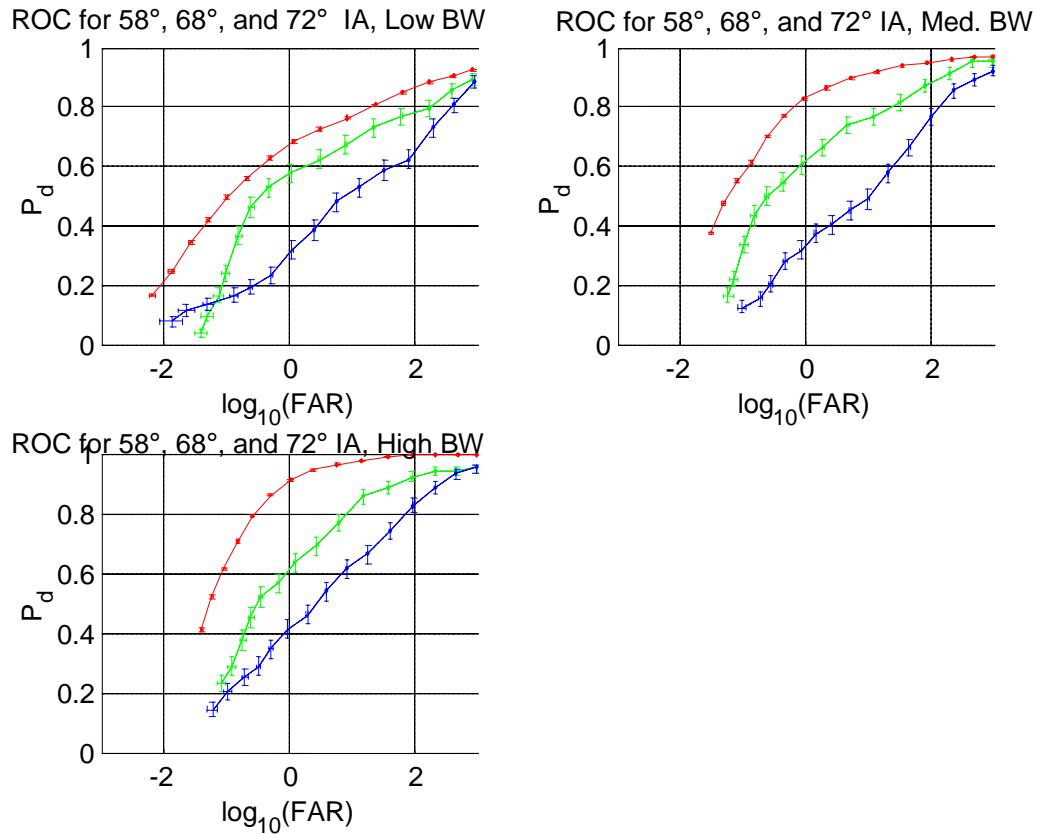


Figure 27. ROC curves for study six showing performance as a function of incidence angle for various bandwidths. On all graphs, the legend is: 58° (r-), 68° (g.), and 72° (b-). The 58° , 68° , and 72° incidence angle results were generated using 68, 4, and 4 image pairs, respectively.

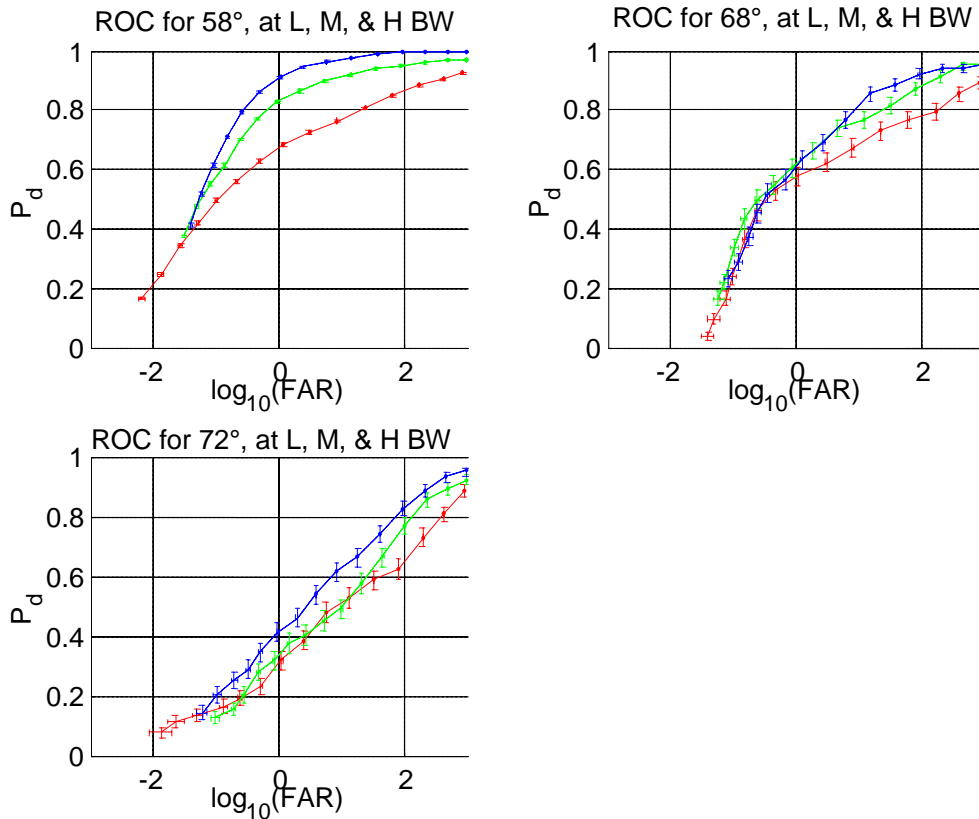


Figure 28. ROC curves for study six showing performance as a function of bandwidth for various incidence angles. On all graphs, the legend is: low (r-), medium (g.), and high (b-) bandwidth.

This study was extended to investigate the effect of target size on performance as a function of incidence angle; Figure 29 and Figure 30 show these results. Figure 29 shows the ROC curves for only small targets, whereas Figure 30 shows the ROC curves for medium and large targets combined. The reason for combining medium and large targets is to increase the number of targets and thus reduce the confidence intervals. Also, the difference in target size between medium and large target classes is sufficiently small that no noticeable performance difference is expected across these two target classes.

A few more conclusions can be drawn from this further analysis. First, it does appear that performance is more sensitive to incidence angle for small targets. For the low bandwidth case, only the medium and large targets give a reasonable performance at the two lowest incidence angles 58° and 68° . The high bandwidth case, on the other hand, gives reasonable performance across all incidence angles for this combined target class.

Secondly, even for the high bandwidth case there is a significant performance drop as the incidence angle increases for small targets. The increase in FAR is about three orders of magnitude as the incidence angle increases from 58° to 72° for a fixed P_d .

Another comment valid for all results in this study is that there were only 4 suitable image pairs for the 68° and 72° case while there were 68 pairs available for the 58° case. Thus there is a large difference in the confidence intervals in these results. This can be seen in the difference in smoothness across the plots for the different incidence angles.

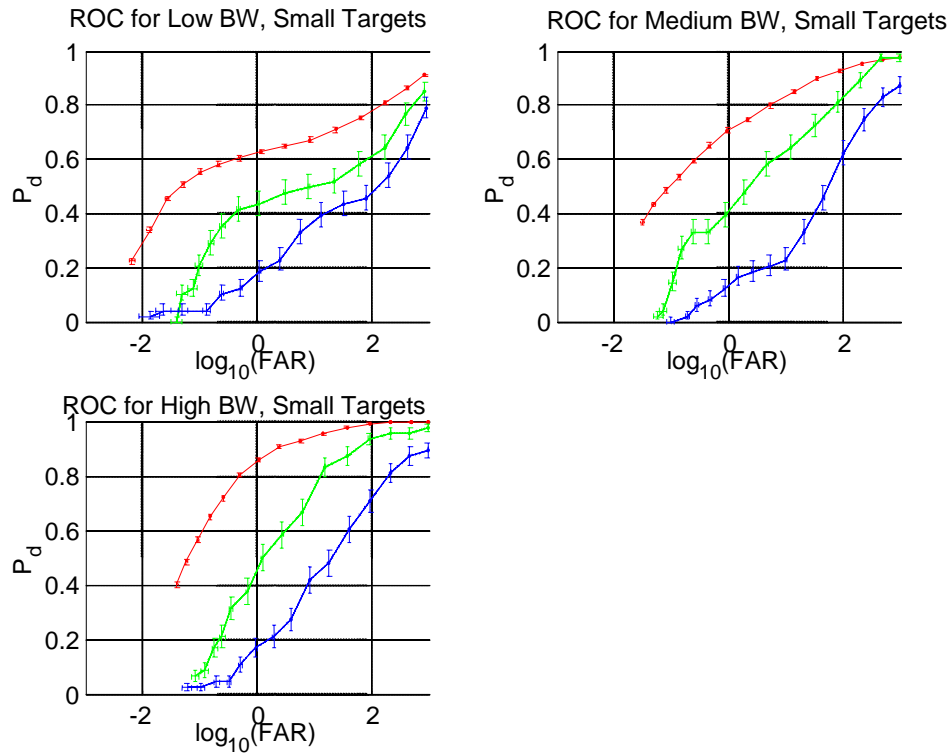


Figure 29. ROC curve for study 6 with only small targets. Legend: 58° (r-), 68° (g-), and 72° (b-).

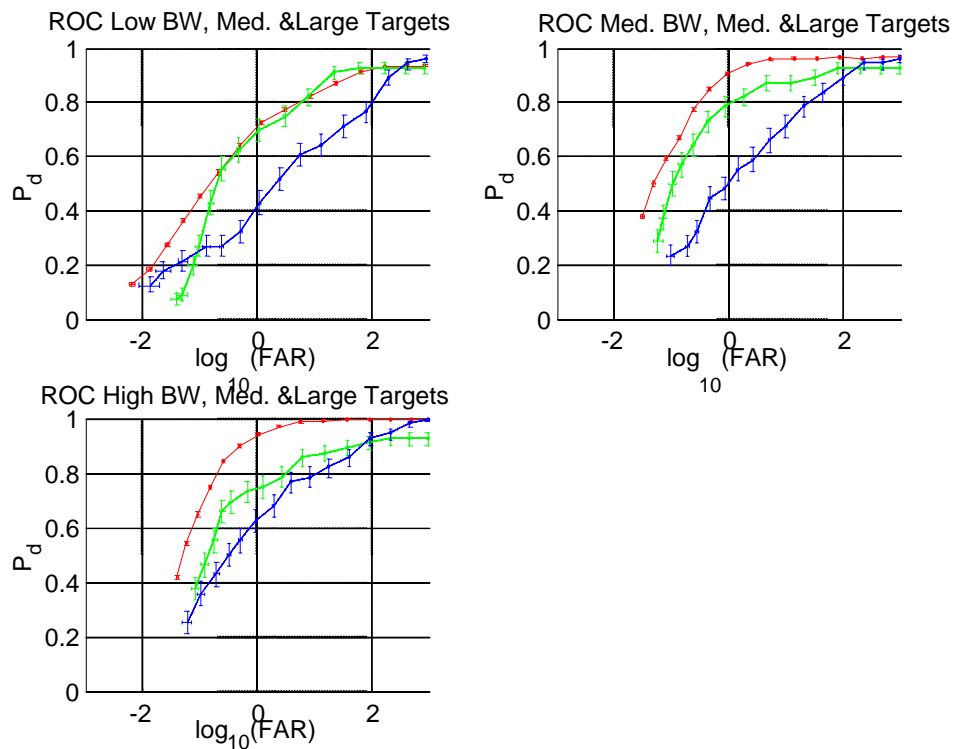


Figure 30. ROC curve for study 6 with medium and large targets. Legend: 58° (r-), 68° (g-), and 72° (b-).

6 CONCLUSIONS

Sixteen successful CARABAS-II missions were flown at the RFN Vidsel test range between 30 May and 12 June, 2002. SAR images from all 150 flight passes have been processed.

A total of 64 images from eleven flight missions were used to perform the change detection analysis presented in this report.

The data collection was planned and executed such that sufficient data would exist to test performance as a function of various operating conditions. The operating conditions of importance in this study were target orientation, target size, change in heading between the two images used to form a change image, radio-frequency interference, bandwidth, and incidence angle.

Six different change detection studies were performed to measure performance across these operating conditions. The performance metric used in all studies was a ROC curve ("Receiver-Operator-Characteristic"), i.e. probability of target detection vs. false-alarm rate.

The results obtained by these studies can be categorized into expected and unexpected results. The expected results were:

- Performance improves as bandwidth increases.
- Performance increases as target size increases.
- Performance decays slowly for changes in flight heading between imaging passes.
- There was a noticeable decrease in performance when the RFI environment increased.
- There was substantial performance loss at high incidence angles.

The unexpected results found were:

- The combination of small bandwidth plus small targets with end-on orientation resulted in no target detection at all.

The change detection processing scheme used throughout this study was intentionally kept uncomplicated and consistent. The decision to keep the scheme uncomplicated was made to ensure robust performance across all of the operating conditions being investigated. The processing scheme was kept consistent to ensure that comparisons between the different studies performed would produce meaningful conclusions. Thus while the change detection performance obtained throughout this study is consistent, it does not represent the state of the art in change detection.

REFERENCES

- [1] H. Hellsten, L.M.H. Ulander, A. Gustavsson, and B. Larsson, "Development of VHF CARABAS-II SAR," in Proc. Radar Sensor Technology, held in Orlando, FL, 8-9 April 1996, SPIE vol. 2747, pp. 48-60, 1996.
- [2] J.G. Roos, "Unmasking the Enemy," Armed Forces Journal International, p. 51, April 1998.
- [3] L.M.H. Ulander, P.-O. Frö Lind, A. Gustavsson, H. Hellsten, T. Jonsson, B. Larsson, and G. Stenström, "Performance of the CARABAS-II VHF-band synthetic aperture radar," in Proc. IGARSS'01, held in Sydney, Australia, 9-13 July 2001, pp. 129-131, 2001.
- [4] R.T.K. Jaldehag, J.M. Johansson, P. Eló segui, J.L. Davis, A.E. Niell, B.O. Rö nnäng, and I.I. Shapiro, "Geodesy using the Swedish permanent GPS network: Effects of signal scattering on estimates of relative site positions," J. Geophys. Res., vol. 101, pp. 17.814-17.860, 1996.
- [5] L.M.H. Ulander, "Performance of Stepped-Frequency Waveform for Ultra-Wideband VHF SAR," in Proc. EUSAR '98, held in Friedrichshafen, Germany, 25-27 May 1998, pp. 323-326, 1998.
- [6] L.M.H. Ulander, H. Hellsten, and G. Stenström, "Synthetic-Aperture Radar Processing Using Fast Factorised Back-Projection," IEEE Transactions on Aerospace and Electronics Systems, vol. 39, no. 32, pp. 760-776, 2003.
- [7] L.M.H. Ulander, P.-O. Frö Lind, and T. Martin, "Processing and Calibration of Ultra-Wideband SAR Data from CARABAS-II," in Proc. CEOS SAR Workshop, held in Toulouse, France, 26-29 October 1999, ESA SP-450, pp. 273-278, 2000.
- [8] M. Lundberg, B. Flood, P. Follo, P.-O. Frö Lind, A. Gustavsson, T. Jonsson, B. Larsson, G. Stenström, and L.M.H. Ulander, "CARABAS-II Campaign Vidsel 2002. Ground Report," FOI-R--0963--SE, 2003.
- [9] L.M.H. Ulander, B. Flood, P. Follo, P.-O. Frö Lind, A. Gustavsson, T. Jonsson, B. Larsson, M. Lundberg, and G. Stenström, "CARABAS-II Campaign Vidsel 2002. Flight Report," FOI-R--1002--SE, 2003.
- [10] F. Walter, "CARABAS-II Campaign Vidsel 2002. Forest Report," FOI-R--0962--SE, 2003.
- [11] L.M.H. Ulander, P.-O. Frö Lind, A. Gustavsson, H. Hellsten and B. Larsson, "Detection of Concealed Ground Targets in CARABAS SAR Images using Change Detection," Proc. Algorithms for Synthetic Aperture Radar Imagery VI, held in Orlando, FL, 5-9 April, 1999, SPIE vol. 3721, pp. 243-252, 1999.
- [12] T. Ross, "Confidence Intervals for ATR Performance Metrics," Proc. Algorithms for Synthetic Aperture Radar Imagery VIII, held in Orlando, FL, 16-19 April, 2001, SPIE vol. 4382, pp. 318-329, 2001.
- [13] T. Ross, "Accurate confidence Intervals for Binomial Proportion and Poisson Rate Estimation," Computers in Biology and Medicine, in press.

APPENDIX A SAR IMAGE QUALITY NUMBERS

The following table contains image quality numbers for each image used in the present report.

The naming convention used is as follows:

v02_x_y_z.a.Fbp.RFcorr.Cmpx

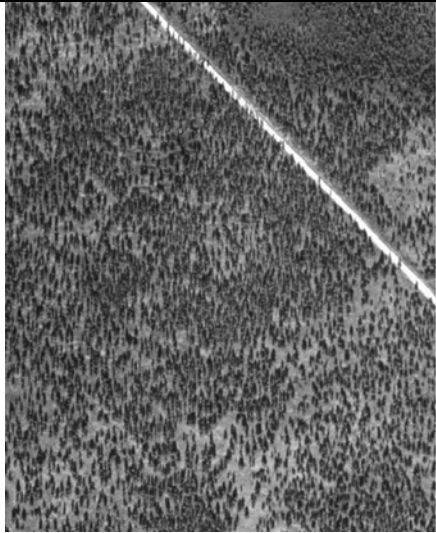
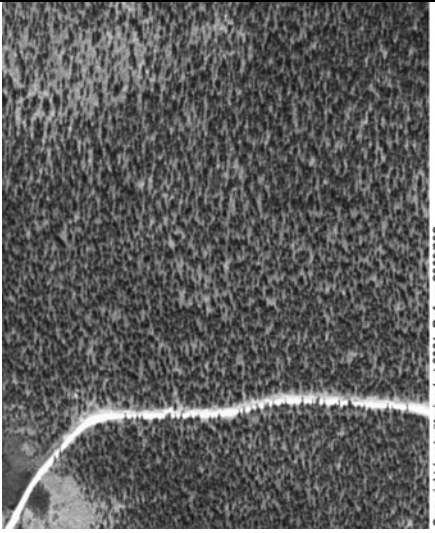
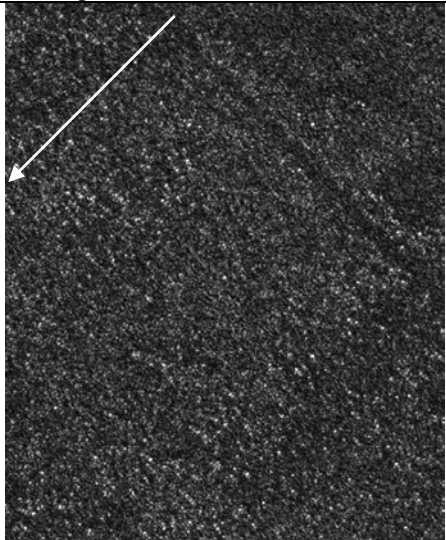
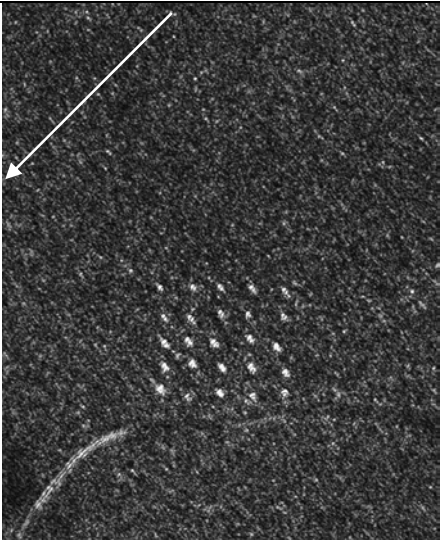
- v02 stands for Vidsel 2002
- x is flight mission number
- y is flight pass number
- z is image sequence number
- a is antenna channel (a = closest to illumination side, b = away from illumination side)
- Fbp means that factorised backprojection algorithm has been used for SAR processing
- RFcorr means data are radiometrically calibrated in range and radial frequency
- Cmpx means pixel data are in complex format with 32 + 32 bit floating point representation of the real and imaginary parts

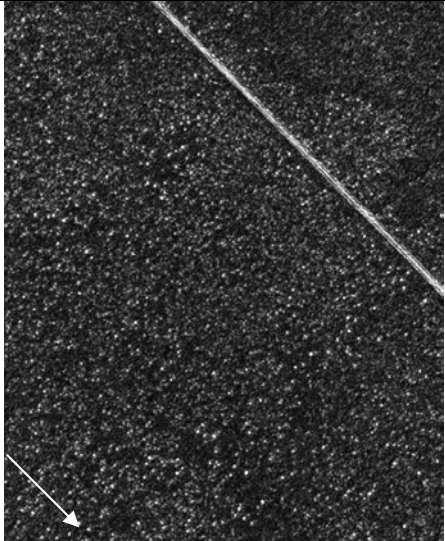
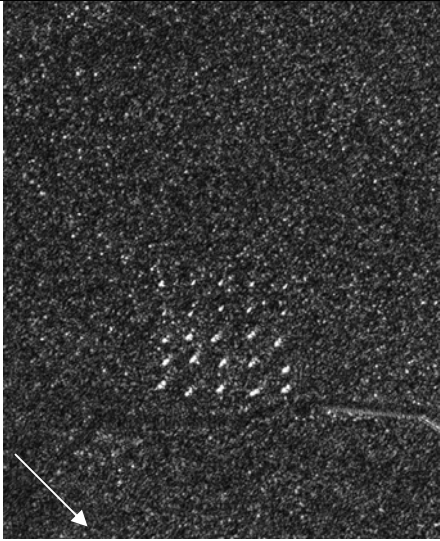
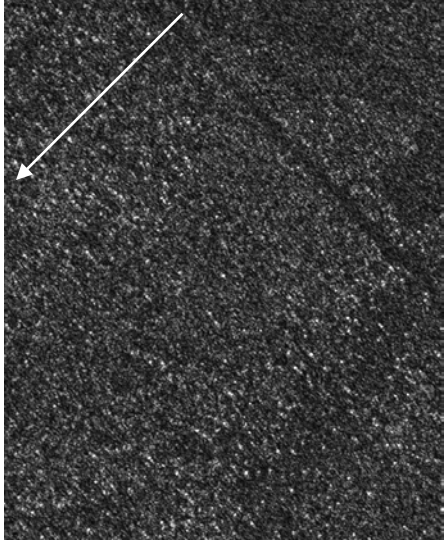
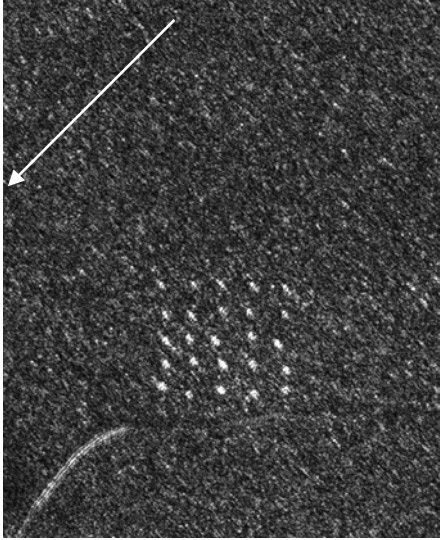
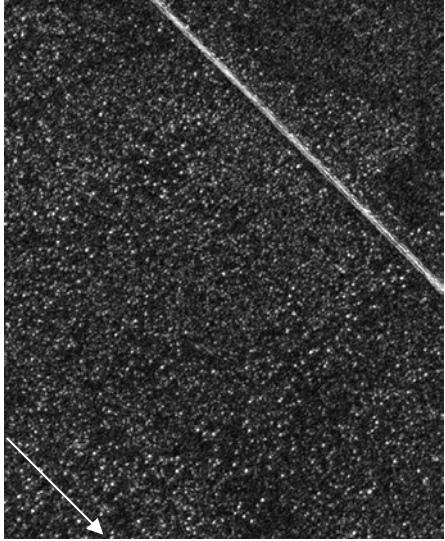

Image File Name	Noise Power (dB)	Trihedral 3dB Az. Width (m)	Trihedral 3dB Range Width (m)	Trihedral Contour Area (m ²)	Heading (°)
v02_2_1_1.a.Fbp.RFcorr.Cmpx	-17.8	3.0	2.5	6.1	225
v02_2_2_1.a.Fbp.RFcorr.Cmpx	-20.2	2.8	2.7	5.5	135
v02_2_3_1.a.Fbp.RFcorr.Cmpx	-17.1	3.1	2.5	6.4	225
v02_2_4_1.a.Fbp.RFcorr.Cmpx	-20.1	2.8	2.8	6.5	135
v02_2_5_1.a.Fbp.RFcorr.Cmpx	-17.9	3.0	2.5	6.4	230
v02_2_6_1.a.Fbp.RFcorr.Cmpx	-19.5	3.0	2.6	6.2	230
v02_3_1_2.a.Fbp.RFcorr.Cmpx	-18.0	3.2	2.5	6.8	225
v02_3_2_1.a.Fbp.RFcorr.Cmpx	-19.6	3.0	2.7	6.3	135
v02_3_3_1.a.Fbp.RFcorr.Cmpx	-18.2	2.9	2.6	6.2	225
v02_3_4_1.a.Fbp.RFcorr.Cmpx	-20.1	2.9	2.7	6.5	135
v02_3_5_2.a.Fbp.RFcorr.Cmpx	-18.2	2.8	2.6	6.1	230
v02_3_6_1.a.Fbp.RFcorr.Cmpx	-18.9	3.0	2.6	3.1	230
v02_4_1_1.a.Fbp.RFcorr.Cmpx	-18.0	3.2	2.6	6.8	225
v02_4_2_1.a.Fbp.RFcorr.Cmpx	-19.8	2.9	2.7	6.4	135
v02_4_3_1.a.Fbp.RFcorr.Cmpx	-17.8	3.1	2.6	6.6	225
v02_4_4_1.a.Fbp.RFcorr.Cmpx	-20.5	2.9	2.7	6.2	135
v02_4_5_1.a.Fbp.RFcorr.Cmpx	-18.3	3.0	2.6	6.1	230
v02_4_6_1.a.Fbp.RFcorr.Cmpx	-18.4	3.0	2.5	6.6	230
v02_5_1_1.a.Fbp.RFcorr.Cmpx	-17.8	3.1	2.5	6.0	225
v02_5_2_1.a.Fbp.RFcorr.Cmpx	-20.3	3.0	2.7	6.4	135
v02_5_3_1.a.Fbp.RFcorr.Cmpx	-17.0	3.0	2.6	5.8	225
v02_5_4_1.a.Fbp.RFcorr.Cmpx	-20.2	2.8	2.7	5.9	135
v02_5_5_1.a.Fbp.RFcorr.Cmpx	-18.6	3.1	2.5	6.4	230
v02_5_6_1.a.Fbp.RFcorr.Cmpx	-18.6	3.2	2.6	5.6	230
v02_7_1_9.a.Fbp.RFcorr.Cmpx	-18.8	3.3	2.6	6.9	225
v02_7_2_3.a.Fbp.RFcorr.Cmpx	-19.0	2.8	2.6	4.6	135
v02_7_9_2.a.Fbp.RFcorr.Cmpx	-17.6	3.1	2.7	6.8	225
v02_7_10_3.a.Fbp.RFcorr.Cmpx	-20.7	3.1	2.7	6.6	135

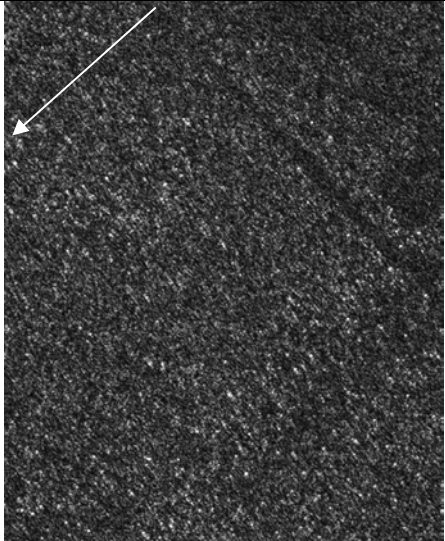
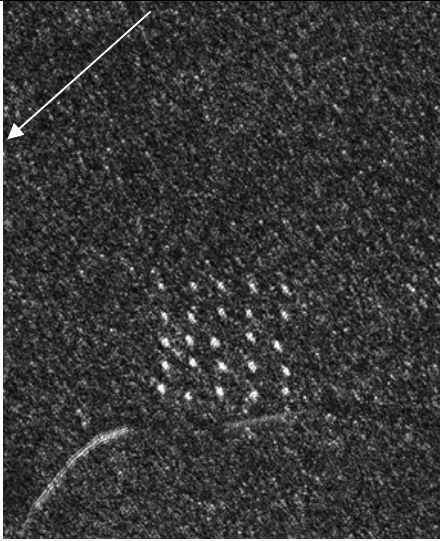
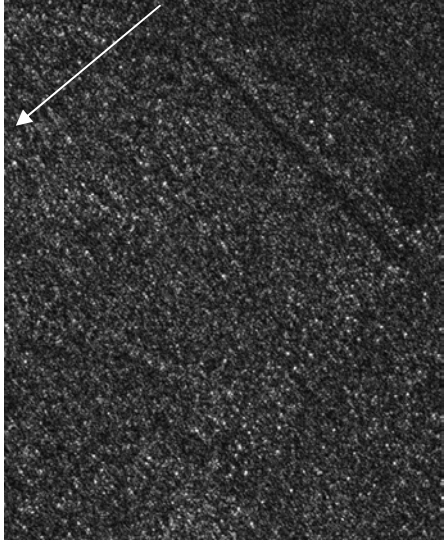
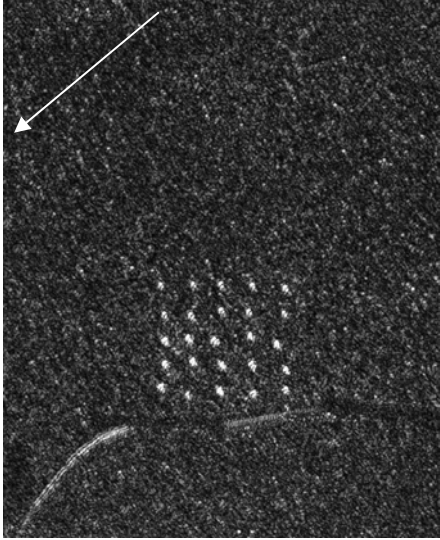
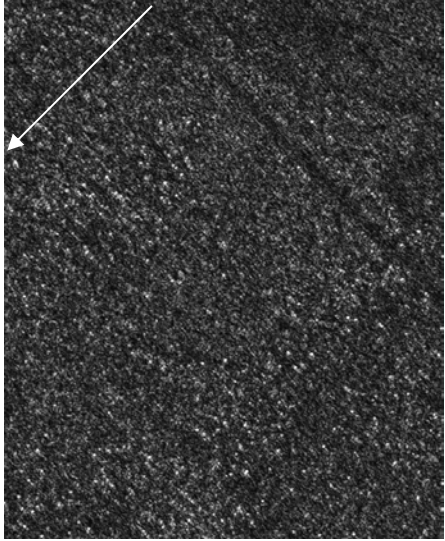
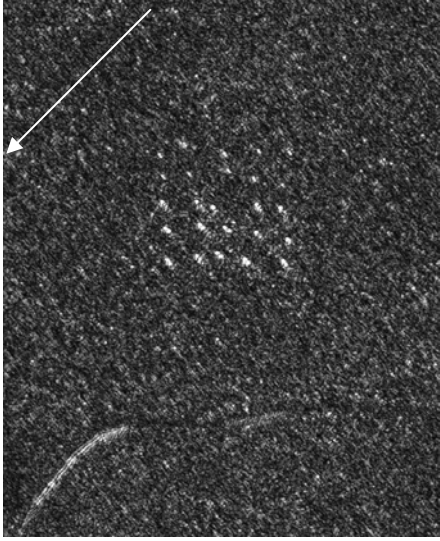
v02_8_1_2.a.Fbp.RFcorr.Cmpx	-19.2	3.2	2.7	7.2	45
v02_8_2_1.a.Fbp.RFcorr.Cmpx	-21.2	2.9	2.8	6.6	315
v02_8_3_1.a.Fbp.RFcorr.Cmpx	-17.3	3.1	3.0	7.0	225
v02_8_4_1.a.Fbp.RFcorr.Cmpx	-20.4	3.0	2.9	6.8	135
v02_8_5_1.a.Fbp.RFcorr.Cmpx	-19.6	3.0	2.8	7.2	45
v02_8_6_1.a.Fbp.RFcorr.Cmpx	-22.6	3.1	2.8	7.2	315
v02_9_1_13.a.Fbp.RFcorr.Cmpx	-17.8	3.2	2.6	5.6	225
v02_9_2_3.a.Fbp.RFcorr.Cmpx	-18.1	3.2	2.6	6.5	227
v02_9_3_6.a.Fbp.RFcorr.Cmpx	-18.7	3.0	2.6	6.1	230
v02_9_4_4.a.Fbp.RFcorr.Cmpx	-18.7	3.0	2.6	6.4	236
v02_9_5_3.a.Fbp.RFcorr.Cmpx	-18.1	2.9	2.5	4.4	243
v02_9_6_2.a.Fbp.RFcorr.Cmpx	-19.2	2.9	2.79	6.4	255
v02_11_1_3.a.Fbp.RFcorr.Cmpx	-18.7	3.1	2.6	6.2	225
v02_11_2_1.a.Fbp.RFcorr.Cmpx	-20.1	2.9	2.7	3.6	135
v02_11_9_2.a.Fbp.RFcorr.Cmpx	-16.8	3.2	2.6	7.1	225
v02_11_10_1.a.Fbp.RFcorr.Cmpx	-19.2	3.0	2.9	7.0	135
v02_12_1_1.a.Fbp.RFcorr.Cmpx	-16.8	3.1	2.5	4.5	45
v02_12_2_1.a.Fbp.RFcorr.Cmpx	-20.7	3.0	2.7	6.7	315
v02_12_3_1.a.Fbp.RFcorr.Cmpx	-16.5	3.0	2.7	6.6	225
v02_12_4_1.a.Fbp.RFcorr.Cmpx	-19.9	2.9	2.9	6.8	135
v02_12_5_1.a.Fbp.RFcorr.Cmpx	-18.3	3.2	2.6	6.9	45
v02_12_6_1.a.Fbp.RFcorr.Cmpx	-22.1	3.0	2.8	7.0	315
v02_13_1_2.a.Fbp.RFcorr.Cmpx	-18.2	2.8	2.6	5.9	225
v02_13_2_1.a.Fbp.RFcorr.Cmpx	-19.1	3.3	2.6	6.9	227
v02_13_3_1.a.Fbp.RFcorr.Cmpx	-19.7	3.6	2.6	7.4	230
v02_13_4_3.a.Fbp.RFcorr.Cmpx	-17.8	2.9	2.6	5.5	236
v02_13_5_3.a.Fbp.RFcorr.Cmpx	-17.9	2.9	2.6	6.2	243
v02_13_6_2.a.Fbp.RFcorr.Cmpx	-19.1	3.0	2.7	6.5	255
v02_14_1_1.a.Fbp.RFcorr.Cmpx	-20.5	3.0	2.8	6.6	225
v02_14_2_1.a.Fbp.RFcorr.Cmpx	-20.2	3.0	2.8	3.5	135
v02_14_3_1.a.Fbp.RFcorr.Cmpx	-21.5	2.9	2.8	6.6	225
v02_14_4_1.a.Fbp.RFcorr.Cmpx	-19.2	3.0	2.6	6.4	135
v02_14_5_1.a.Fbp.RFcorr.Cmpx	-22.0	3.1	2.7	6.9	230
v02_14_6_1.a.Fbp.RFcorr.Cmpx	-21.6	3.1	2.7	6.8	230
v02_14_7_2.a.Fbp.RFcorr.Cmpx	-19.4	3.0	2.7	6.2	140
v02_14_8_1.a.Fbp.RFcorr.Cmpx	-18.9	2.9	2.7	6.2	140

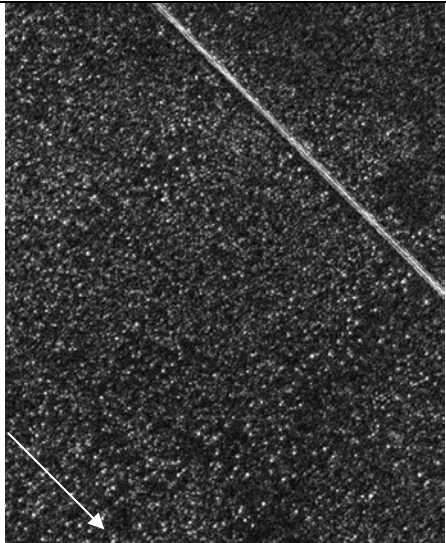
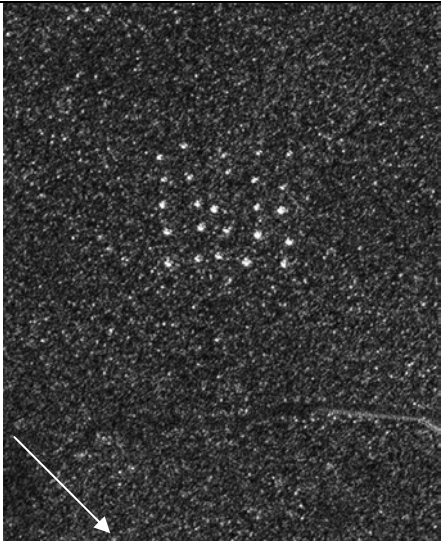
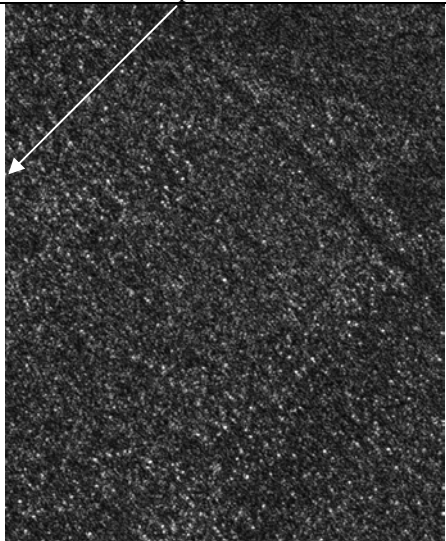
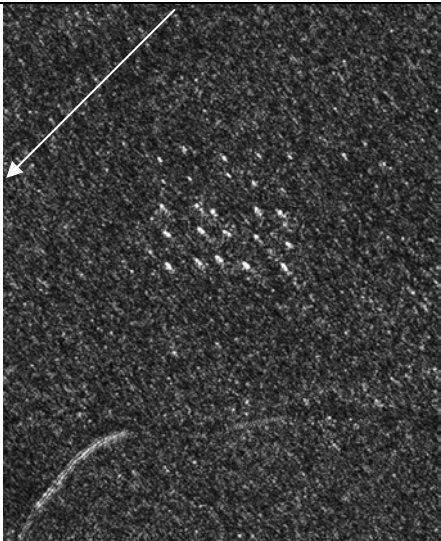
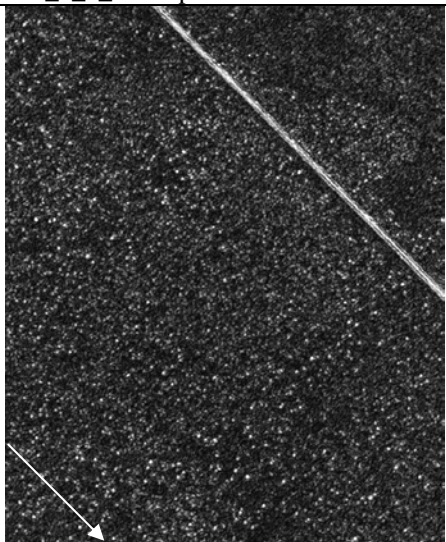
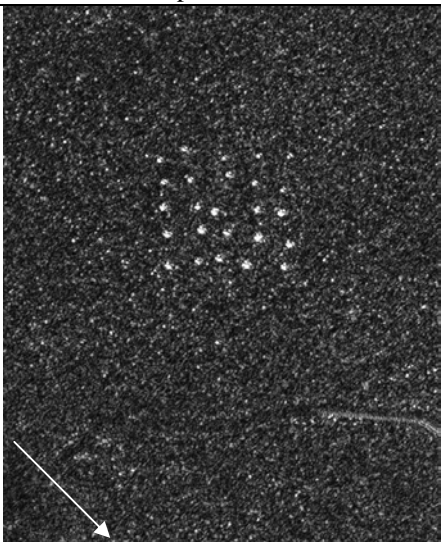
APPENDIX B SAR IMAGE CHIPS OF FOREST 1, 2

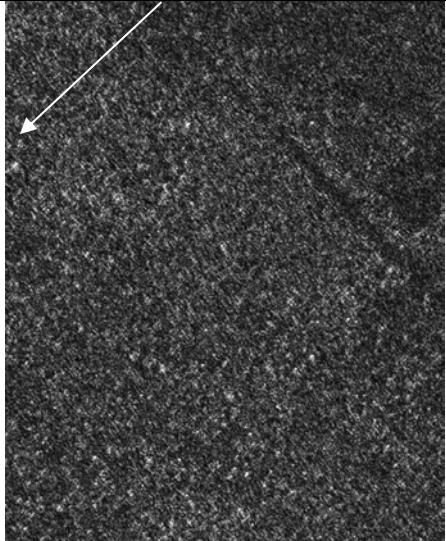
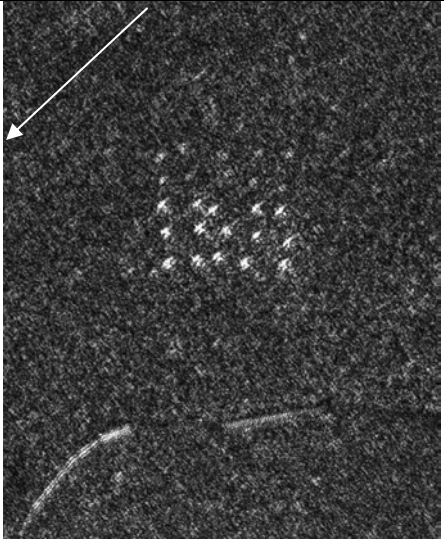
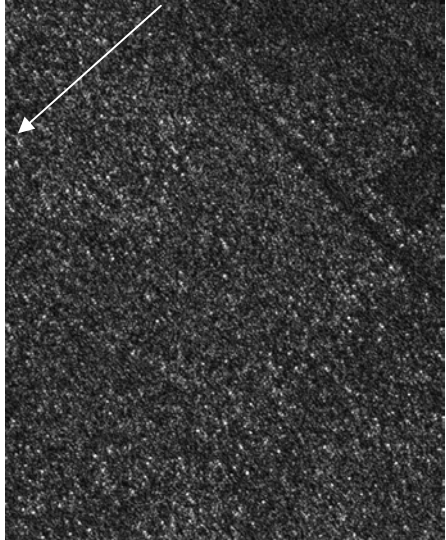
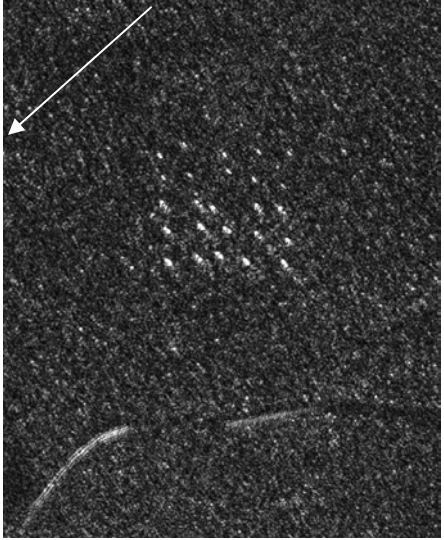
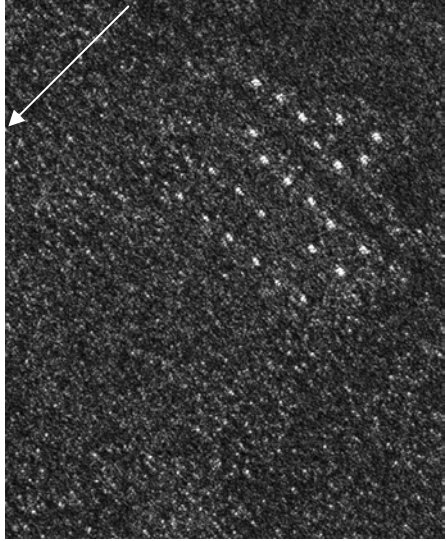
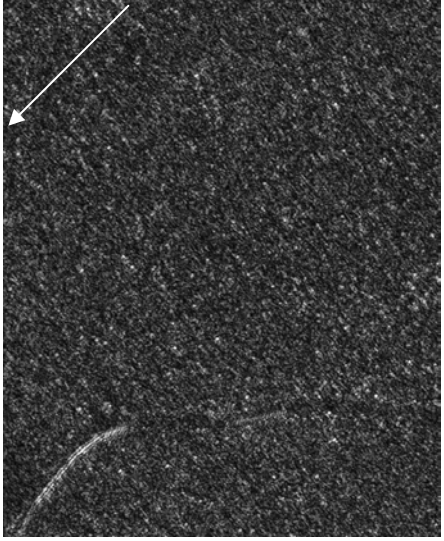
This Appendix contains SAR image chips (650 m x 800 m) over the target deployment sites (Forest 1 and 2) for each flight pass used in the present report. The nominal flight heading is annotated by an arrow in each image. All flights were conducted with the radar looking left.

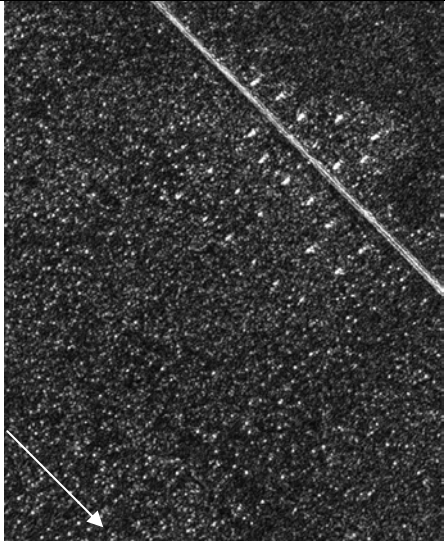
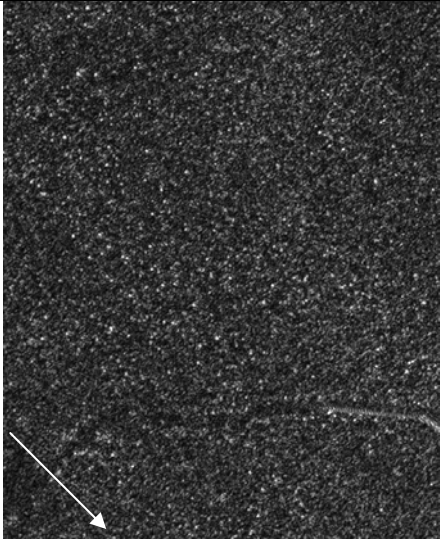
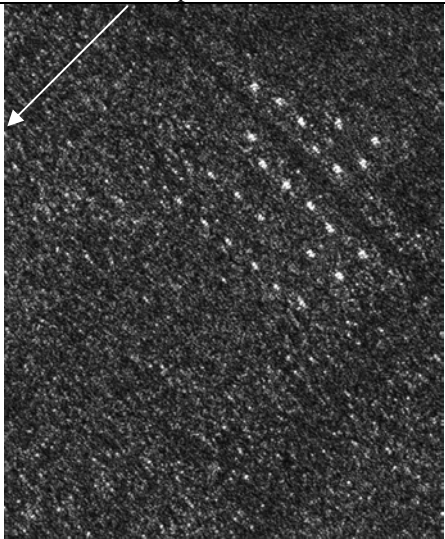
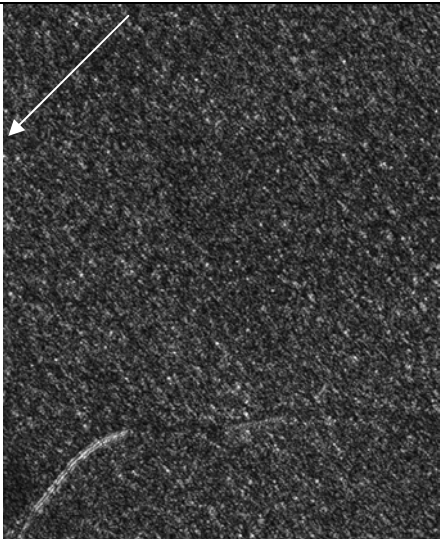
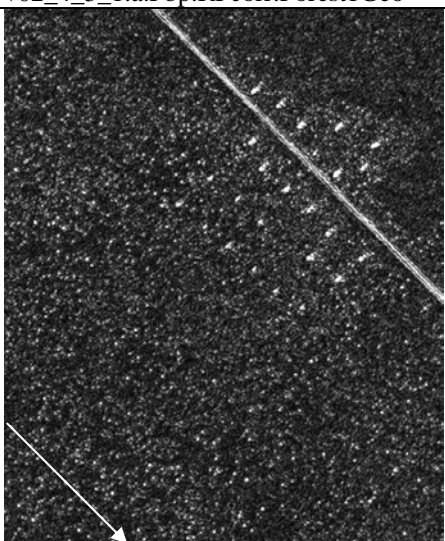
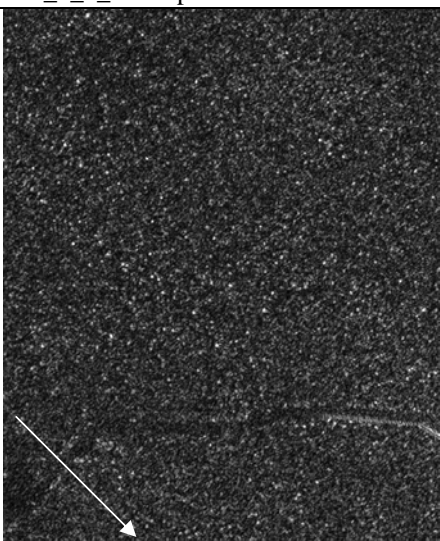
Forest 1	Forest 2	Heading (°)	Inc. Angle (°)	Deployment
 <p>Copyright Lantmäteriverket 2001. Ref. nr. 2002308.</p> <p>Aerial photo of Forest 1</p>	 <p>Copyright Lantmäteriverket 2001. Ref. nr. 2002308.</p> <p>Aerial photo of Forest 2</p>			
 <p>v02_2_1_1.a.Fbp.RFcorr.Forest1Geo</p>	 <p>v02_2_1_1.a.Fbp.RFcorr.Forest2Geo</p>	225	58	Sigismund

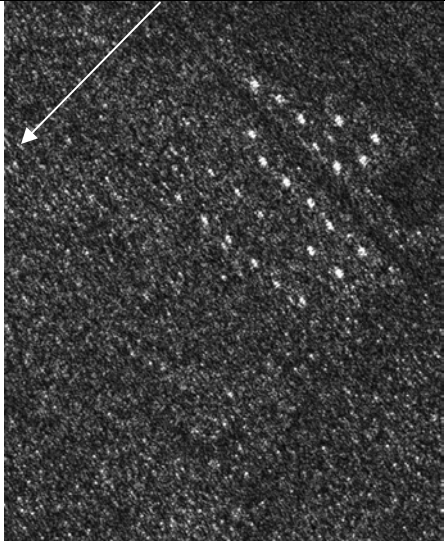
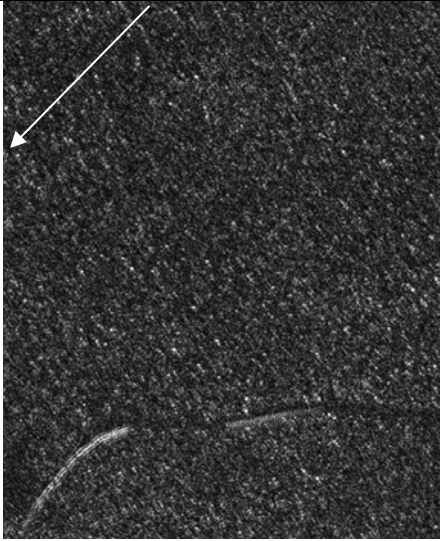
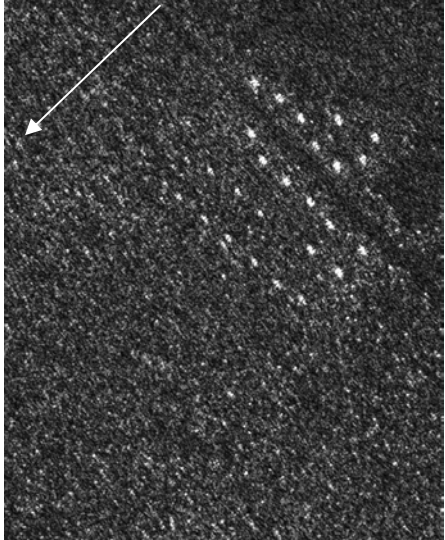
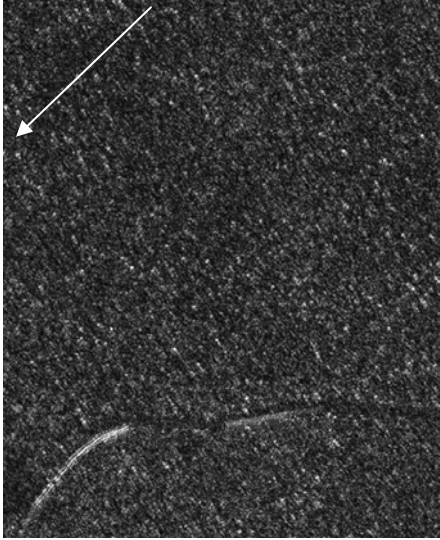
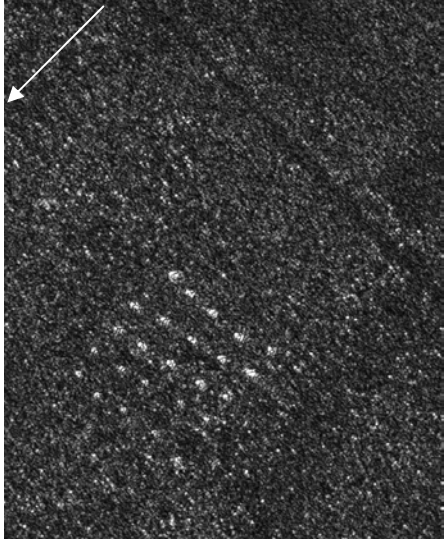
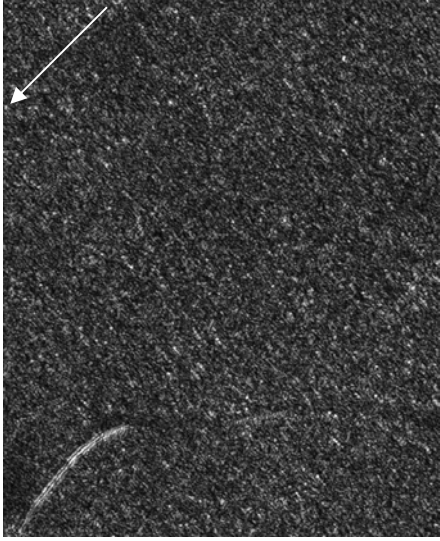
		135	58	Sigismund
v02_2_2_1.a.Fbp.RFcorr.Forest1Geo	v02_2_2_1.a.Fbp.RFcorr.Forest2Geo			
		225	58	Sigismund
v02_2_3_1.a.Fbp.RFcorr.Forest1Geo	v02_2_3_1.a.Fbp.RFcorr.Forest2Geo			
		135	58	Sigismund
v02_2_4_1.a.Fbp.RFcorr.Forest1Geo	v02_2_4_1.a.Fbp.RFcorr.Forest2Geo			

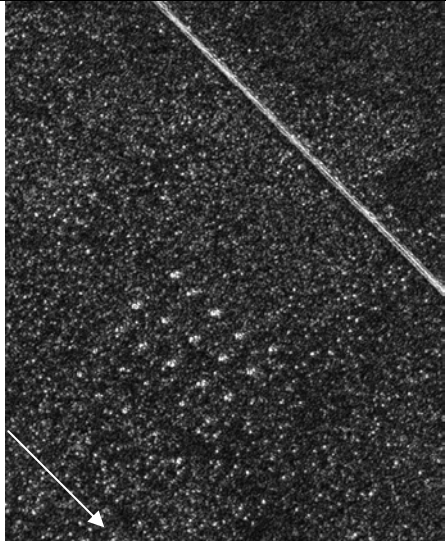
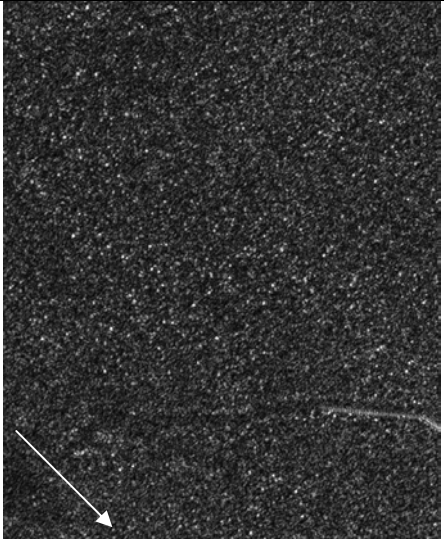
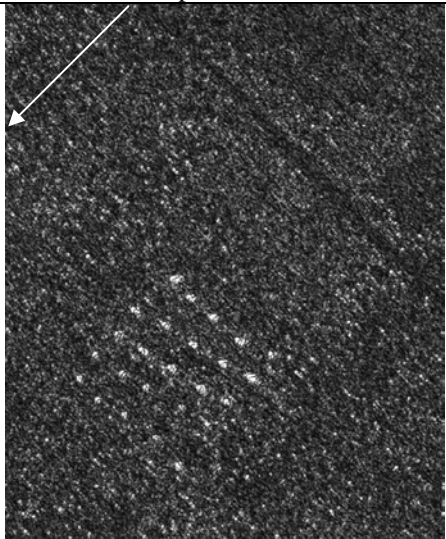
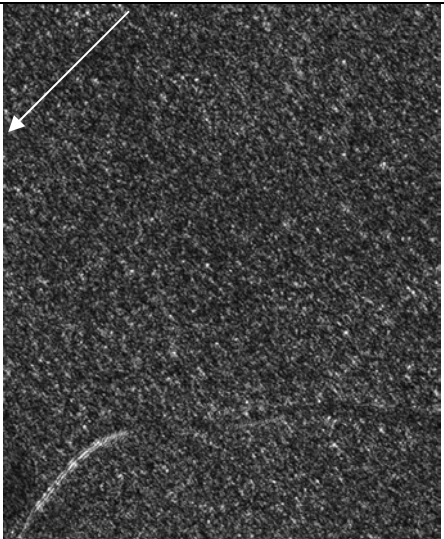
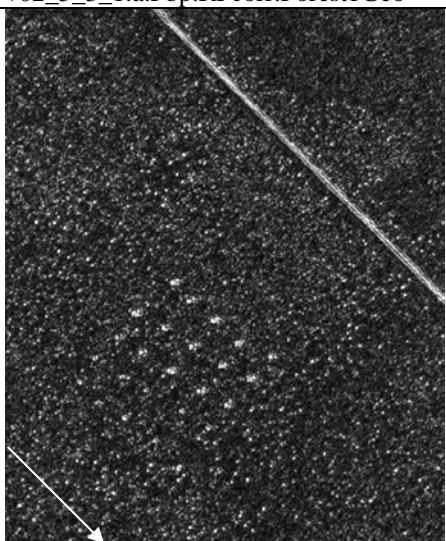
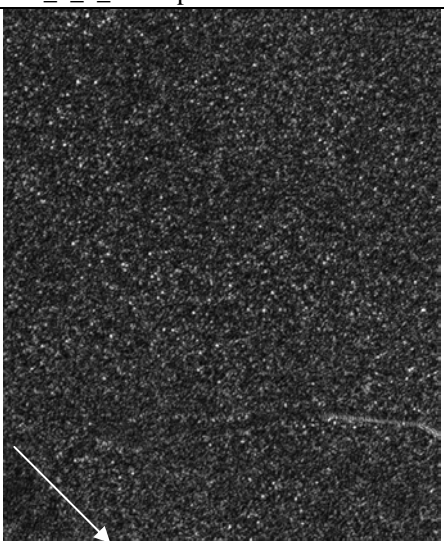
			230	58	Sigismund
v02_2_5_1.a.Fbp.RFcorr.Forest1Geo	v02_2_5_1.a.Fbp.RFcorr.Forest2Geo				
			230	58	Sigismund
v02_2_6_1.a.Fbp.RFcorr.Forest1Geo	v02_2_6_1.a.Fbp.RFcorr.Forest2Geo				
			225	58	Karl
v02_3_1_2.a.Fbp.RFcorr.Forest1Geo	v02_3_1_2.a.Fbp.RFcorr.Forest2Geo				

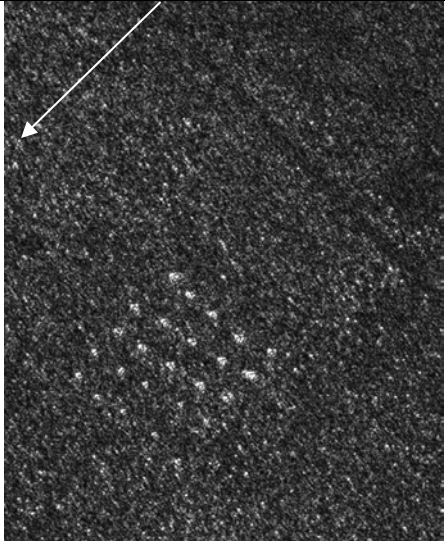
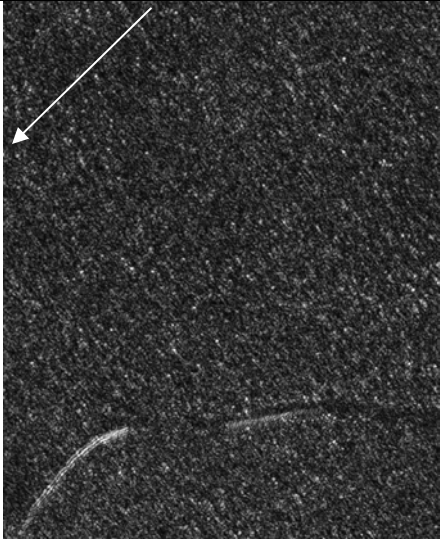
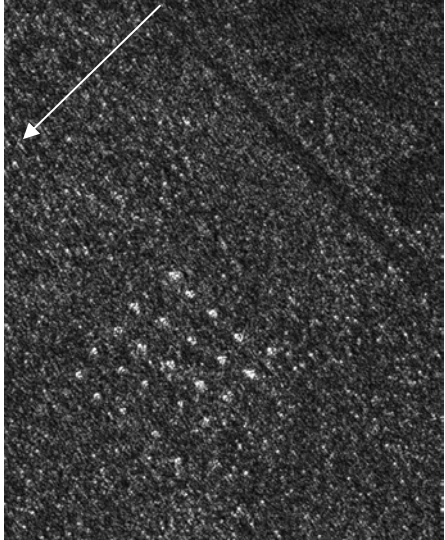
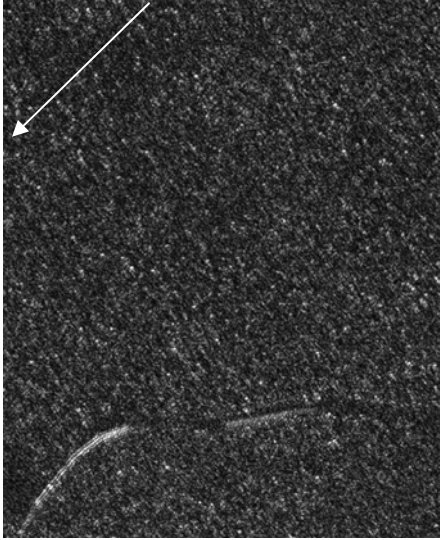
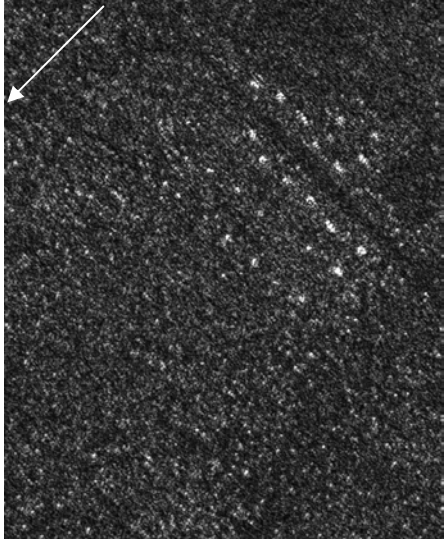
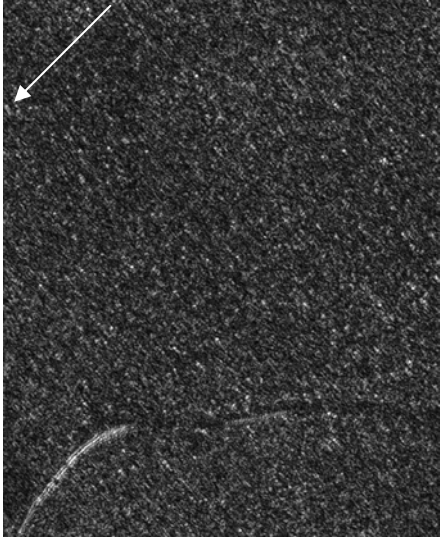
			135	58	Karl
v02_3_2_1.a.Fbp.RFcorr.Forest1Geo	v02_3_2_1.a.Fbp.RFcorr.Forest2Geo				
			225	58	Karl
v02_3_3_1.a.Fbp.RFcorr.Forest1Geo	v02_3_3_1.a.Fbp.RFcorr.Forest2Geo				
			135	58	Karl
v02_3_4_1.a.Fbp.RFcorr.Forest1Geo	v02_3_4_1.a.Fbp.RFcorr.Forest2Geo				

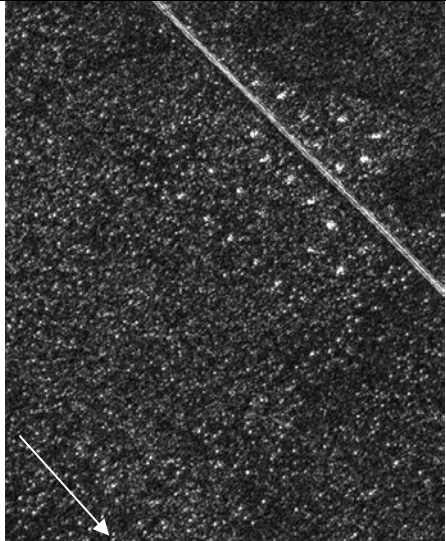
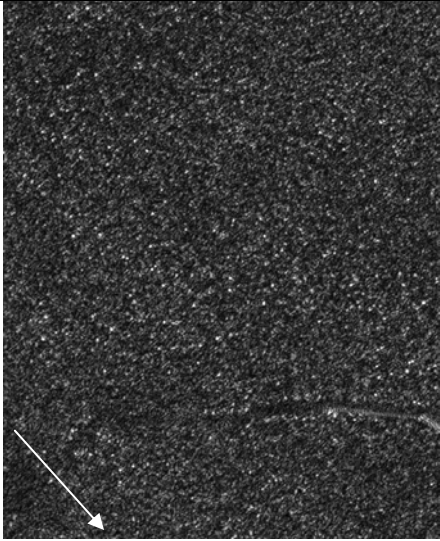
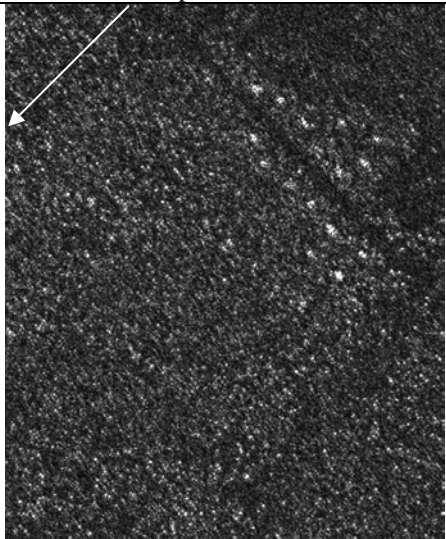
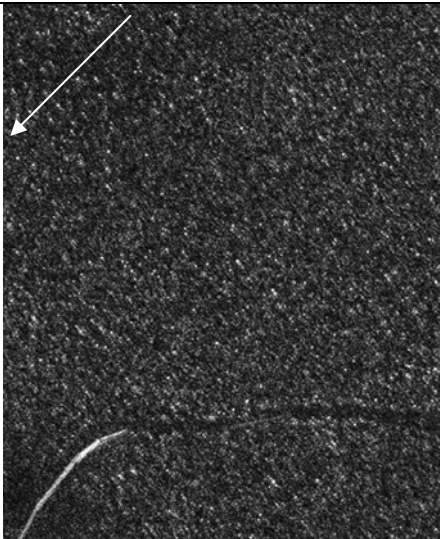
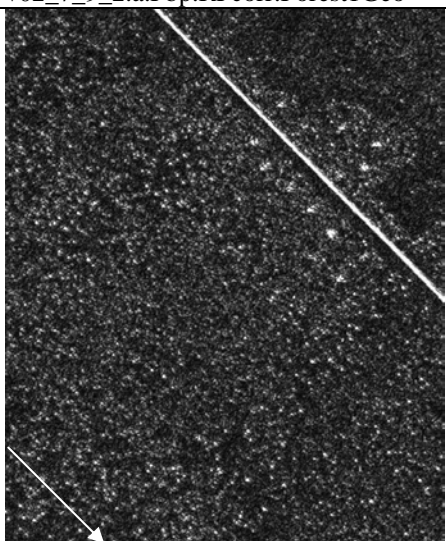
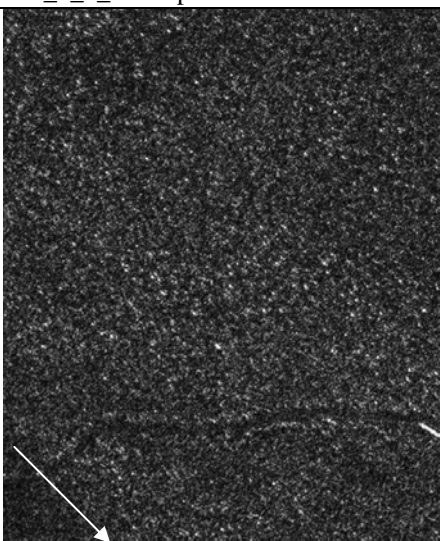
			230	58	Karl
v02_3_5_2.a.Fbp.RFcorr.Forest1Geo					
v02_3_5_2.a.Fbp.RFcorr.Forest2Geo					
			230	58	Karl
v02_3_6_1.a.Fbp.RFcorr.Forest1Geo					
v02_3_6_1.a.Fbp.RFcorr.Forest2Geo					
			225	58	Fredrik
v02_4_1_1.a.Fbp.RFcorr.Forest1Geo					
v02_4_1_1.a.Fbp.RFcorr.Forest2Geo					

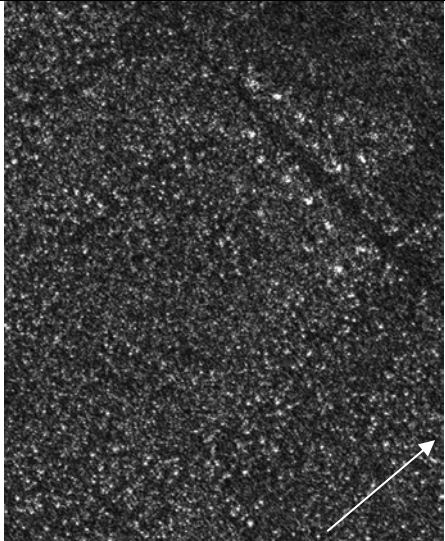
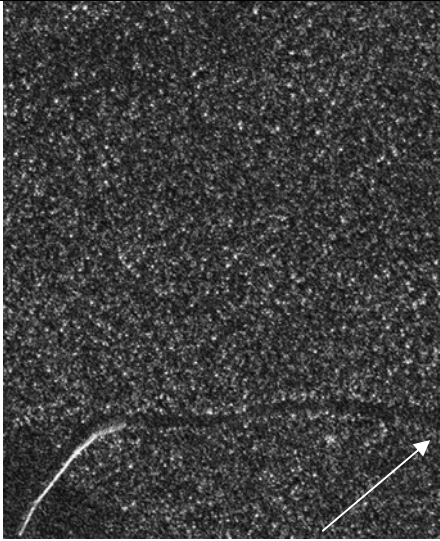
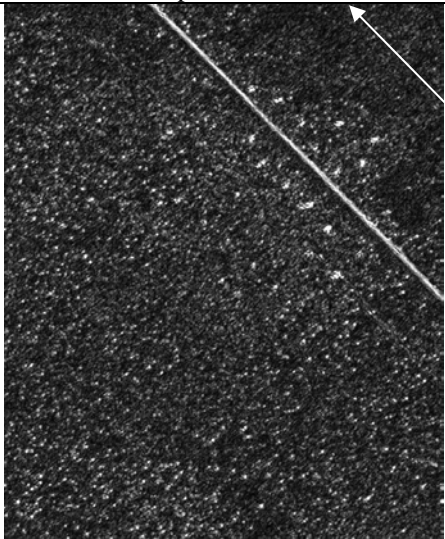
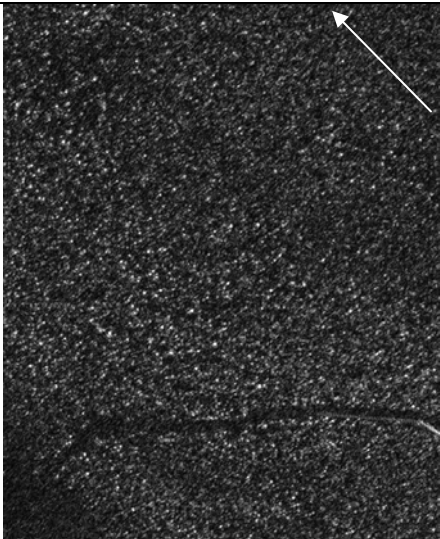
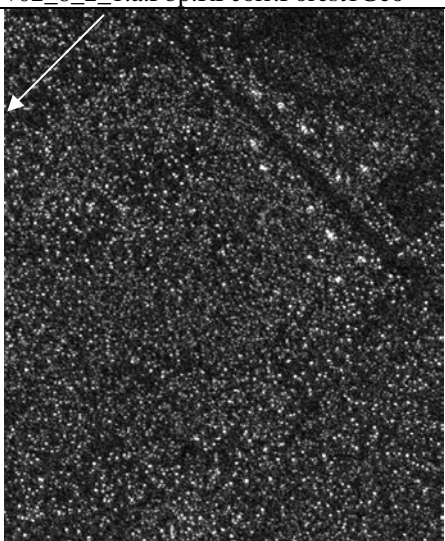
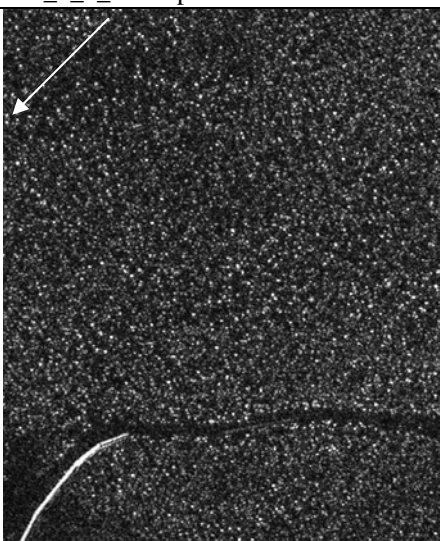
			135	58	Fredrik
v02_4_2_1.a.Fbp.RFcorr.Forest1Geo	v02_4_2_1.a.Fbp.RFcorr.Forest2Geo				
			225	58	Fredrik
v02_4_3_1.a.Fbp.RFcorr.Forest1Geo	v02_4_3_1.a.Fbp.RFcorr.Forest2Geo				
			135	58	Fredrik
v02_4_4_1.a.Fbp.RFcorr.Forest1Geo	v02_4_4_1.a.Fbp.RFcorr.Forest2Geo				

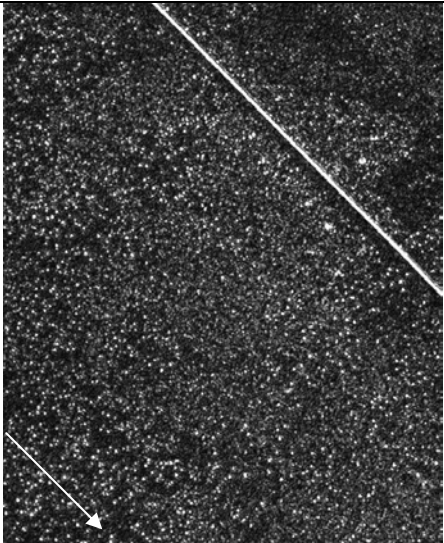
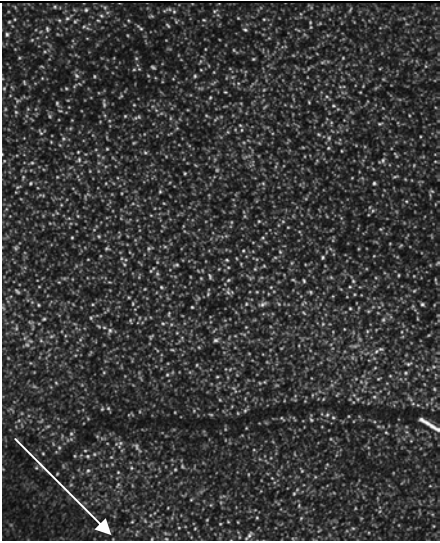
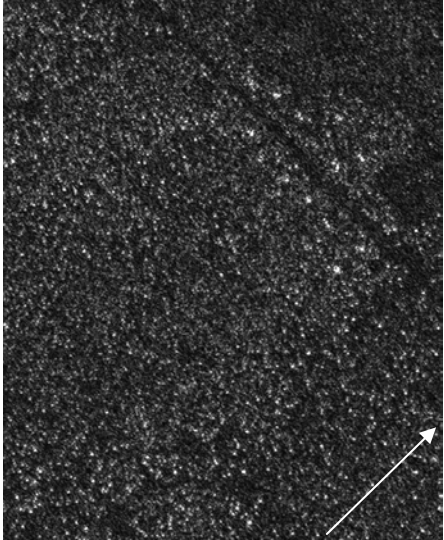
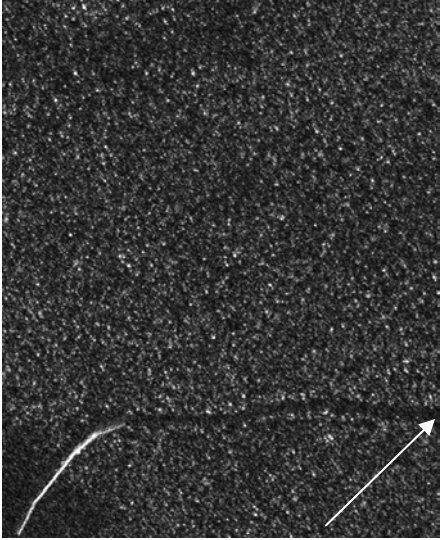
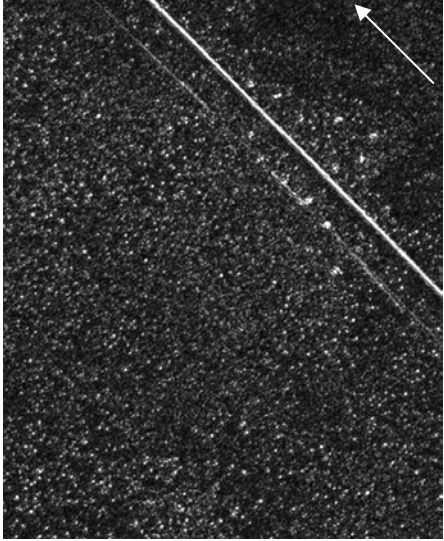
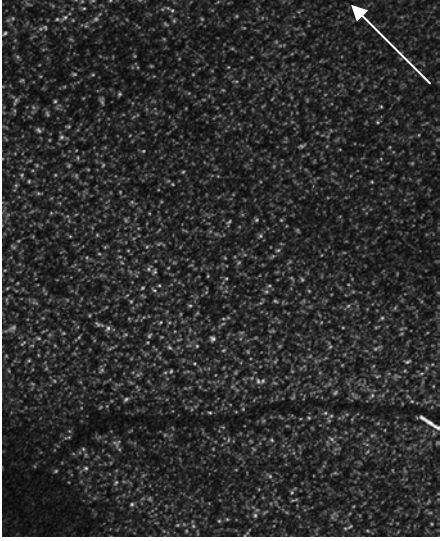
			230	58	Fredrik
v02_4_5_1.a.Fbp.RFcorr.Forest1Geo	v02_4_5_1.a.Fbp.RFcorr.Forest2Geo				
			230	58	Fredrik
v02_4_6_1.a.Fbp.RFcorr.Forest1Geo	v02_4_6_1.a.Fbp.RFcorr.Forest2Geo				
			225	58	Adolf-Fredrik
v02_5_1_1.a.Fbp.RFcorr.Forest1Geo	v02_5_1_1.a.Fbp.RFcorr.Forest2Geo				

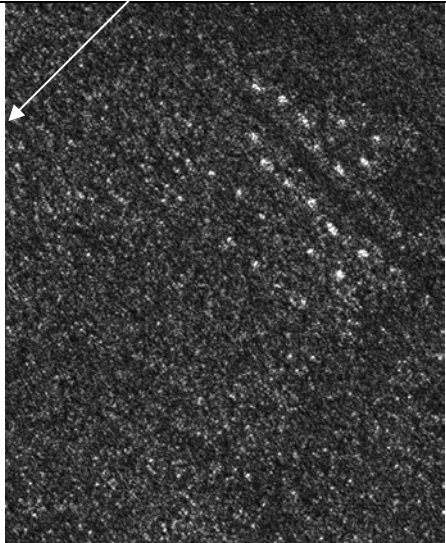
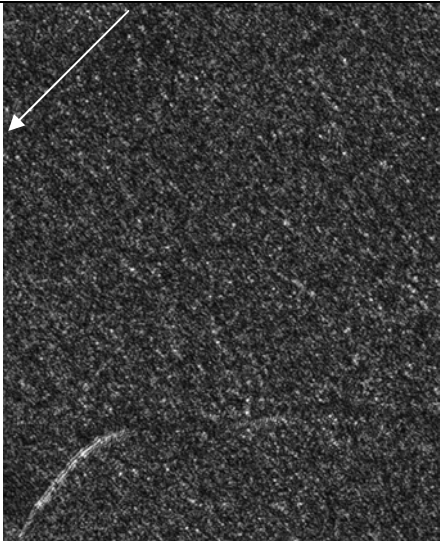
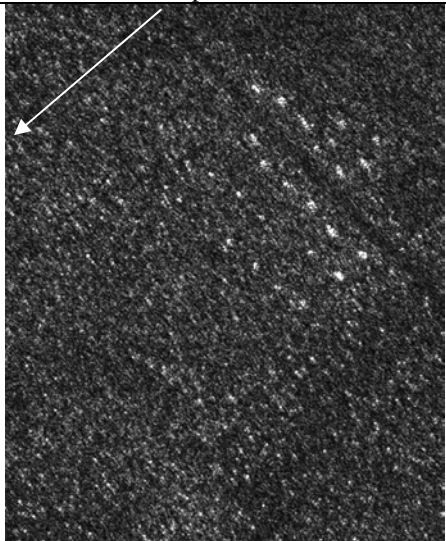
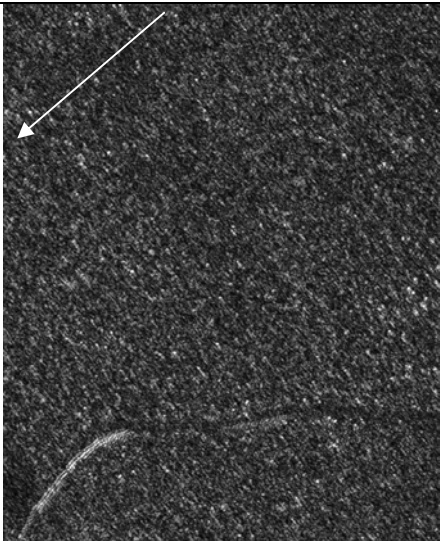
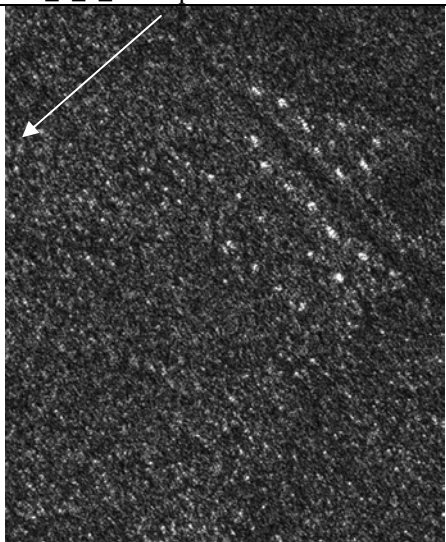
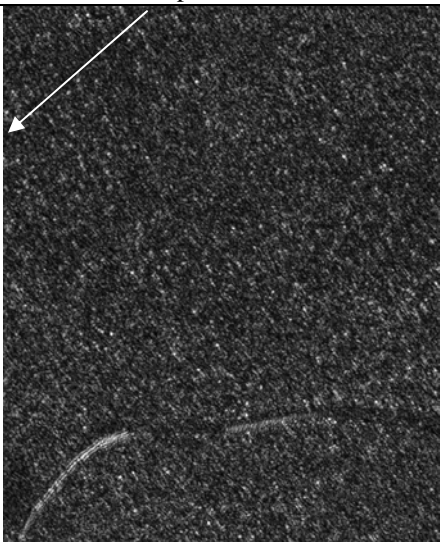
			135	58	Adolf-Fredrik
v02_5_2_1.a.Fbp.RFcorr.Forest1Geo	v02_5_2_1.a.Fbp.RFcorr.Forest2Geo				
			225	58	Adolf-Fredrik
v02_5_3_1.a.Fbp.RFcorr.Forest1Geo	v02_5_3_1.a.Fbp.RFcorr.Forest2Geo				
			135	58	Adolf-Fredrik
v02_5_4_1.a.Fbp.RFcorr.Forest1Geo	v02_5_4_1.a.Fbp.RFcorr.Forest2Geo				

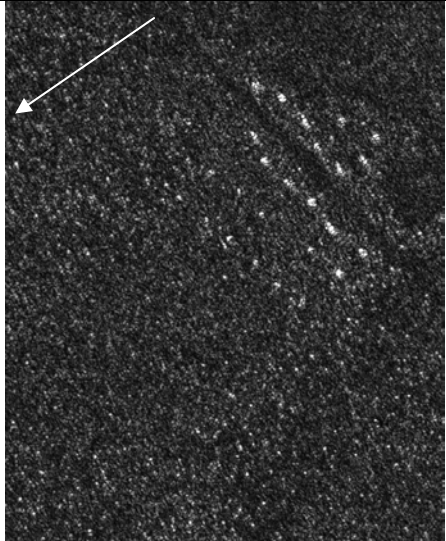
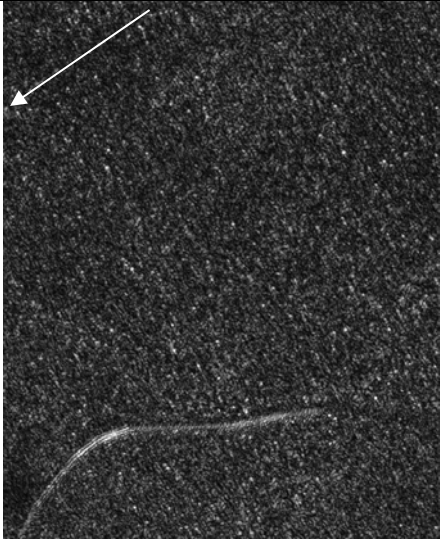
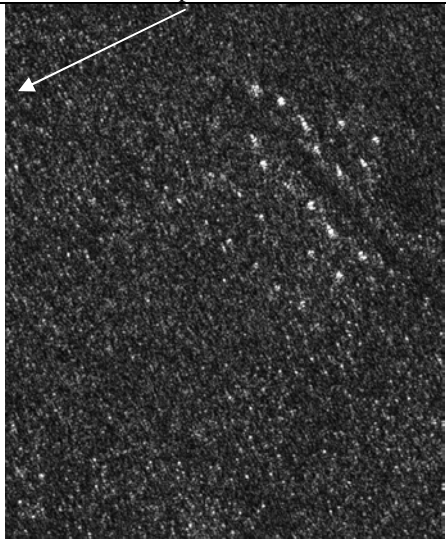
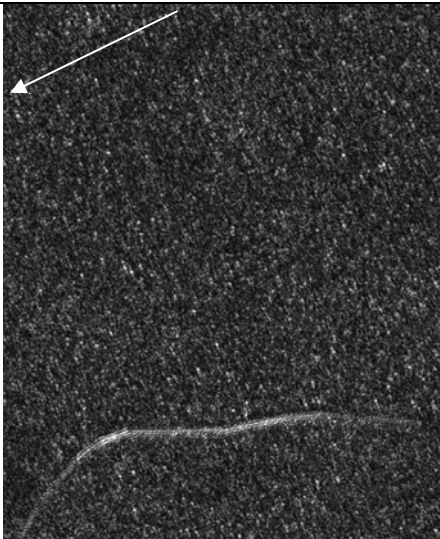
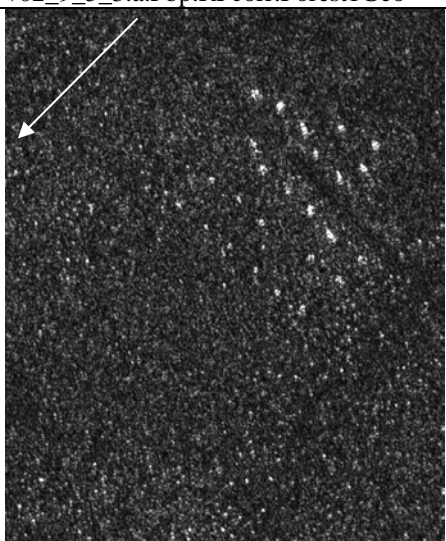
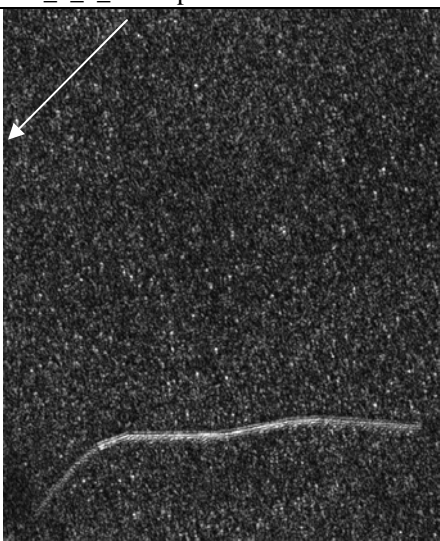
			230	58	Adolf-Fredrik
v02_5_5_1.a.Fbp.RFcorr.Forest1Geo	v02_5_5_1.a.Fbp.RFcorr.Forest2Geo				
			230	58	Adolf-Fredrik
v02_5_6_1.a.Fbp.RFcorr.Forest1Geo	v02_5_6_1.a.Fbp.RFcorr.Forest2Geo				
			225	58	Gustav
v02_7_1_9.a.Fbp.RFcorr.Forest1Geo	v02_7_1_9.a.Fbp.RFcorr.Forest2Geo				

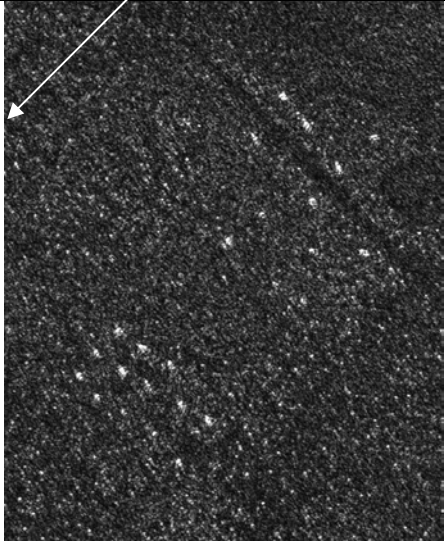
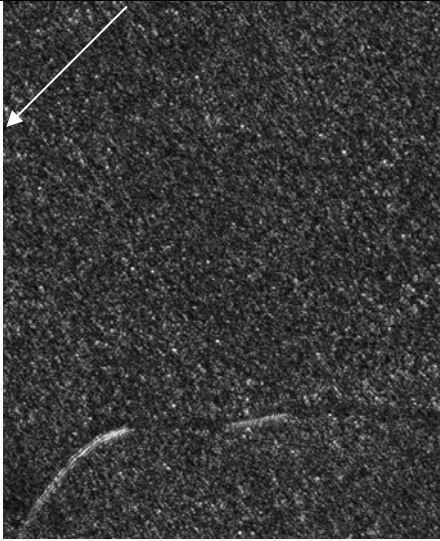
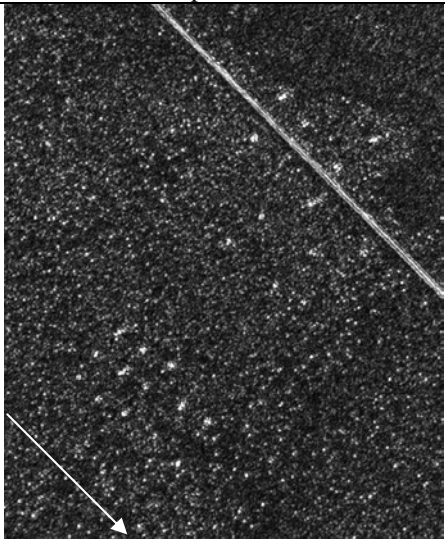
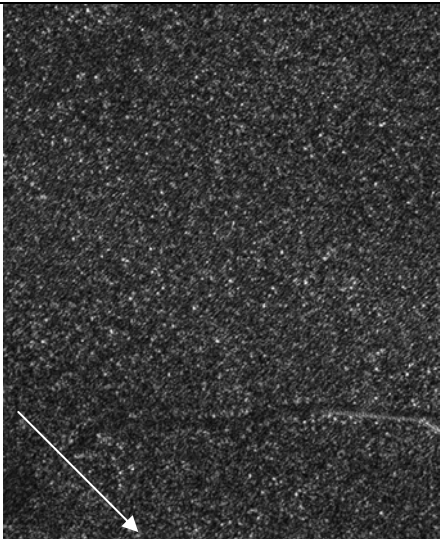
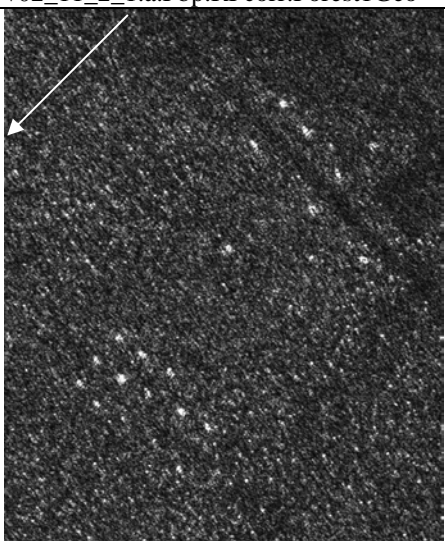
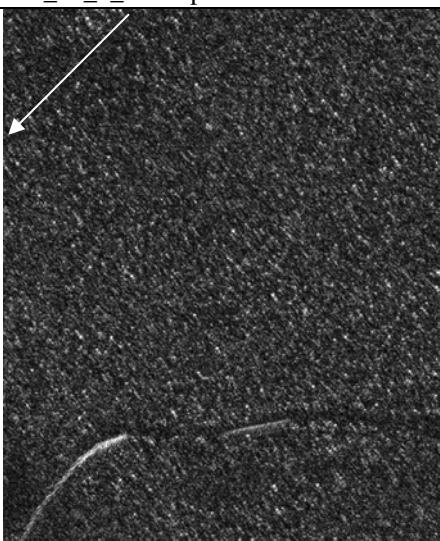
			135	58	Gustav
			225	68	Gustav
			135	68	Gustav

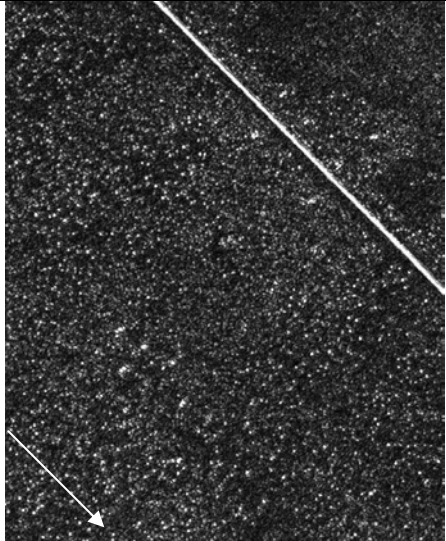
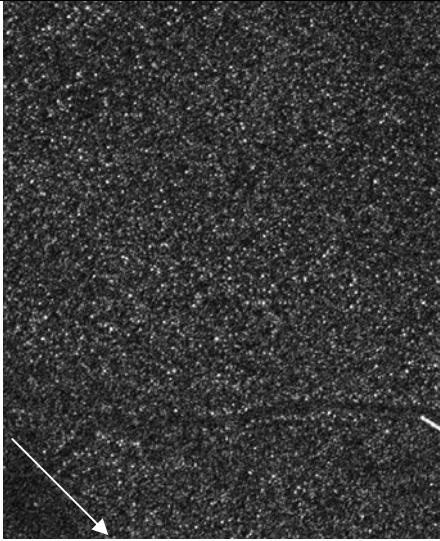
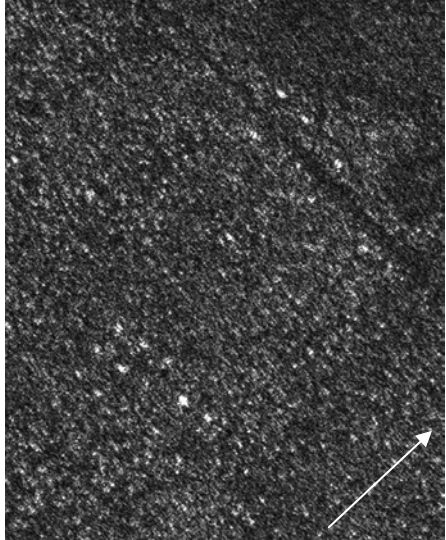
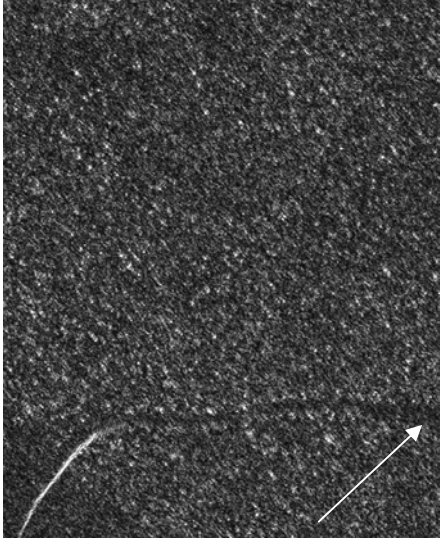
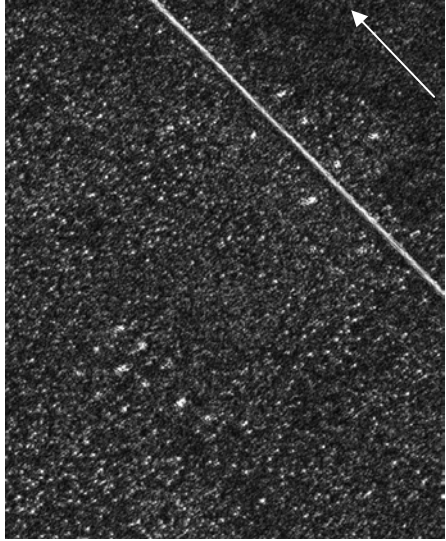
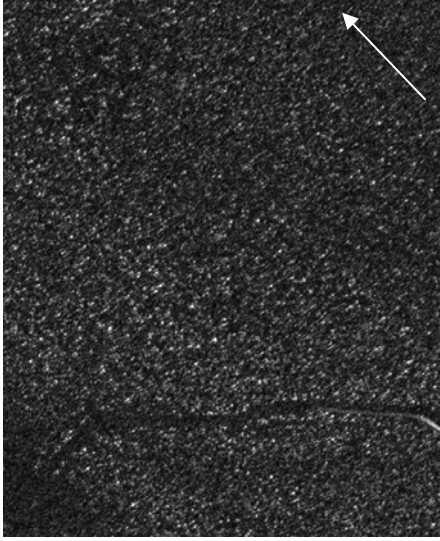
		45	68	Gustav
		315	68	Gustav
		225	72	Gustav

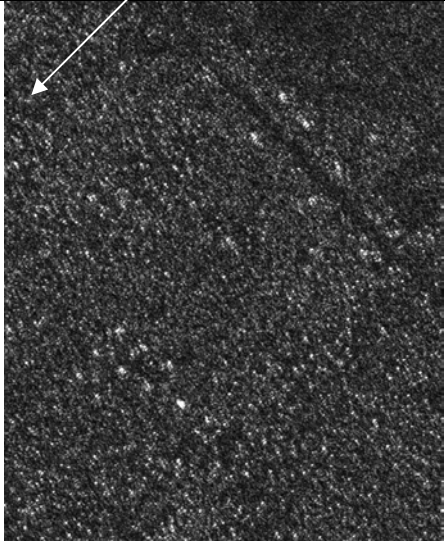
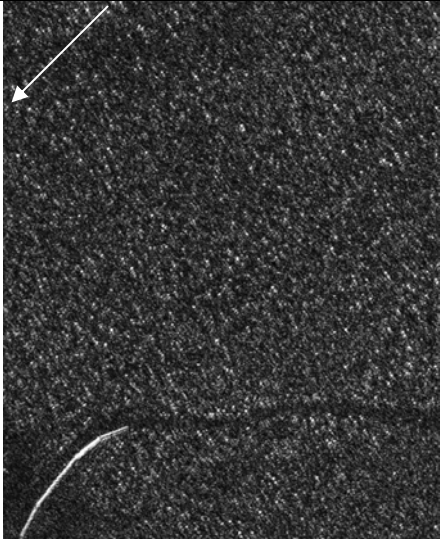
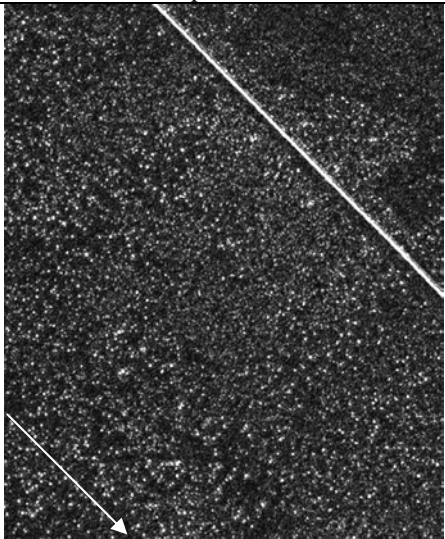
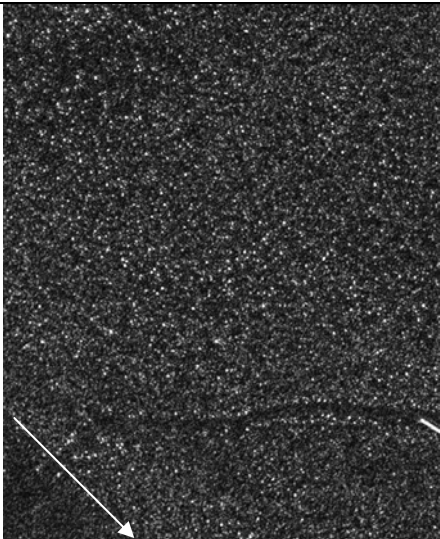
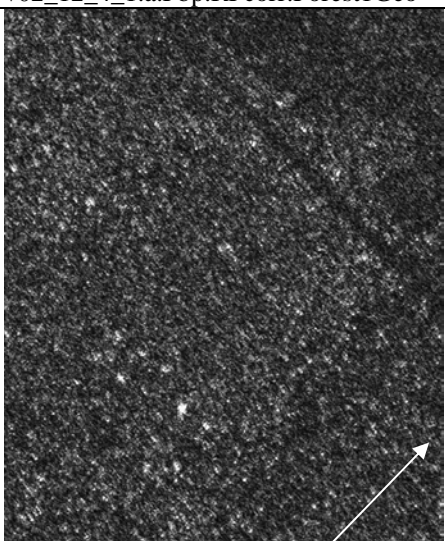
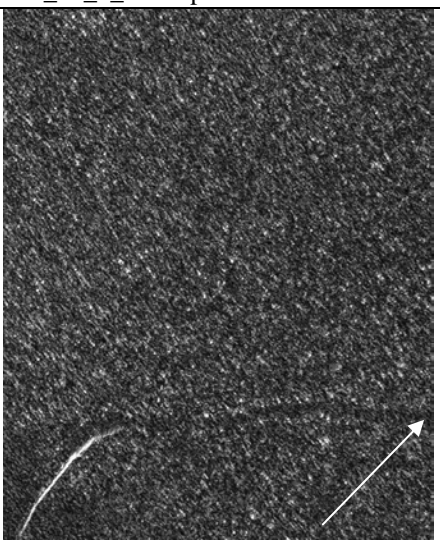
			135	72	Gustav
v02_8_4_1.a.Fbp.RFcorr.Forest1Geo	v02_8_4_1.a.Fbp.RFcorr.Forest2Geo				
			45	72	Gustav
v02_8_5_1.a.Fbp.RFcorr.Forest1Geo	v02_8_5_1.a.Fbp.RFcorr.Forest2Geo				
			315	72	Gustav
v02_8_6_1.a.Fbp.RFcorr.Forest1Geo	v02_8_6_1.a.Fbp.RFcorr.Forest2Geo				

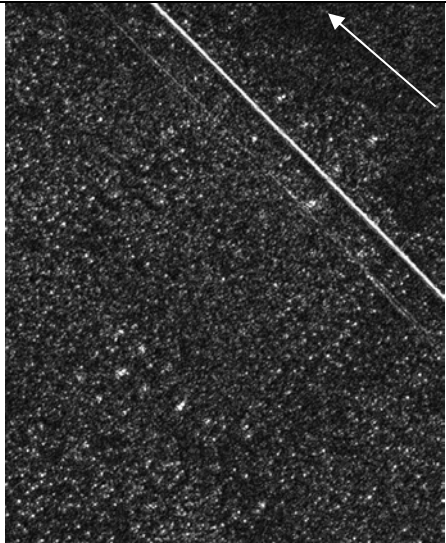
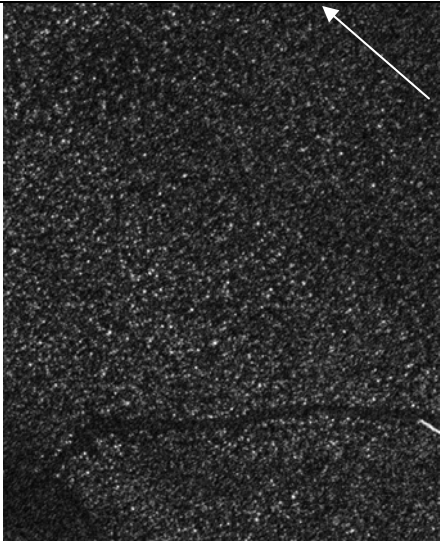
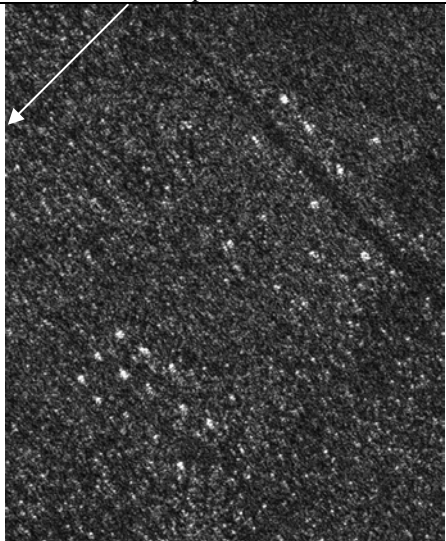
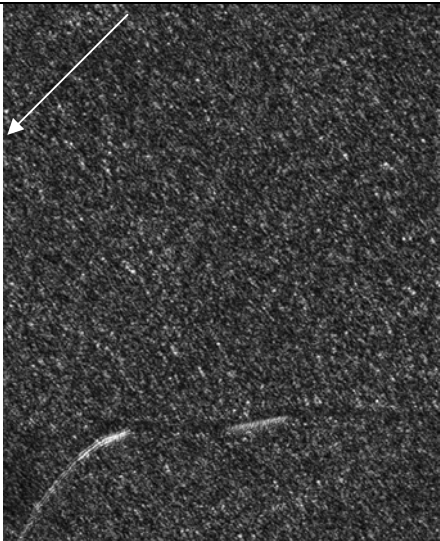
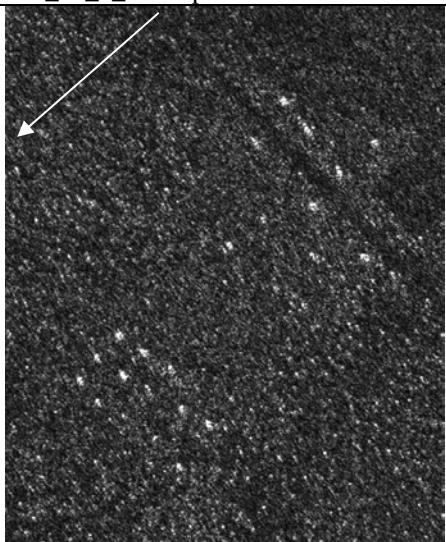
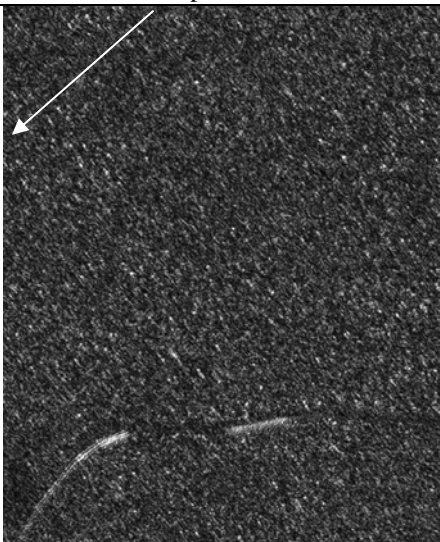
			225	58	Gustav
v02_9_1_13.a.Fbp.RFcorr.Forest1Geo	v02_9_1_13.a.Fbp.RFcorr.Forest2Geo				
			227	58	Gustav
v02_9_2_3.a.Fbp.RFcorr.Forest1Geo	v02_9_2_3.a.Fbp.RFcorr.Forest2Geo				
			230	58	Gustav
v02_9_3_6.a.Fbp.RFcorr.Forest1Geo	v02_9_3_6.a.Fbp.RFcorr.Forest2Geo				

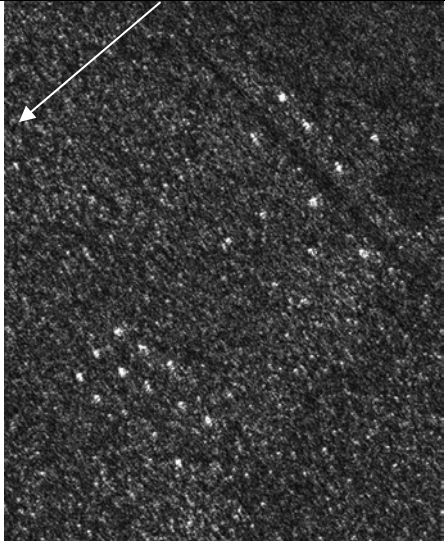
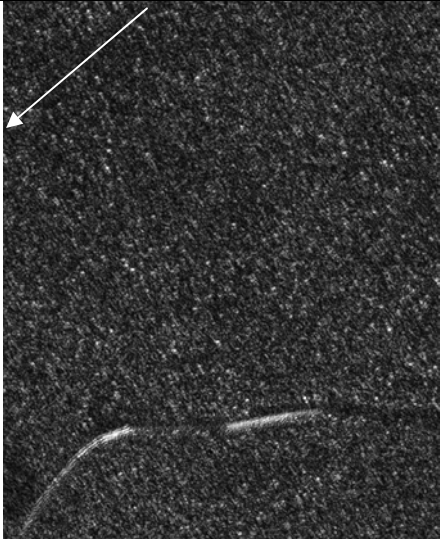
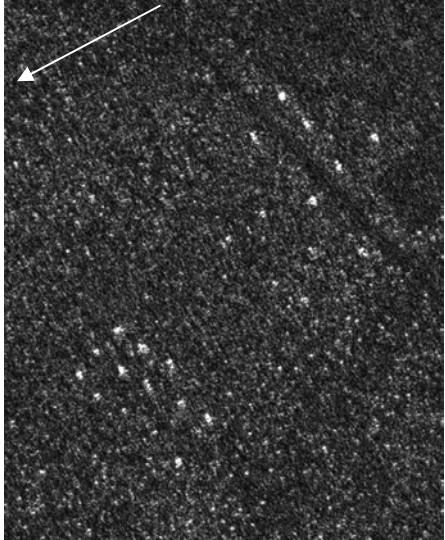
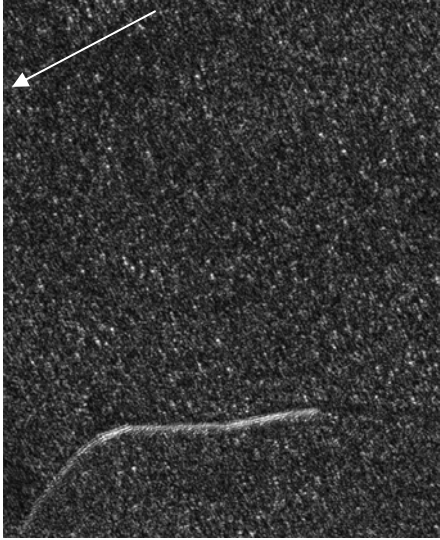
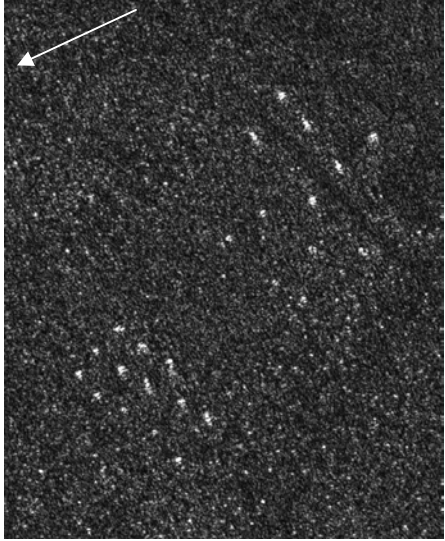

			236	58	Gustav
v02_9_4_4.a.Fbp.RFcorr.Forest1Geo	v02_9_4_4.a.Fbp.RFcorr.Forest2Geo				
			243	58	Gustav
v02_9_5_3.a.Fbp.RFcorr.Forest1Geo	v02_9_5_3.a.Fbp.RFcorr.Forest2Geo				
			255	58	Gustav
v02_9_6_2.a.Fbp.RFcorr.Forest1Geo	v02_9_6_2.a.Fbp.RFcorr.Forest2Geo				

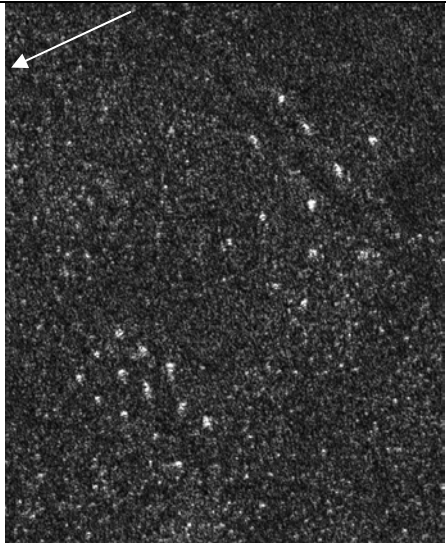

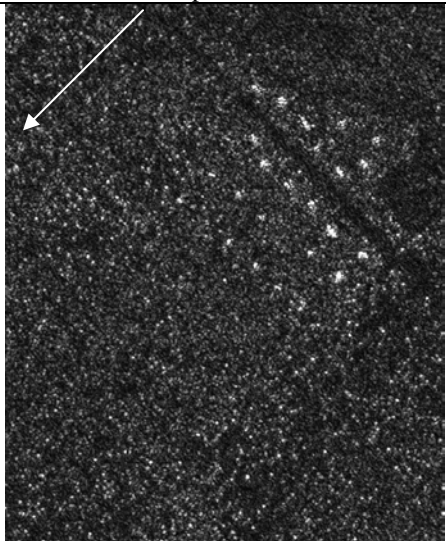
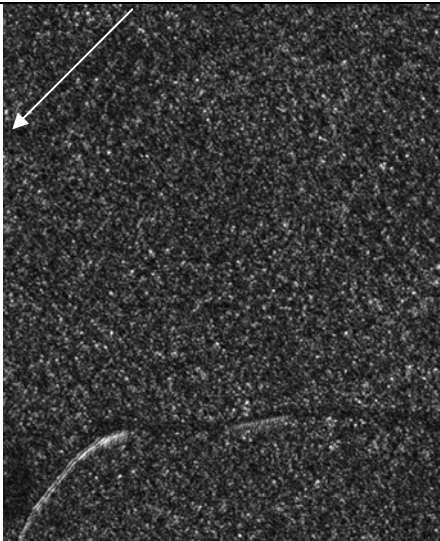
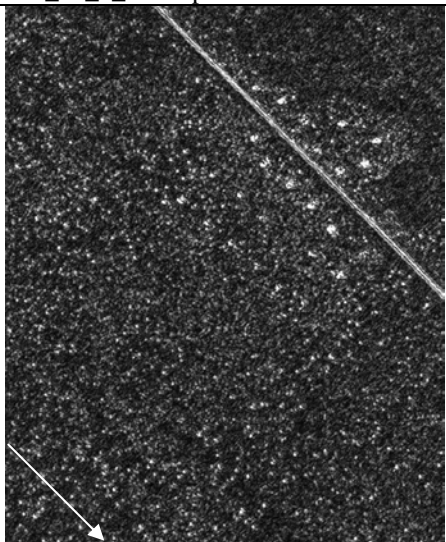
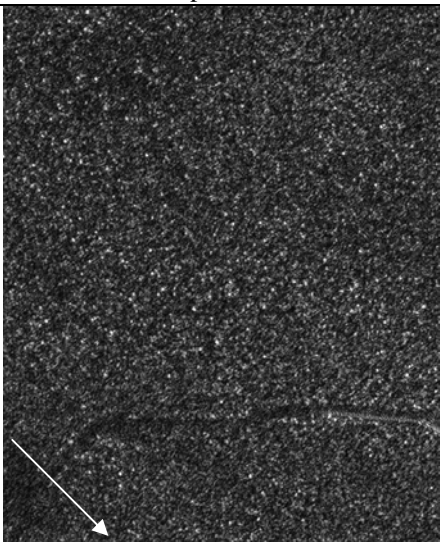
			225	58	Johan
			135	58	Johan
			225	68	Johan

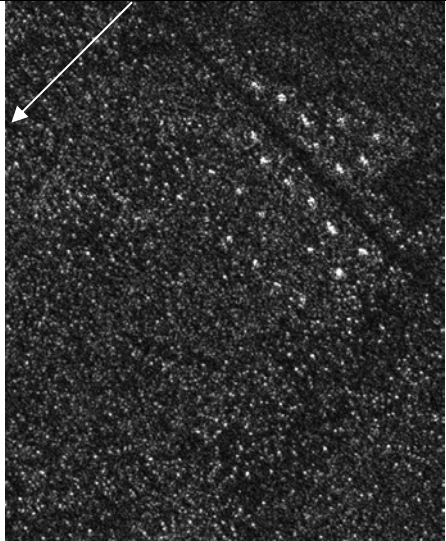
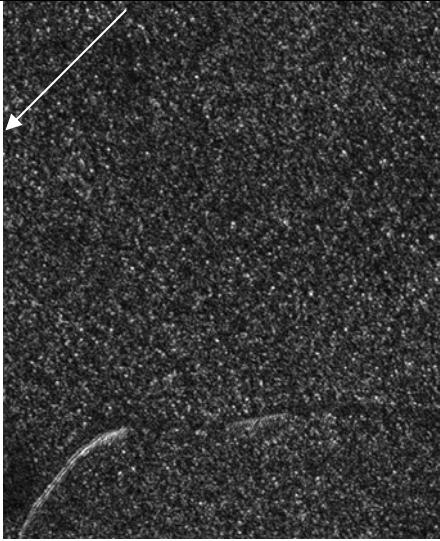
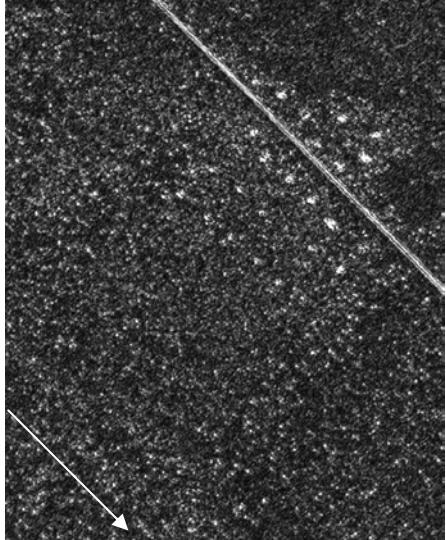
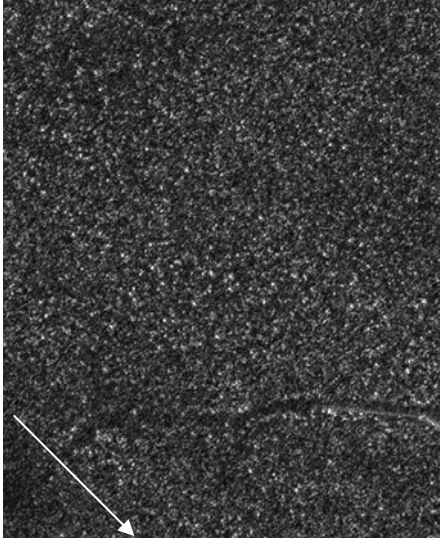
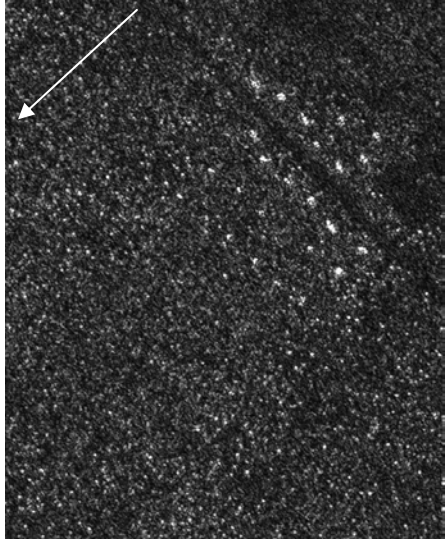
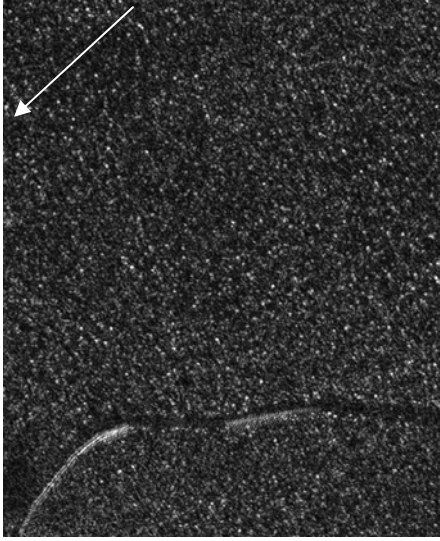
			135	68	Johan
			45	68	Johan
			315	68	Johan

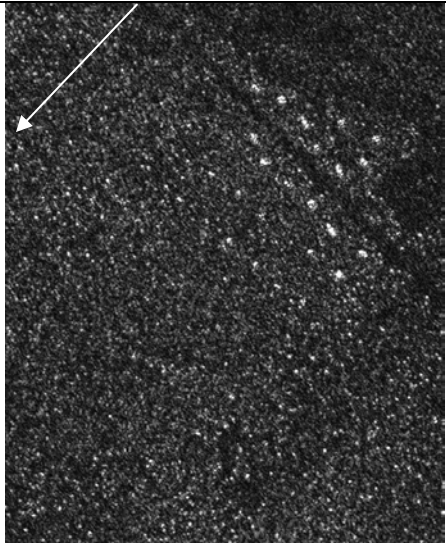
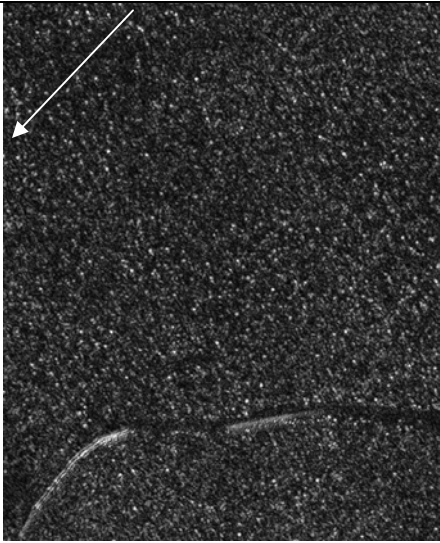
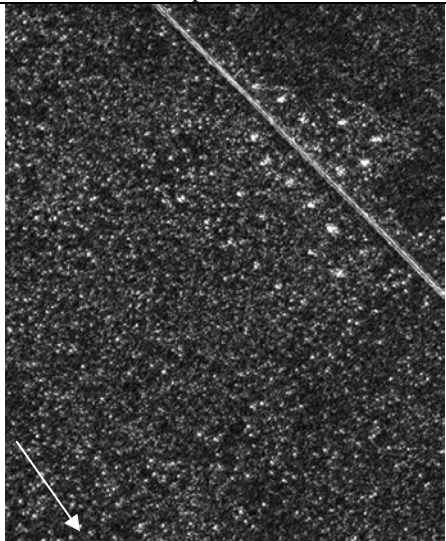
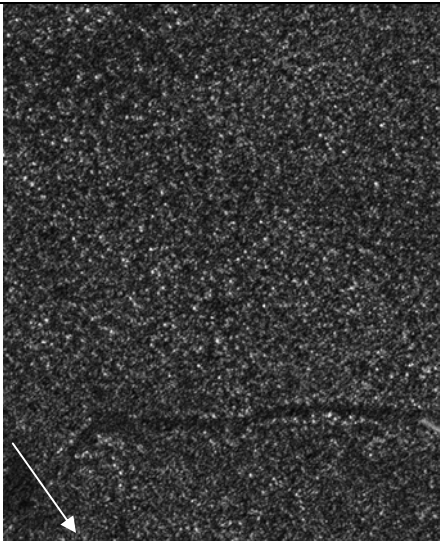
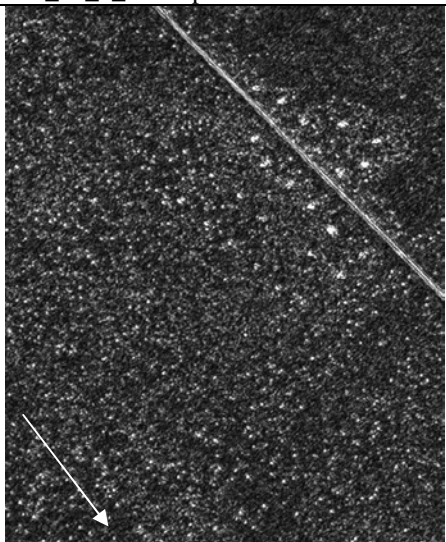
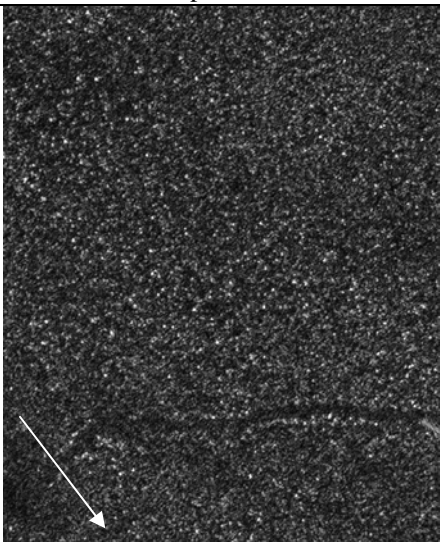
			225	72	Johan
			135	72	Johan
			45	72	Johan

			315	72	Johan
v02_12_6_1.a.Fbp.RFcorr.Forest1Geo	v02_12_6_1.a.Fbp.RFcorr.Forest2Geo				
			225	58	Johan
v02_13_1_2.a.Fbp.RFcorr.Forest1Geo	v02_13_1_2.a.Fbp.RFcorr.Forest2Geo				
			227	58	Johan
v02_13_2_1.a.Fbp.RFcorr.Forest1Geo	v02_13_2_1.a.Fbp.RFcorr.Forest2Geo				

			230	58	Johan
v02_13_3_1.a.Fbp.RFcorr.Forest1Geo	v02_13_3_1.a.Fbp.RFcorr.Forest2Geo				
			236	58	Johan
v02_13_4_3.a.Fbp.RFcorr.Forest1Geo	v02_13_4_3.a.Fbp.RFcorr.Forest2Geo				
			243	58	Johan
v02_13_5_3.a.Fbp.RFcorr.Forest1Geo	v02_13_5_3.a.Fbp.RFcorr.Forest2Geo				

		255	58	Johan
		225	58	Gustav
		135	58	Gustav

			225	58	Gustav
v02_14_3_1.a.Fbp.RFcorr.Forest1Geo	v02_14_3_1.a.Fbp.RFcorr.Forest2Geo				
			135	58	Gustav
v02_14_4_1.a.Fbp.RFcorr.Forest1Geo	v02_14_4_1.a.Fbp.RFcorr.Forest2Geo				
			230	58	Gustav
v02_14_5_1.a.Fbp.RFcorr.Forest1Geo	v02_14_5_1.a.Fbp.RFcorr.Forest2Geo				

			230	58	Gustav
			140	58	Gustav
			140	58	Gustav